Resonance ionization spectroscopy with time of flight mass spectrometry

by

Frederick John Waso

Thesis presented in partial fulfilment of the requirements for the degree of Master of Science in Physics in the Faculty of Natural Science at Stellenbosch University

Supervisors:

Dr. C.M. Steenkamp
Prof. A. du Plessis
Dr. R.A. Bark

April 2019

Declaration

By submitting this thesis electronically, I declare that the entirety of the work contained therein is my own, original work, that I am the sole author thereof (save to the extent explicitly otherwise stated), that reproduction and publication thereof by Stellenbosch University will not infringe any third party rights and that I have not previously in its entirety or in part submitted it for obtaining any qualification.

Date: April 2019

i

Abstract

Resonance ionization spectroscopy with time of flight mass spectrometry

F.J. Waso

Department of Physics
University of Stellenbosch
Private Bag X1, Matieland 7602, South Africa

Thesis: MSc (Phys)

April 2019

Resonance ionization using laser light is one of the most useful techniques for isolating radioactive isotopes and producing radioactive ion beams at accelerator facilities around the world. The aim of this study was to develop an offline experiment for resonance ionization spectroscopy (RIS) using the non-radioactive element tin. Tin was selected as a test element due to its unique nuclear properties and is an element of interest in various nuclear and astrophysical studies.

Various properties of the nucleus can impact the atomic energy levels of the atom. Laser spectroscopy can be used to probe and determine these nuclear properties. RIS is one spectroscopic technique that can be used for this purpose.

RIS will be used to produce ions of non-radioactive tin and a time-of-flight mass spectrometer (ToF-MS) will be used to detect these ions. Two separate atom sources have been designed and developed, namely a supersonic jet source and an effusive atomic beam source. Due to administrative delays the ToF-MS could not be implemented in the current study.

Simulations using the IBSimu simulation library were performed to study and understand the influence of various experimental parameters in an effort to predict optimal parameters for the experimental setup.

The impact of the initial volume and velocity distribution of the ions in the atom sources were studied. From the simulations it was observed that a fine

margin exists between a too small or too big initial volume. The resolution decreases as the initial volume increases, but at too small volumes space charge effects start to reduce the resolution of the mass spectra as well. It was observed that ions with large transverse velocity components reduce the resolution of the ToF-MS. Proper beam collimation through the use of skimmers can help reduce the transverse velocity spread and improve the resolution of the instrument.

The ToF-MS is fitted with an ion reflector called a reflectron. The reflectron greatly improves the resolution of the ToF-MS and is a crucial component to obtain high resolution spectra. From the results it was observed that a linear potential gradient in the reflectron would be optimal for the resolution of the ToF-MS.

The two atom sources were compared, and depending on the aim both sources have distinct advantages. The effusive source will be easier to implement and will be ideal to test the sensitivity and resolution of the ToF-MS. The Doppler broadening of the spectral lines in the effusive beam, however, makes selective excitation and ionization impossible. The supersonic jet limits Doppler broadening and is therefore crucial for selective ionization of Sn.

The simulations provided an insight into the influence of various experimental parameters that will facilitate the implementation of the ToF-MS at a later stage.

Uittreksel

Resonans ionisasie spektroskopie met vlugtyd massa spektrometrie

("Resonance ionization spectroscopy with time of flight mass spectrometry")

F.J. Waso

Fisika Departement
Universiteit van Stellenbosch
Privaatsak X1, Matieland 7602, Suid Afrika

Tesis: MSc (Phys)

April 2019

Resonans ionisasie deur gebruik te maak van laser lig is een van die handigste tegnieke vir die isolasie van radioaktiewe isotope asook vir die produksie van radioaktiewe ioon bundels by versneller fasiliteite wêreldwyd. Die doel van hierdie studie was om 'n eksperiment vir resonans ionisasie spektroskopie (RIS) te ontwikkel deur gebruik te maak van die nie-radioaktiewe element tin. Tin was gekies weens die unieke kern eienskappe van die elemente. Daar is ook 'n groot belangstelling in tin in verskeie kern en astrofisika studies.

Verskeie eienskappe van die kern beïnvloed die atomiese energievlakke die atoom. Laser spektroskopie kan gebruik word om hierdie kern eienskappe te bepaal. Een van die spektroskopiese tegnieke wat gebruik kan word is RIS.

RIS sal gebruik word om ione van tin te produseer en 'n vlugtyd massa spektrometer gaan gebruik word om die ione waar te neem. Twee verskillende atoom bronne is ontwerp en vervaardig, naamlik 'n supersoniese gas bron en 'n effusie bron. Weens administratiewe vertragings kon die vlugtyd massa spektrometer nie in die tydsverloop van hierdie studie opgestel word nie.

Die IBSimu simulasie pakket is gebruik om simulasies te hardloop wat die impak van verskeie eksperimentele kondisies bepaal. Vanuit die simulasies kan voorspellings oor die optimale eksperimentele parameters gemaak word.

Die invloed van aanvanklike ioon volume en snelheidsverspreiding in die twee atoom bronne was deur middel van simulasies ondersoek. Vanuit die resultate is daar waargeneem dat daar 'n noue grens is tussen 'n te groot of te klein ioon volume. Die resolusie van die mass spektra neem af, soos die ioon volume toe neem. Wanneer die aanvanklike ioon, egter, te klein word, begin ruimte ladingsdigtheid 'n rol speel. Dit was ook waargeneem dat die transversale snelheids verspreiding die resolusie van die vlugtyd massa spektrometer gaan beïnvloed. Die transversale snelheidsverspreiding kan deur behoorlike kollimering beperk word.

Die vlugtyd massa spektrometer bevat ook 'n reflektron wat die resolusie van die instrument aansienlik verbeter. Hierdie komponent is noodsaaklik om hoë resolusie spektra te meet. Vanuit die simulasies is daar waargeneem dat die reflektron optimaal werk vir 'n lineêre potensiaal gradient.

Die twee atoom bronne is ook met mekaar vergelyk en afhangend van die doel het elke bron sy eie voordele. Die effusie bron is makliker om te implementeer en daarom is hierdie bron geskik daarvoor om die vlugtyd massa spektrometer te toets in terme van sensitiwiteit asook resolusie. Die Doppler verbreding van spekraallyne vir hierdie bron is egter 'n probleem. Die Doppler verbreding verhoed die selektiewe opwekking en ionisasie van 'n spesifiek isotoop. Die supersoniese gas bron beperk die Doppler verbreding en is noodsaaklik vir die selektiewe opwekking en ionisasie van tin.

Die simulasies het waardevolle insig gelewer oor die invloed van verskeie eksperimentele parameters en sal as grondslag dien vir die opstelling van die vlugtyd mass spektrometer in die toekoms.

Acknowledgements

I would first like to thank my supervisor Dr Christine Steenkamp for all her efforts over the past two years, her continued support and motivation made this study possible. She always encouraged me to formulate my own ideas, delve deeper, and ask the right questions. While the project had its ups and downs, Dr Steenkamp was always on hand to provide the necessary guidance.

Secondly I would like to thank my co-supervisors Dr Rob Bark and Prof Anton du Plessis. Your insight and comments during the writing of this thesis are greatly appreciated. Dr Bark provided valuable insight into the nuclear physics side of this project, something which I am not entirely familiar with. A special thank you to Prof du Plessis who provided financial support during the first year of this study as well as access to the high performance computer lab at the Stellenbosch University CT scanner facility.

A special thank you to my colleagues at the Laser Research Institute at Stellenbosch University for providing an environment that cultivates critical thinking. Your support and suggestions during this study proved extremely valuable. I would like to express my sincere gratitude to the technical staff of the Stellenbosch University Physics Department. Whether it came to soldering some loose wires or sorting out water issues for the Nd:YAG, someone was always on hand to help. A special thanks to Mr Gerhard Louwrens and Mr Laurence Ashworth for your invaluable input regarding the design and construction of the atomic beam sources and other experimental components.

Thank you to the CSIR National Laser Centre Rental Pool Programme for providing financial support to laboratory as well as the CSIR DST-Interbursary Support Programme for providing financial support during 2018.

Finally, I would like to thank my family. To my parents and sister, thank you for your support and motivation. You helped me cross each hurdle that came over my path and without you this would not have been possible.

All glory to God.

Contents

CONTENTS **viii**

List of Figures

List of Tables

Chapter 1

Introduction

1.1   Motivation

The resonance ionization technique is a well established technique for isolation of radioactive isotopes and the production of radioactive ion beams at accelerator facilities worldwide. It is generally termed the isotope separation on-line (ISOL) technique and is used at the ISOLDE facility at CERN, the ISAC facility at TRIUMF in Canada, the IGISOL facility at the University of Jyväskylä in Finland as examples. At CERN a new facility is being developed to focus on the extraction of medical radioisotopes exclusively [1].

In South Africa, iThemba LABS is one of the main contributors in the production and distribution of various long-lived isotopes used in medical applications. iThemba LABS produces medical products based on ^{67}Ga, ^{123}I, ^{22}Na and ^{82}Sr. These isotopes can all be purified by radio-chemical methods. However, chemical separation is not possible or sufficient for some new medical radioisotopes such as ^{225}Ac.

The long term vision is that the current work would serve as a critical preparatory step towards producing and purifying the medical radioactive isotope ^{225}Ac for implementation in cancer therapy. The project is part of a collaboration between the Laser Research Institute at Stellenbosch University and the Radioactive Beams and Radionuclide Production sections of iThemba LABS. Recently,^{225}Ac has been identified as a radionuclide that can be used for medical application [2]. The ^{225}Ac nucleus is an α emitting nucleus. α radiation has been shown to kill cancer cells that are resistant to other therapies including β^- or γ radiation or chemotherapy [3]. There is a clinical study being done in South Africa at the University of Pretoria, led by Prof Mike Sathekge, on targeted α therapy on advanced prostate cancer patients [4]. To date, ^{225}Ac has only been produced at the European Joint Research Centre (JRC) in Karlsruhe, Germany. Production of ^{225}Ac in South Africa would make the new

treatment more accessible to the South African population. It is possible to produce this nuclide at the facilities available at iThemba LABS, but chemical purification is not possible. Therefore resonance ionization must be developed as an alternative.

A dipole mass spectrometer can be used as a spatial mass separator to separate different isotopes based on their mass. A problem arises when isobars are present in the sample. Isobars are isotopes of different elements with the same atomic weight. The dipole mass spectrometer cannot separate isobars and a different technique is needed to be element specific.

Resonance ionization using lasers can be used to ionize a specific element [5]. When combined with a dipole mass spectrometer a specific isotope of a desired element can be produced for further study or for medical application. Resonance ionization schemes have to be developed and optimized for different elements. This can often be achieved using non-radioactive isotopes of the desired element at an offline facility.

The aim of the current project is to develop an offline experiment that can be used for resonance ionization spectroscopy studies and technique development.

The element tin has been selected as a test element to develop an offline RIS setup. While this element is not of interest for medical application, it is of interest in the nuclear physics community. It was observed that nuclei with a magic number of nucleons (protons and neutrons) exhibit enhanced nuclear stability [6] and this led to the formulation of the nuclear shell model [7]. Sn consists of a magic number of protons ($Z = 50$) in its nucleus in terms of the nuclear shell model. It also has two doubly magic isotopes, with a magic number of neutrons as well. The doubly magic isotopes for tin have 50 protons and either 50 or 82 neutrons. The tin nucleus therefore provides an ideal environment to study the evolution of the nuclear shell model from one magic number to the next.

Other than purely nuclear physics research the tin nucleus is also of interest in astrophysics. Recently it has been shown that the rapid proton capture process (rp-process) comes to an end near the doubly magic ^{100}Sn nucleus [8]. The rp-process is a nucleosynthesis process that involves the capture of protons by the nucleus to produce heavier elements [9]. The Sn nucleus can be used to study this process.

RIS will be used to produce ions of non-radioactive tin. The setup to be developed at Stellenbosch University will use a time-of-flight mass spectrometer (ToF-MS) for ion detection. The ToF-MS will be used to obtain the entire mass spectrum of the ionized tin for every laser shot. This will provide information

when investigating the selectivity of the RIS process.

1.2   Aims and objectives

The main motivation behind this project is to characterize a laser based resonance ionization spectroscopy (RIS) setup that can be used to study radioactive isotope separation. The characterization can be done using the non-radioactive element tin (Sn).

To achieve this aim the following set of objectives have been identified:

- Study relevant nuclear and atomic properties of Sn isotopes,

- Identify suitable RIS schemes for Sn,

- Design and set up a laser system for resonance ionization of Sn,

- Design and manufacture apparatus for introducing Sn atoms in the form of an effusive beam or as a seeded jet into a vacuum chamber,

- Simulate the operation of a specific ToF-MS available at Stellenbosch University to investigate and optimize experimental parameters and understand what results to expect,

- Implement the ToF-MS and demonstrate proof of principle experiments.

Chapter 2

Theoretical background

2.1 Nuclear Structure

In the nucleus, protons (with the proton number represented by Z) and neutrons (with the neutron number represented by N) form a complex system of interacting nucleons held together by the strong interaction. The properties of the nucleus can be described by studying the nucleus as a quantum many-body system, but solving such a many-body problem is no easy feat. Many models exist that describe the nucleus such as the liquid-drop model, the Fermi-gas model, and the nuclear shell model. Physicists have long been interested in testing and verifying these models experimentally.

2.1.1 The nuclear shell model

In 1948 it was shown that nuclei consisting of 2, 8, 20, 50, 82 or 126 neutrons or protons have enhanced nuclear stability [6]. These numbers were dubbed the "magic" numbers [7; 10] and it was the starting point for the modern day nuclear shell model. Nuclei with nucleon numbers of 40 and 64 have demonstrated some properties of being "magic" and are often described as "weakly magic" nuclei [11].

Nuclear stability is not the only factor suggesting a shell structure for the nucleus. The nucleon capture cross section for nuclei with a magic number of nucleons is much lower than other nuclei, while nuclei one nucleon shy of being magic have a much larger nucleon capture cross section [11]. Another phenomenon that supports the idea of nuclear shell structure is the low excitation probability between the nuclear ground state and first excited state for nuclei with a magic number of protons or neutrons [11].

The nuclear shell model gives a quantum mechanical description of the nucleus where protons and neutrons will occupy specific shells within the nucleus. Pro-

tons and neutrons fill the shells while adhering to the Pauli exclusion principle similar to electrons filling orbitals in atomic physics. While there is sufficient evidence supporting the idea of a shell model, finding a model that reproduces the magic numbers and other observable nuclear properties is a field of continuing investigation. The starting point for constructing the nuclear shell model, is the so-called independent particle model. The nuclear shell model is often called the "interacting shell model" or the "multiparticle shell model".

The independent particle model

The independent particle model (IPM) describes the nucleus in terms of noninteracting particles (the protons and neutrons) placed in the orbits of a spherically symmetric potential [11], where the potential is a result of all the nucleons within the system. While the IPM is only valid for nuclei with either closed shells or with one nucleon outside of the closed shell it still provides a basis for more complex situations [12]. As with any quantum mechanical system it is necessary to start with the Schrödinger equation, which in a very basic form can be written as follows:

$$\hat{H}|\Psi\rangle = (\hat{T} + \hat{V})|\Psi\rangle = E|\Psi\rangle. \tag{2.1.1}$$

In the equation above $\hat{T}$ refers to the kinetic energy operator, while $\hat{V}$ is the potential energy of the interacting nucleons inside the nucleus. This energy is determined by the inter-nucleon interactions. Since nuclei consist of many nucleons and various interactions, the potential energy will take on the following form:

$$\hat{V} = \sum_{i<j} \hat{V}_{ij} + \sum_{i<j<k} \hat{V}_{ijk} + \dots. \tag{2.1.2}$$

The first term is for the nucleon-nucleon interaction, while the second term describes the three nucleon interaction. The ellipsis take the place of some of the higher order many-body interactions that can take place within the nucleus. The subscripts i, j, k refer to the ith, jth, and kth nucleon.

It is possible to limit the expression above to only include the nucleon-nucleon interaction since it has the biggest contribution to the potential energy, however, recently it has been shown that the three-nucleon interaction can significantly improve the accuracy of *ab initio* calculations for nuclear observables [13]. The potential energy can then be written as:

$$\hat{V} \approx \sum_{i<j} \hat{V}_{ij}. \tag{2.1.3}$$

Even when the Schrödinger equation is made to only include nucleon-nucleon interaction, solving the problem is by no means trivial. The problem can be simplified further by introducing a mean field potential, U_i. This potential

attempts to replace the two nucleon interaction with a potential U_i that only depends on the position of the ith nucleon. The Hamiltonian can then be written as follows:

$$
\begin{aligned}
H &= T + \sum_{i<j} V_{ij} + \sum_i U_i - \sum_i U_i \\
&= T + \sum_i U_i + \sum_{i<j} V_{ij} - \sum_i U_i \\
&= \left(T + \sum_i U_i \right) + \left(\sum_{i<j} V_{ij} - \sum_i U_i \right) \\
&= H_0 + H_{res}.
\end{aligned}
\tag{2.1.4}
$$

In the aforementioned Hamiltonian, H_0 describes a collection of nucleons moving in an averaged potential produced by all the other nucleons within the nucleus. The nucleons move independently from one another in this system. The second part of the Hamiltonian, H_{res}, can be treated as a perturbation on the system of independently moving nucleons.

For the IPM one considers the pertubation, H_{res}, sufficiently small, to such a degree that it can be neglected. The Hamiltonian in equation 2.1.4 then becomes $H = H_0$.

The next hurdle in the construction of the shell model is the shape of the mean field potential, U_i. As with many quantum systems a good starting point is the harmonic oscillator potential.

$$
U(r) = \frac{1}{2} m \omega^2 r^2.
\tag{2.1.5}
$$

The Hamiltonian then becomes:

$$
H = H_0 = T + \frac{1}{2} m \omega^2 r^2.
\tag{2.1.6}
$$

Using the Hamiltonian above and solving the Schrödinger equation, magic numbers are predicted at nucleon numbers of 2, 8, 20, 40, 70, 112, ... [11]. The number of nucleons per shell can be determined from the energy eigenvalues of the harmonic oscillator.

Another option for the potential is that of the infinite square well which takes the following general form:

$$
U(r) = \begin{cases} -U_0 & \text{for } 0 \le r \le a, \\ \infty & \text{elsewhere.} \end{cases}
\tag{2.1.7}
$$

This potential can then be used and the Schrödinger equation can be solved. For the case of the infinite spherical well magic numbers are predicted at 2, 8,

20, 34, 58, 92, 138, ... [11].

Comparing the results above with the experimentally observed magic numbers, it becomes apparent that only the first three magic numbers can be reproduced by either the harmonic oscillator or the spherical well. Therefore a different potential is needed to reproduce the observed magic numbers.

The harmonic oscillator potential can be modified in an attempt to obtain the experimentally observed magic numbers. Phenomenologically it was observed that modifying the harmonic potential by adding an attractive l^2-term, where l refers to the orbital angular momentum of the nucleon [6], flattens out the effective radial shape of the potential [11]. This effect is illustrated in Figure 2.1 which was adapted from [11].
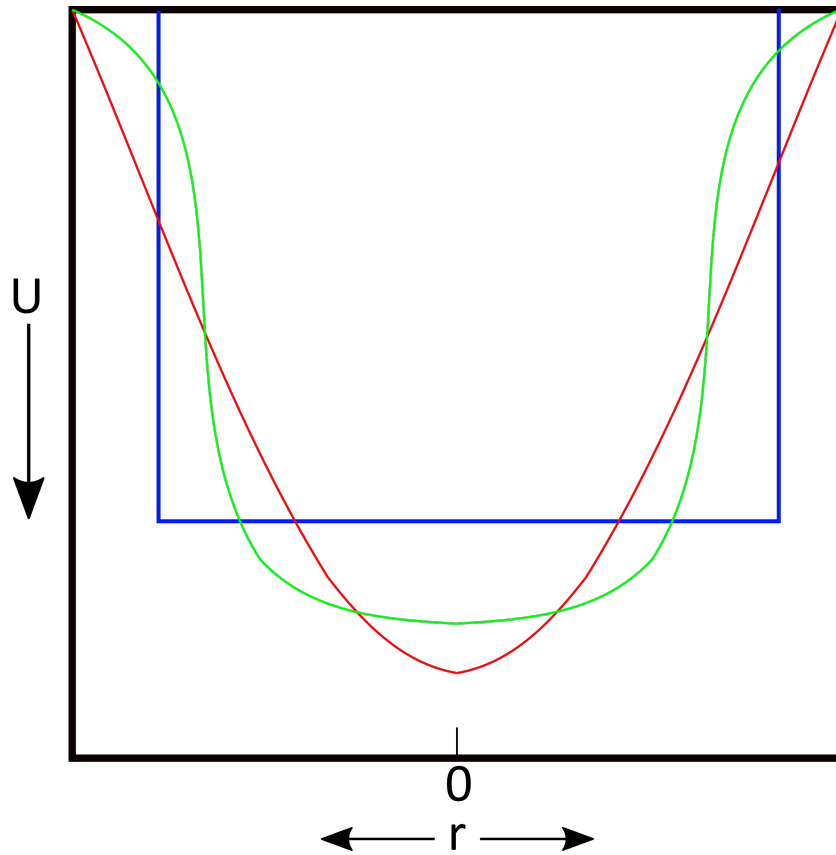
Figure 2.1: Schematic representation of the three nuclear potentials. A square well potential (blue), the simple harmonic oscillator potential (red), and the modified harmonic oscillator potential (green).

As the l^2-term increases with increasing orbital angular momentum, nucleons with high orbital angular momentum feel a stronger attractive interaction.

This attractive interaction lowers the energies of these high orbital angular momentum nucleons. The introduction of the l^2-term produces a hybrid form of both the harmonic oscillator and the infinite square well potential.

The Woods-Saxon potential can be used instead of the modified harmonic oscillator potential [11], but for the purpose of this section the modified harmonic oscillator will be used.

The modified harmonic oscillator potential takes the following form:

$$U(r) = \frac{1}{2}m\omega^2 r^2 + D\vec{l^2}. \tag{2.1.8}$$

While this modified potential is an improvement on the harmonic oscillator potential, the observed magic numbers are not reproduced and another term is needed to reproduce them. It is known that nucleons are half-integer spin particles, i.e. fermions, and therefore a sensible modification to the potential described in equation 2.1.8 would be to include spin-orbit coupling. For this the nucleon spin, $\vec{s}$, and orbital angular momentum, $\vec{l}$, are coupled together to form the total angular momentum, $\vec{j}$. This interaction produces a new term that can be added to equation 2.1.8. When it comes to the spin-orbit interaction, the force felt by any given nucleon differs depending on whether the spin and orbital angular momenta are aligned parallel or anti-parallel [11]. To produce the magic numbers, a parallel configuration is chosen, as this lowers the energy. The spin-orbit potential can then be written in the following form:

$$U_{l \cdot s} = -U_{ls}\vec{l} \cdot \vec{s}. \tag{2.1.9}$$

In equation 2.1.9 $-U_{ls}$ is just a strength constant. The potential then takes the following form:

$$U(r) = \frac{1}{2}m\omega^2 r^2 + D\vec{l^2} + C\vec{l} \cdot \vec{s}. \tag{2.1.10}$$

Equation 2.1.10 represents a realistic shell model potential that can be used to produce the correct magic numbers of 2, 8, 20, 50, 82, and 126 [6].
In equation 2.1.10 D and C are just constants. The independent particle model, as constructed above, is quite useful and can be used to explain various phenomena across the nuclear chart. The IPM, however, can be improved by including many body interactions. The many body interactions fall outside the scope of the project, and will not be discussed.

2.1.2   Tin (Sn) as a test case in nuclear physics

From experimental data it has become clear that nuclei with magic nucleon numbers have enhanced stability [6]. Sn has a magic number of protons

($Z = 50$) in its nucleus, and therefore enhanced nuclear stability. The stability of the Sn nucleus causes it to have the largest number of stable isotopes (10 stable isotopes) of all the elements, and in addition a relatively large number (31) of known unstable isotopes. The tin isotopes, their lifetimes, and their natural abundances if stable have been listed in Table 2.1. The data were obtained from the Nuclear Data Services provided by the International Atomic Energy Agency [14].

Because of the unique properties of tin, the tin nucleus has been studied numerously in the past couple of years. In recent years nuclei within $Z = N = 50$ region of the Segré chart of nuclides have been studied extensively [15; 16; 17; 18; 19], both experimentally and theoretically. The term "doubly magic nuclei" refer to nuclei consisting of magic numbers for both protons and neutrons. In the $Z = N = 50$ region the doubly magic nucleus of interest, is the ^{100}Sn nucleus. This nucleus is the heaviest self-conjugate ($N = Z$) doubly magic nucleus [20]. The ^{100}Sn nucleus provides an ideal environment to understand and test nuclear shell structure [21] as well as astrophysical processes [8]. Some of these processes include the rapid proton capture process (rp-process) and nuclear processes like α-decay and Gamow-Teller transitions taking place in stars.

Recently it has been shown that the rapid proton capture process comes to an end near the ^{100}Sn nucleus [8]. The rp-process is a series of nucleosynthesis processes that involves the capture of protons by a nucleus to produce heavy elements [9]. One of the proton capture processes that involve the tin nucleus can be written down as follows [22]

$$^{106}_{50}Sn + p \rightarrow ^{107}_{51}Sb + \gamma, \tag{2.1.11}$$

where a γ ray is emitted as the proton is captured.

Another reason physicists are interested in the ^{100}Sn nucleus, is because of its position within the nuclear landscape. This nucleus is located near the proton dripline [23]. These driplines indicate the number of protons or neutrons where nuclear binding ends. Astrophysical processes, such as the aforementioned rp-process, take place in the areas close to these driplines [24]. Therefore the structure of nuclei close to these driplines are of interest since it has a direct impact on the formation of heavier elements within the universe [23].

The ^{100}Sn nucleus and surrounding nuclei are also the terminal point for a collection of nuclei, such as ^{105}Te and ^{109}Xe , exhibiting enhanced α-decay [25; 26]. These results provided the opportunity to continue the search for superallowed α-decay [26]. The observed α-decay of ^{105}Te can be written as

$$^{105}_{52}Te \rightarrow ^{101}_{50}Sn + ^{4}_{2}He. \tag{2.1.12}$$

Table 2.1: The tin isotopes

Isotope	Lifetime	Natural abundance (if stable) %
^{99}Sn	760 ns	N/A
^{100}Sn	1.16 s	N/A
^{101}Sn	1.7 s	N/A
^{102}Sn	3.8 s	N/A
^{103}Sn	7.0 s	N/A
^{104}Sn	20.8 s	N/A
^{105}Sn	34 s	N/A
^{106}Sn	115 s	N/A
^{107}Sn	2.9 min	N/A
^{108}Sn	10.3 min	N/A
^{109}Sn	18.1 min	N/A
^{110}Sn	4.15 h	N/A
^{111}Sn	35.3 min	N/A
^{112}Sn	Stable	0.97
^{113}Sn	115 days	N/A
^{114}Sn	Stable	0.65
^{115}Sn	Stable	0.36
^{116}Sn	Stable	14.53
^{117}Sn	Stable	7.68
^{118}Sn	Stable	24.22
^{119}Sn	Stable	8.85
^{120}Sn	Stable	32.59
^{121}Sn	27 h	N/A
^{122}Sn	Stable	4.63
^{123}Sn	129 days	N/A
^{124}Sn	Stable	5.79
^{125}Sn	9.6 days	N/A
^{126}Sn	2.3×10^5 years	N/A
^{127}Sn	2.1 h	N/A
^{128}Sn	59 min	N/A
^{129}Sn	2.23 min	N/A
^{130}Sn	3.72 min	N/A
^{131}Sn	56 s	N/A
^{132}Sn	1.05 s	N/A
^{133}Sn	1.46 s	N/A
^{134}Sn	1.05 s	N/A
^{135}Sn	0.92 s	N/A
^{136}Sn	0.29 s	N/A
^{137}Sn	190 ms	N/A
^{138}Sn	140 ms	N/A
^{139}Sn	130 ms	N/A

Table 2.2: The tin isotopes studied through laser spectroscopy

Isotopes of tin	Spectroscopic technique used
$101 - 103, 108$	HC RILIS at GSI
$105 - 111, 113, 117, 119, 121, 123, 125 - 138$	HC RILIS at CERN
$125 - 132$	ABPL
$107 - 111, 113, 121$	HC RILIS at TRIUMF

As mentioned above, the ^{100}Sn nucleus provides an ideal opportunity to study Gamow-Teller transitions. Gamow-Teller transitions are a specific set of β-decays [27]. These transitions describe the process of a proton transforming into a neutron or the other way around. An example of a Gamow-Teller transition would be

$$^{105}_{50}Sn \rightarrow^{105}_{49} In + \beta^+ + \upsilon_e \tag{2.1.13}$$
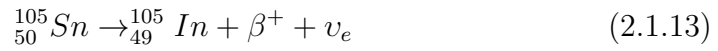
where υ_e represents the electron neutrino.

Gamow-Teller transitions are relevant in the study of the electron capture process that takes place during collapse of massive stars. This process is regulated by Gamow-Teller transitions. An example of an electron capture process will be

$$^{107}_{50}Sn + e^- \rightarrow^{107}_{49} In + \upsilon_e, \tag{2.1.14}$$
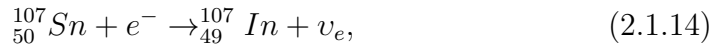
where e^- refers to the electron and υ_e to the electron neutrino.

A more in depth understanding of Gamow-Teller transitions can also provide a necessary constraint on the mass of the neutrino, should neutrinoless double β-decay ever be observed [28].

The ^{100}Sn nucleus and surrounding nuclei also play an important role in the understanding and testing of nuclear structure and nuclear models. Laser spectroscopy has been applied to various Sn isotopes [29; 30; 31]. The different isotopes that have been studied as well as the laser spectroscopic technique used to study them are listed in Table 2.2 [32]. In table 2.2 HC RILIS refers to the Hot Cavity Resonance ionization laser ion source, and ABPL refers to measurements taken using atomic beam being probed with a pulsed laser system. The table was reproduced from the data listed in [32]. The facility at which the measurement took place is also indicated.

Through laser spectroscopy experiments various properties of the nucleus can be determined. These properties include the spin of the nuclear ground state, nuclear moments, and the nuclear charge radii. For doubly magic nuclei these properties carry significant importance, as they form an integral part in mean-field calculations [33; 34; 35] that can be used to calculate ground state prop-

erties for various other nuclei found on the nuclear chart.

On the heavier side of the Segré chart the doubly magic ^{132}Sn nucleus is also of interest. This nucleus consists of 50 protons and 82 neutrons. Numerous studies have been done to probe and explore the ground state properties of the tin nucleus in this region [36; 37; 38].

2.2 Atomic Structure

Moving up in scale from the nucleus, atomic physics is used to describe the electron-electron interaction as well as the interaction between the nucleus and the surrounding electrons. To describe the observed atomic energy levels and atomic phenomenon an in depth understanding of the interaction between all the electrons of an atom and the nucleus as well as with each other is needed. A good starting point to try and explain atomic phenomenon is the Schrödinger equation.

2.2.1 The Schrödinger equation

An electron of mass m_e in a spherically symmetric potential can be described by the following Schrödinger equation

$$H \left| \Psi \right\rangle = \left(\frac{-\hbar^2}{2m_e} \nabla^2 - V(r) \right) \left| \Psi \right\rangle = E \left| \Psi \right\rangle, \tag{2.2.1}$$

where the first term describes the kinetic energy and the second term describes the potential energy due to the attraction between the nucleus and a single electron.

The expression above essentially describes the hydrogen atom in its ground state. A description of $V(r)$ can be found in numerous atomic physics textbooks (see [39]). In spherical polar coordinates ∇^2 can be expressed as follows

$$\nabla^2 = \frac{1}{r^2} \frac{\partial}{\partial r} \left(r^2 \frac{\partial}{\partial r} \right) + \frac{1}{r^2} \left[\frac{1}{\sin\theta} \frac{\partial}{\partial \theta} \left(\sin\theta \frac{\partial}{\partial \theta} \right) + \frac{1}{\sin^2\theta} \frac{\partial^2}{\partial^2\phi} \right]. \tag{2.2.2}$$

The Schrödinger equation in equation 2.2.1 is essentially a differential equation that can be solved using the separation of variables technique. The problem, however, is that the Schrödinger equation becomes tougher to solve for atoms with more than one or two orbiting electrons.

The Hamiltonian for an atom with N electrons takes the following form

$$H = \sum_{i=1}^{N} \left\{ -\frac{\hbar}{2m_e} \nabla_i^2 - \frac{Ze^2}{4\pi\epsilon_0 r_i} + \sum_{j>i}^{N} \frac{e^2}{4\pi\epsilon_0 r_{ij}} \right\}. \tag{2.2.3}$$

Where:

∇^2 is defined in equation 2.2.2.

Z the number of protons in the nucleus.

e refers to the electron charge.

ϵ_0 is the permittivity of free space.

r_i refers to the position of the ith electron.

r_{ij} refers to the distance between the ith and the jth electron and is defined as $r_{ij} = |\vec{r_i} - \vec{r_j}|$.

In equation 2.2.3 $-\frac{\hbar}{2m_e}\nabla_i^2$ describes the kinetic energy, $-\frac{Ze^2}{4\pi\epsilon_0 r_i}$ describes potential energy due to the attraction between the nucleus and electrons, and $\sum_{j>i}^{N} \frac{e^2}{4\pi\epsilon_0 r_{ij}}$ describes the repulsion between the electrons.

To simplify the problem the Hamiltonian can be split into three distinct parts such that it takes the following form [39]

$$H = H_{CF} + H_{Re} + H_{SO}. \qquad (2.2.4)$$

The first term in equation 2.2.4 refers to the central field Hamiltonian stemming from the central-field approximation. The central field approximation assumes that a part of the repulsion between electrons can be treated as a central potential [39]. The filled electron shells around the nucleus have a spherical charge distribution; because of this the interaction between the valence electrons and the filled shells and nucleus should also be spherically symmetric. Therefore the central field Hamiltonian covers the radial part of the Coulomb repulsion between the electrons.

$$H_{CF} = \sum_{i=1}^{N} \left\{ -\frac{\hbar^2}{2m_e}\nabla_i^2 - \frac{Ze^2}{4\pi\epsilon_0 r_i} + S(r_i) \right\}. \qquad (2.2.5)$$

In the equation above $S(r)$ is the central potential introduced via the central field approximation and the rest of the symbols are as defined for equation 2.2.3.

The second term in equation 2.2.4 is the so-called residual electrostatic interaction Hamiltonian. This part of the total Hamiltonian describes the angular part of the Coulomb interaction between all the electrons and can be described as follows:

$$H_{Re} = \sum_{i=1}^{N} \left\{ \sum_{j>i}^{N} \frac{e^2}{4\pi\epsilon_0 r_{ij}} - S(r_i) \right\}. \qquad (2.2.6)$$

The last term in equation 2.2.4 describes the spin-orbit interaction of the unpaired valence electrons surrounding the nucleus. Electrons are fermions with spin $s = \frac{1}{2}$ and these particles move in the potential generated by the nucleus and the other electrons. The spin-orbit interaction can be expressed by

$$H_{SO} = \sum_{i=1}^{N} \beta_i \vec{s_i} \cdot \vec{l_i}, \tag{2.2.7}$$

where:

β_i refers to the fine structure constant.

$\vec{s_i}$ refers to the spin of the ith electron.

$\vec{l_i}$ refers to the orbital angular momentum of the ith electron.

The central field Hamiltonian has a bigger contribution to the energy of the system than the remaining two parts of the total Hamiltonian, such that

$$E_{CF} \gg E_{Re} \qquad \text{and} \qquad E_{CF} \gg E_{SO}. \tag{2.2.8}$$

Both the residual electrostatic interaction and the spin-orbit interaction can be treated as perturbations on a system described by the central field Hamiltonian, H_{CF}. The order in which these perturbations act on the system depends on the impact of both the interactions on the system. There exists two main possibilities, namely

$$E_{Re} \gg E_{SO} \qquad \text{and} \qquad E_{SO} \gg E_{Re}. \tag{2.2.9}$$

In the regime where $E_{Re} \gg E_{SO}$, the residual electrostatic interaction is treated as a perturbation on H_{CF}. The spin-orbit interaction is then treated as another perturbation on the system described by $H_{CF} + H_{Re}$. In this regime Russell-Saunders or LS-Coupling is used to describe the system.

In the second regime, $E_{SO} \gg E_{Re}$, the spin-orbit interaction acts as a perturbation on the central field. The residual electrostatic interaction is treated as a perturbation on the system described by $H_{CF} + H_{SO}$. In this regime jj-coupling is used to describe the system.

In both of these cases the starting point is the central field Hamiltonian. The Schrödinger equation can be written as

$$H_{CF} \left| \psi_{CF} \right\rangle = E_{CF} \left| \psi_{CF} \right\rangle. \tag{2.2.10}$$

The eigenstates for this system are the electronic configuration.

$$\left| \psi_{CF} \right\rangle = \left| n_1 l_1, n_2 l_2, \ldots, n_N l_N \right\rangle. \tag{2.2.11}$$

Where n and l are the principle and orbital angular momentum quantum numbers. The electron configuration can be shortened for convenience sake to γ. The eigenstates for the central field can then be represented as

$$|\psi_{CF}\rangle = |n_1 l_1, n_2 l_2, \ldots, n_N l_N\rangle = |\gamma\rangle. \tag{2.2.12}$$

LS-Coupling

As mentioned previously, in the LS-coupling regime the residual electrostatic interaction acts as a perturbation on the central field. Due to the electrostatic repulsion, the interaction between the electrons causes their orbital angular momenta, $\vec{l_i}$, to change. The total orbital angular momentum of the atom, however, stays the same and can then described by the following:

$$\vec{L} = \sum_i \vec{l_i}. \tag{2.2.13}$$

Similarly the total spin angular momentum of the atom can be described as follows:

$$\vec{S} = \sum_i \vec{s_i}. \tag{2.2.14}$$

When considering multi-electron atoms, only unpaired electrons contribute to the total orbital and spin angular momenta. Therefore only valence electrons are considered when using equations 2.2.13 and 2.2.14.

With H_{Re} acting on the system, n and l are no longer sufficient quantum numbers to describe the system. From a classical approach the orbital and spin angular momenta in the system stay conserved. Quantum mechanically this implies the following:

$$\left[L^2, H_{Re}\right] = 0 \qquad and \qquad [L_z, H_{Re}] = 0, \tag{2.2.15}$$

$$\left[S^2, H_{Re}\right] = 0 \qquad and \qquad [S_z, H_{Re}] = 0. \tag{2.2.16}$$

The associated magnetic quantum numbers governing the orientation of $\vec{L}$ and $\vec{S}$ in an external magnetic field are given by M_L (with values $L, L-1, \ldots, -L$) and M_S (with values $S, S-1, \ldots, -S$). Thus in the LS-Coupling scheme the $L, M_L, S,$ and M_S quantum numbers are well defined. Therefore the eigenstates for H_{Re} are $|\gamma, L, M_L, S, M_S\rangle$. In this scheme it is also quite useful to label the energy levels of the atom in question with these quantum numbers. These labelled energy levels are then called terms. The term values can be expressed as follows:

$$^{2S+1}L \tag{2.2.17}$$

where

S is the total spin angular momentum,

L is the total orbital angular momentum.

$2S + 1$ is referred to as the spin multiplicity.

For different values of the L-quantum number the term values in equation 2.2.17 changes. For the quantum number $L = 0, 1, 2, \ldots$, the L in spectroscopic notation (2.2.17) becomes $S, P, D, \ldots$.

Thus far only the central field and the residual electrostatic interaction have been accounted for. The spin-orbit interaction still needs to be introduced. The coupling between the spin of the electron and its intrinsic orbital angular momentum, l, leads to the fine structure observed in atomic spectra. As mentioned previously the spin-orbit interaction acts perturbatively on $|\gamma, L, M_L, S, M_S\rangle$.

$$\langle \gamma, L, M_L, S, M_S | H_{SO} | \gamma, L, M_L, S, M_S \rangle . \tag{2.2.18}$$

The problem however is that H_{SO} does not commute with L_z or S_z.

$$[L_z, H_{SO}] \neq 0 \qquad \text{and} \qquad [S_z, H_{SO}] \neq 0. \tag{2.2.19}$$

Therefore L_z and S_z are no longer good quantum numbers to describe the system. The basis for the eigenstate should be changed. To do this the total electronic angular momentum of the atom is introduced. The total electronic angular momentum for the system stays constant and can be expressed as the vector sum of the orbital angular momentum and the spin angular momentum.

$$\vec{J} = \vec{L} + \vec{S}. \tag{2.2.20}$$

With possible J-values from $|L - S|, \ldots, L + S$. The conservation of the total electronic angular momentum implies that

$$\left[J^2, H_{SO} \right] = 0 \qquad \text{and} \qquad [J_z, H_{SO}] = 0. \tag{2.2.21}$$

The eigenstates then become $|\gamma, L, S, J, M_J\rangle$. The spin-orbit interaction then implies that the term values described in equation 2.2.17 are degenerate. The degeneracy stems from the associated magnetic quantum number M_J with $2J + 1$ values (with values $J, J - 1, \ldots, -J$). The term value from equation 2.2.17 can be changed to include J values:

$$^{2S+1}L_J. \tag{2.2.22}$$

The energy shift from the ^{2S+1}L term to the $^{2S+1}L_J$ fine structure level can then be determined by

$$E_{FS} = \beta_{LS} \langle \vec{S} \cdot \vec{L} \rangle, \tag{2.2.23}$$

where $\langle \vec{S} \cdot \vec{L} \rangle$ refers to the expectation value and β_{LS} is the fine structure constant. Evaluating the expression above with the eigenstates $|\gamma, L, S, J, M_J\rangle$, the energy splitting from the unperturbed ground state can be determined as

$$E_{FS} = \frac{\beta_{LS}}{2}\{J(J+1) - L(L+1) - S(S+1)\}. \qquad (2.2.24)$$

The energy shift between subsequent J-Levels with the same L and S values can then be expressed as

$$\delta E_{FS} = E_J - E_{J-1} = \beta_{LS}J. \qquad (2.2.25)$$

This is often referred to as the interval rule for fine structure.

jj-Coupling

In the LS-Coupling scheme the residual electrostatic interaction was treated as a perturbation on the central field, followed by the spin-orbit interaction acting on the system. In the jj-Coupling scheme the order of perturbation is reversed. The spin-orbit interaction becomes stronger as the atom becomes heavier [39]. Because of this the LS-coupling scheme generally holds for light atoms and the jj-coupling scheme for heavy atoms.

In the regime where $E_{SO} \gg E_{Re}$ the spin-orbit interaction must be considered before the residual electrostatic interaction. The spin-orbit interaction causes the orbital angular momentum and spin angular momentum of individual electrons to be coupled together,

$$\vec{j_i} = \vec{l_i} + \vec{s_i}. \qquad (2.2.26)$$

The eigenstates of the $H_{CF} + H_{SO}$ system are given by $|\gamma, j_1 m_1, j_2 m_2, \ldots, j_N m_N\rangle$ where m_N is the magnetic quantum number of the Nth electron. The residual electrostatic interaction acts as a perturbation on the system and the angular momenta of the electrons are coupled together to give the total angular momentum, J, where

$$J = \sum_i j_i. \qquad (2.2.27)$$

Following the introduction of the electrostatic interaction the eigenstates of the system also changes. The eigenstates describing the system now become $|\gamma, j_1, j_2, \ldots, j_N, J, M\rangle$.

2.2.2   Electron configuration of the tin atom

With the background of atomic physics outlined in the previous section, the tin (Sn) atom is considered. In the previous section a distinction between LS- and jj-coupling was made, with *LS*-coupling working better for light atoms

and jj-coupling working better for heavier atoms. Tin, however, does not fall purely into either regime, therefore neither scheme describes the atom perfectly [39]. LS-coupling will be used to describe the atom in this section, as this is the generally accepted labelling scheme in atomic physics.

The ground state electron configuration of the tin atom can be written as follows:
$$1s^2 2s^2 2p^6 3s^2 3p^6 3d^{10} 4s^2 4p^6 4d^{10} 5s^2 5p^2. \tag{2.2.28}$$
This can be abbreviated to
$$[Kr]\, 4d^{10} 5s^2 5p^2 \tag{2.2.29}$$
where $[Kr]$ represents the electron configuration of krypton. For the tin atom both the $4d$ and $5s$ shells are filled with electrons. Therefore in the LS-coupling scheme only the two valence electrons in the $5p$-shell are considered. In the ground state both the electrons are in a p-orbital and therefore they can be described with the following set of quantum numbers:

$$l_1 = l_2 = 1,$$
$$m_{l1} = +1,$$
$$m_{l2} = 0,$$
$$s_1 = s_2 = \frac{1}{2},$$
$$m_{s1} = m_{s2} = +\frac{1}{2}.$$

The electrons fill separate p-orbitals following Pauli's exclusion principle. Generally p-orbitals have orbital angular momentum $l = 1$. To have the lowest energy the electrons will have parallel spin according to Hund's rule. Therefore, the unpaired electrons are assigned m_s-values of $+\frac{1}{2}$. According to Pauli's exclusion principle these electrons will have different m_l-values.

To describe the atomic ground state in the LS-coupling scheme the total orbital angular momentum and total spin are needed. The total orbital angular momentum is given by $\vec{L} = \vec{l}_1 + \vec{l}_2$. Due to the different allowed orientations of $\vec{l}_1$ and $\vec{l}_2$, as illustrated in Figures 2.2, 2.3, and 2.4, the L quantum number can have values
$$L = l_1 + l_2, \ldots, |l_1 - l_2|, \tag{2.2.30}$$
where the magnitude of $\vec{l}_i$ is defined as
$$|l_i| = \hbar\sqrt{l_i(l_i + 1)}, \tag{2.2.31}$$
and the magnitude of the total orbital angular momentum is defined as
$$\left|\vec{L}\right| = \hbar\sqrt{L(L + 1)}. \tag{2.2.32}$$
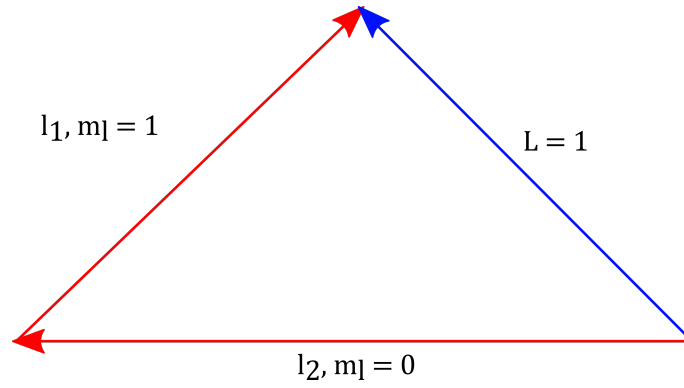
Figure 2.2: Schematic representation of the coupling between l_1 and l_2 for the ^3P ground state, yielding $L = 1$.
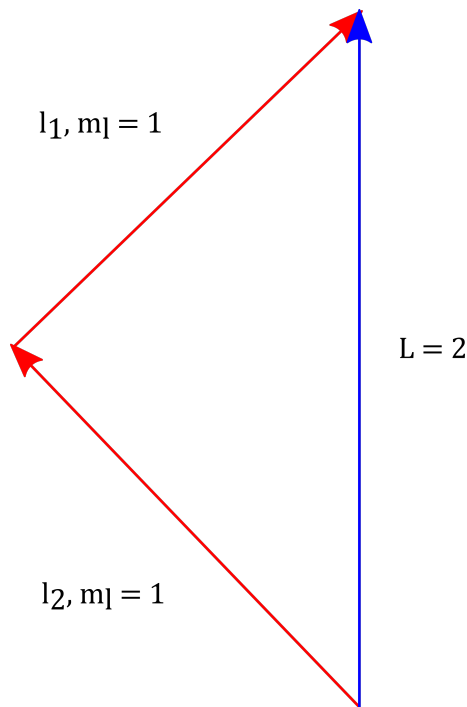
Figure 2.3: Schematic representation of the coupling between l_1 and l_2 for the ^1D state, yielding $L = 2$.

The ground state of tin has $L = 1$ [40], for which the coupling is illustrated in Figure 2.2. In spectroscopic notation (see equation 2.2.22) this corresponds to term symbol P.

Similarly the coupling to form the total spin angular momentum can be illustrated using a vector model and this was done in Figure 2.5. In the P state the spins are unpaired as illustrated in Figure 2.5 yielding a total spin quantum
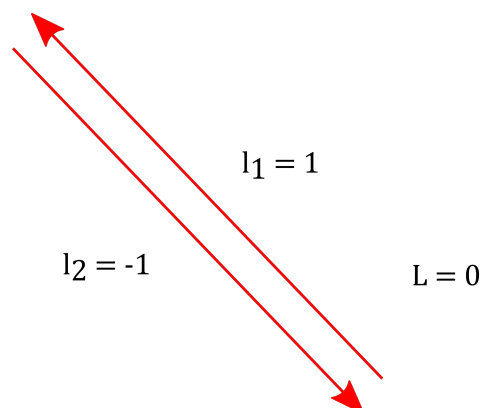
Figure 2.4: Schematic representation of the coupling between l_1 and l_2 for the ^1S state, yielding $L = 0$.

number $S = 1$. In spectroscopic notation the multiplicity $2S + 1 = 3$ is used, which implies that the tin atom has a triplet ground state, ^3P.
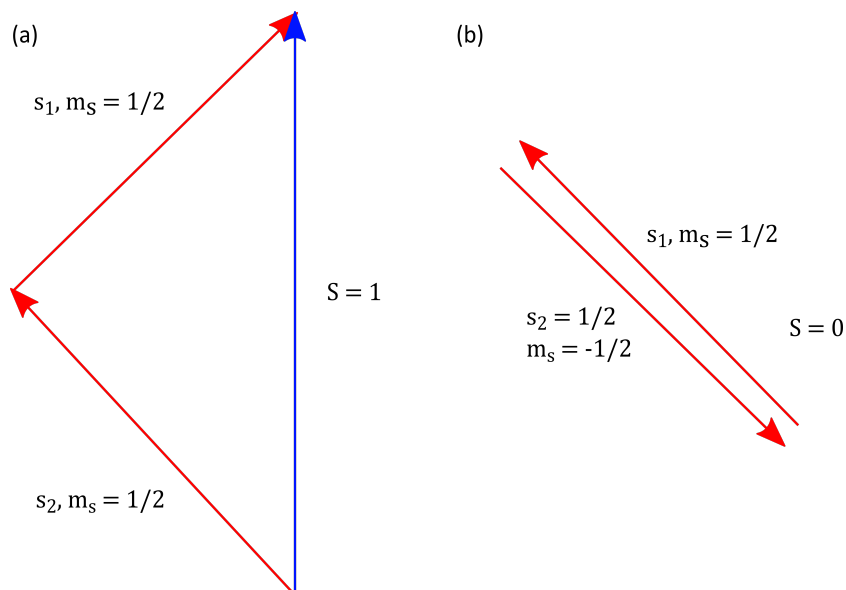
Figure 2.5: Vector representation of the coupling between s_1 and s_2. Diagram (a) is termed "unpaired spins" and diagram (b) is termed "paired spins".

Finally the total orbital angular momentum is needed. As mentioned previously the possible J-values are $|L - S|, \ldots, L + S$. For the tin atom ground state with $L = 1$, $S = 1$

$$J = |L - S|, |L - S| + 1, L + S$$
$$= 0, 1, 2$$

represents the possible J-values of the ground state. The triplet ground state of the tin atom can then be described fully as

$$[Kr]\,4d^{10}5s^25p^{2\,3}P_{0,1,2}. \tag{2.2.33}$$

Energetically, tin atoms are most likely to occupy the lowest J level. Therefore the $5p^{2\,3}P_0$ level is considered as the ground state of the atom.

The alternative coupling of the angular momenta forms the next two energy states of Sn. The ^3D state has $L = 2$ (Figure 2.3) and $S = 1$ (Figure 2.5(a)), with $J = 1, 2, 3$. The complete description is

$$[Kr]\,4d^{10}5s^25p^{2\,3}D_{1,2,3}. \tag{2.2.34}$$

The ^1S state has $L = 0$ (Figure 2.4). $S = 0$ (Figure 2.5(b)) due to the Pauli exclusion principle, therefore $J = 0$. The complete description is

$$[Kr]\,4d^{10}5s^25p^{2\,1}S_0. \tag{2.2.35}$$

2.3 Influence of the nuclear properties on the atomic energy levels

Laser spectroscopy is a versatile and useful tool that can be used to learn more about matter and its properties. This is especially true in nuclear physics research, where optical techniques can be used to determine several nuclear ground state and long lived isomeric state properties. These properties include the nuclear spin, magnetic dipole moments, and changes in the mean-square charge radius of the nucleus. Systematically studying these ground state properties provides valuable insight into the structure of the nucleus, meaning that various nuclear models can be adjusted and updated. Measurements of these ground state nuclear properties can also help to map out whole regions of the Segré chart of nuclides [41]. These properties will be discussed below, followed by a brief discussion on how lasers can be used to extract them.

2.3.1 Nuclear spin, nuclear moments and hyperfine structure

Similar to electrons in atomic physics, protons and neutrons occupy orbitals within the nucleus. Therefore, nucleons can be characterized by their orbital angular momentum, $\vec{l}$, and spin angular momentum, $\vec{s}$. These angular momenta couple to form the total angular momentum of the nucleon, $\vec{j_i}$. The nuclear spin, $\vec{I}$, is the total angular momentum of the nucleus resulting from the coupling of the total angular momentum of all the nucleons in the nucleus.

$$\vec{I} = \sum_i \vec{j_i}. \tag{2.3.1}$$

Nucleons pair up in a similar fashion to electrons in atomic orbitals. Pairing leading to a total nuclear spin of 0 is preferred. Therefore only the angular momenta of valence nucleons contribute to the spin of the nucleus.

The interaction between the nucleus and the surrounding electrons results in a further splitting of the fine structure levels into hyperfine structure levels.

The hyperfine interaction can be expressed in terms of the magnetic field generated by the atomic electrons and the magnetic moment of the nucleus,

$$H_{HFS} = -\vec{\mu_I} \cdot \vec{B_E} \tag{2.3.2}$$

where $\vec{\mu_I}$ represents the magnetic moment of the nucleus and $\vec{B_E}$ the magnetic field generated by the electrons. The magnetic moment of the nucleus will be discussed further in the next section. The magnetic field generated by the electrons is proportional to $\vec{J}$, with prefactors [39]. Evaluating equation 2.3.2 leads to

$$H_{HFS} = -\frac{\mu_I B_E}{IJ} \vec{I} \cdot \vec{J}. \tag{2.3.3}$$

The hyperfine interaction can then be expressed as

$$H_{HFS} = -A\vec{I} \cdot \vec{J}, \tag{2.3.4}$$

where A is the hyperfine parameter, defined as $\frac{\mu_I B_E}{IJ}$. The hyperfine interaction acts on the system described by the eigenstates $|\gamma, L, S, J, M_J\rangle$. Similar to the fine structure case described in the previous section, the hyperfine interaction causes the nuclear spin angular momentum, $\vec{I}$, and the atomic angular momentum, $\vec{J}$ to couple. The total angular momentum, however, stays the same. The total angular momentum, $\vec{F}$, can be defined as

$$\vec{F} = \vec{I} + \vec{J}, \tag{2.3.5}$$

with possible F-values ranging from $|I - J|$ to $|I + J|$. Once again the problem arises that H_{HFS} does not commute with either I_z or J_z, or symbolically

$$[I_z, H_{HFS}] \neq 0 \qquad \text{and} \qquad [J_z, H_{HFS}] \neq 0. \tag{2.3.6}$$

This implies that M_I and M_J are not sufficient to describe the system. The conservation of the total angular momentum leads to

$$\left[F^2, H_{HFS}\right] = 0 \qquad \text{and} \qquad [F_z, H_{HFS}] = 0. \tag{2.3.7}$$

The eigenstates needed to describe the system with the hyperfine interaction then becomes $|\gamma, I, J, F, M_F\rangle$.

To determine the energy eigenvalues of the hyperfine levels the expectation value of equation 2.3.4 should be calculated.

$$
\begin{aligned}
E_{HFS} &= A\langle \vec{I} \cdot \vec{J} \rangle \\
&= \frac{A}{2}\{F(F+1) - I(I+1) - J(J+1)\} \\
&= \frac{1}{2}AK,
\end{aligned}
\tag{2.3.8}
$$

where $\{F(F+1) - I(I+1) - J(J+1)\}$ is abbreviated to K. The expression above is quite similar to the result obtained for the fine structure (see equation 2.2.24). The hyperfine structure also follows a similar interval rule to the fine structure.

$$
\delta E_{HFS} = E_F - E_{F-1} = AF.
\tag{2.3.9}
$$

Other than the magnetic dipole moment, the non-spherical charge distribution within the nucleus gives rise to an electric quadrupole moment, Q, which has a further influence on the hyperfine structure of the atom. The electric quadrupole moment will be discussed further in a following section. The change in the energy eigenvalues due to the introduction of the electric quadrupole moment can be summarized as

$$
\begin{aligned}
\delta E_{QM} &= eQV_{zz} \frac{3(K(K+1) - 4I(I+1)J(J+1))}{8I(2I-1)J(2J-1)}, \\
&= B \frac{3(K(K+1) - 4I(I+1)J(J+1))}{8I(2I-1)J(2J-1)},
\end{aligned}
\tag{2.3.10}
$$

where the hyperfine B-parameter was defined as eQV_{zz}, Q as the electric quadrupole moment and V_{zz} as the electric field gradient at the nucleus. With the consideration of the electric quadrupole moment the energy eigenvalue of the hyperfine levels can be given as

$$
E_{HFS} = \frac{1}{2}AK + B\frac{3(K(K+1) - 4I(I+1)J(J+1))}{8I(2I-1)J(2J-1)}.
\tag{2.3.11}
$$

The magnetic dipole moment

As mentioned in the previous section the magnetic dipole moment of the nucleus influences the interaction between the nucleus and the magnetic field generated by the surrounding electrons. The magnetic dipole moment is given by [42]

$$
\vec{\mu_I} = g_I \mu_N \vec{I},
\tag{2.3.12}
$$

with g_I the nuclear spin g-factor, μ_N the nuclear magneton, and $\vec{I}$ the nuclear spin.

Stellenbosch University https://scholar.sun.ac.za

The protons orbiting within the nucleus and the intrinsic spin of both protons and neutrons contribute to the nucleus becoming magnetized. In terms of these contributions, the magnetic dipole operator can then be defined as [43]:

$$\vec{\mu} = \sum_{i=1}^{A} g_L^i \vec{L^i} + \sum_{i=1}^{A} g_S^i \vec{S^i}. \tag{2.3.13}$$

In the expression above the gyromagnetic factors, g_L and g_S, differ for protons and neutrons. For protons $g_L^p = 1$ and $g_S^p = +5.587$, while for neutron $g_L^n = 0$ and $g_S^n = -3.826$ [43]. The spectroscopic magnetic dipole moment, used in equation 2.3.3, is then defined as the expectation value of the z-component of the dipole operator defined in 2.3.13 [43],

$$\mu_I = \langle I, M = I | \vec{\mu_z} | I, M = I \rangle$$
$$= \left(\frac{I}{I+1}\right)^{\frac{1}{2}} \langle I | |\vec{\mu}| | I \rangle, \tag{2.3.14}$$

where the Wigner-Eckart Theorem has been used to go from the first to the second line. From this expression it becomes clear that nuclei with $I = 0$ have no magnetic dipole moment.

The electric quadrupole moment

In the previous section it was mentioned that not only the magnetic dipole moment influences the hyperfine splitting of an atom, the electric quadrupole moment also plays a part. The non-spherical charge distribution in a nucleus gives rise to an electric quadrupole moment. The electric quadrupole moment in Cartesian coordinates can be defined as [44]

$$Q_z = \sum_{i=1}^{A} e_i(3z_i^2 - r_i^2), \tag{2.3.15}$$

where e_i represents the charge of the ith nucleon located at position (x_i, y_i, z_i). However it is somewhat easier to represent the electric quadrupole moment in terms of spherical tensors. In a spherical tensor basis the quadrupole moment can be expressed as the zero order tensor component of a rank 2 tensor [43]

$$Q_z = \sqrt{\frac{16\pi}{5}} \sum_{i=1}^{A} e_i r_i^2 Y_2^0(\theta_i, \phi_i). \tag{2.3.16}$$

The spectroscopic electric quadrupole moment, introduced in equation 2.3.10, is then defined as the expectation value of quadrupole moment defined in equation 2.3.16.

$$Q = \langle I, M = I | Q_z | I, M = I \rangle$$
$$= \left(\frac{16\pi}{5} \frac{I(2I-1)}{(2I+1)(2I+3)(I+1)}\right)^{\frac{1}{2}} \langle I | \left| \sum_{i=1}^{A} r_i^2 Y_2^0(\theta_i, \phi_i) \right| | I \rangle. \tag{2.3.17}$$

In equation 2.3.17 the Wigner-Eckart Theorem was used to proceed from the first to the second line. From this expression it becomes clear that for a nucleus with spin I $<$ 1, the spectroscopic quadrupole moment is zero [43].

2.3.2   Nuclear mean-squared charge radius and the isotope shift

In atomic physics the nucleus is generally viewed as a point charge with electrons orbiting this central point. The nucleus, however, is a collection of nucleons and therefore it has a specific shape and mass. The influence of the shape and mass of the nucleus on the atomic energy levels is quite small and therefore it is only observed via high resolution atomic spectroscopy.

The mass and shape of the nucleus contribute to the isotope shift observed between isotopes of the same element. A more in depth description of the isotope shift will be given in the next section. The mass of the nucleus contributes to what is called the "mass shift". In general the mass shift is not used to determine nuclear properties [43]. The second contribution to the isotope shift is the so-called "volume" or "field" shift. As the name suggests, this effect stems from the volume and charge distribution of the nucleus. The volume and charge distribution change from isotope to isotope for a specific element.

The volume shift component of the isotope shift can be attributed to the second radial moment of the nuclear charge distribution [45]. This is called the nuclear mean square charge radius and is expressed as

$$
\begin{aligned}
\langle r^2 \rangle &= \frac{\int_0^R \rho(\vec{r})\vec{r}^2 d\vec{r}}{\int_0^R \rho(\vec{r})d\vec{r}}, \\
&= \frac{1}{Ze} \int_0^R \rho(\vec{r})\vec{r}^2 d\vec{r},
\end{aligned}
\tag{2.3.18}
$$

where $\rho(\vec{r})$ is the charge density, $\vec{r}$ the radial coordinate, and the denominator is just equal to the charge of the nucleus, Ze. It is important to note that laser spectroscopy can not determine the exact value of $\langle r^2 \rangle$, but it can be used to determine the change in the mean square charge radius from one isotope to the next. When considering two isotopes, A and A', the change in mean square charge radius between the two can be expressed as $\delta \langle r^2 \rangle^{AA'}$. By measuring the isotope shift of an element, information on the change of $\langle r^2 \rangle$ as a function of the neutron number can be found. From this it is then possible to observe interesting features in the structure of the nucleus such as shell closures, nucleon pairing, and nucleus deformation.

2.3.3   Extraction of nuclear properties via laser spectroscopy

The observable nuclear properties described in section 2.3.1 are accessible via laser spectroscopy. Spectra obtained using high-resolution laser spectroscopic techniques can provide information on the magnetic dipole and electric quadrupole moments, and changes in mean-square charge radii of the atom of interest. This information can be gathered from the observed isotope shift and frequency intervals between the hyperfine structure peaks in the spectra. The advantage of using laser spectroscopy techniques to measure the nuclear moments as well as mean-square charge radius, is that the measurements are performed in a nuclear model-independent fashion [46]. Furthermore, laser spectroscopy can also be used to measure the nuclear spin of the ground state nucleus.

As some of the desired nuclear properties are contained in the isotope shift, a discussion on isotope shifts will be given below. This will be followed by a short discussion on how the observable nuclear properties described in section 2.3.1 can be extracted from laser spectroscopy results.

Isotope shifts

As mentioned in the discussion of the nuclear mean-squared charge radius (see section 2.3.2), mainly two effects contribute to the shift in energies of the fine structure levels between different isotopes or the so-called isotope shift. The first contribution is the mass shift, which occurs due to the difference in nuclear mass between different isotopes. The second contribution is the volume or field shift. This contribution is due to the change in the nuclear volume and charge distribution as the amount of neutrons changes. The isotope shift, in frequency, between isotope A and A' can be defined as the sum of the mass and volume shifts [47],

$$\delta\nu_{IS}^{AA'} = \delta\nu_{MS}^{AA'} + \delta\nu_{FS}^{AA'}, \tag{2.3.19}$$

where ν_{MS} represents the mass shift and ν_{FS} the field shift.

As the number of neutrons in the nucleus changes from isotope to isotope, the mass of the nucleus changes as well. Therefore the force experienced by electrons orbiting the nucleus will change, and this leads to a change in the fine structure levels of the atom. The energy of two fine structure levels is then shifted by an amount [43]

$$\delta\nu_{MS}^{AA'} = M\frac{m_{A'} - m_A}{m_A m_{A'}}, \tag{2.3.20}$$

where M is an atomic mass factor that is transition dependent [43], $m_{A'}$ the mass of isotope A', and m_A the mass of isotope A. The mass shift can be

calculated using equation 2.3.20.

The field shift has to be measured spectroscopically. The electrostatic potential acting on the orbiting electrons changes as the nuclear volume and charge distribution changes. Relativistic calculations have shown that the field shift depends on the change in mean-squared charge radius [48], $\delta\langle r^2\rangle$. The field shift can be expressed as

$$\delta\nu_{FS}^{AA'} = \frac{\pi a_0^3}{Z}\Delta|\psi(0)|^2 f(Z)\delta\langle r^2\rangle^{AA'}, \tag{2.3.21}$$

with a_0 being the Bohr radius, $\Delta|\psi(0)|^2$ the change in the electron probability density at the nucleus, and $f(Z)$ a correction factor [49]. The expression of the field shift can be simplified to

$$\delta\nu_{FS}^{AA'} = F\delta\langle r^2\rangle^{AA'}, \tag{2.3.22}$$

where F is the atomic field shift factor, not to be confused with the total angular momentum defined in section 2.3.1. The isotope shift can then be expressed as

$$\delta\nu_{IS}^{AA'} = M\frac{m_{A'} - m_A}{m_A m_{A'}} + F\delta\langle r^2\rangle^{AA'}. \tag{2.3.23}$$

From this equation it becomes clear that the isotope shift can be split into an electronic and a nuclear part. In equation 2.3.23 the atomic factors, M and F, contain all the optical transition information and $\frac{m_{A'}-m_A}{m_A m_{A'}}$ and $\delta\langle r^2\rangle^{AA'}$ contain the nuclear information.

It is important to note that for lighter atoms the mass shift tends to dominate, while generally $s \to p$-type transitions have larger field shifts [46]. The atomic M and F factors have to be calculated theoretically or semi-empirically [43].

Nuclear spin

A couple of ways exist to determine the nuclear spin using spectra obtained through laser spectroscopy. The first method that can be used does not rely on any assumptions regarding the nuclear structure. By analyzing the ratio of the heights of hyperfine structure peaks in spectra obtained via laser spectroscopy the nuclear spin, I, can be determined. Kreim *et al.* recently demonstrated this technique for potassium isotopes around the $N = 28$ shell closure [50]. It was reported that the difference between the relative intensities between different isotopes is significant, and therefore these isotopes could not have the same nuclear spin [50].

In section 2.3.1, it was stated that the number of hyperfine states for a specific fine structure level is determined by the nuclear spin, I, and the electronic

angular momentum, J. The possible values for the total angular momentum, F, range between $|I + J|$ and $|I - J|$. In the case where $I > J$ there exists $2J + 1$ possible F-values. In the case where $I < J$ there exists $2I + 1$ possible F-values. Therefore when $I < J$ the number of hyperfine peaks observed can be used to determine the nuclear spin [43].

In section 2.3.1 the magnetic dipole moment was defined (see equation 2.3.12). If the magnetic moment has been measured and the nuclear spin g-factor is known, the ratio of these two observables will equal the nuclear spin. The g-factors can be determined experimentally using laser spectroscopy, β-NMR, etc [43].

Under the assumption that the ratio of hyperfine A-parameter stays constant for the atomic ground state and an excited state, the nuclear spin can also be determined. In section 2.3.1 the hyperfine A-parameter was defined as $\frac{\mu_I B_E}{IJ}$. If we denote the A-parameter for the excited state as A_{es} and for the ground state as A_{gs} the ratio between the two will be expressed as

$$\begin{aligned}
\frac{A_{gs}}{A_{es}} &= \frac{\mu B_{E,gs}}{IJ_{gs}} \bigg/ \frac{\mu B_{E,es}}{IJ_{es}}, \\
&= \frac{B_{E,gs}J_{es}}{B_{E,es}J_{gs}}.
\end{aligned} \tag{2.3.24}$$

Using a variety of spin assumptions during analysis of measured hyperfine structure, the correct ratio of the A-parameters can be used to deduce the correct spin [46].

Nuclear moments

The nuclear moments of interest were described in section 2.3.1. The first moment is the magnetic dipole moment of the nucleus, μ_I (see equation 2.3.14), and the second is the electric quadrupole moment, Q (see equation 2.3.17). As highlighted in section 2.3.1, both the moments influence the hyperfine splitting of the atomic energy levels and are contained with the A and B hyperfine parameters. As a reminder these parameters are defined as

$$\begin{aligned}
A &= \frac{\mu_I B_E}{IJ}, \\
B &= eQV_{zz}.
\end{aligned}$$

From the definition of the A-parameter, it becomes clear that the value of B_E needs to be measured first before the magnetic moment can be determined. If μ and B_E have been determined for a specific isotope, that isotope can be used as a reference to determine μ for an unknown isotope [46]. The magnetic

moment of the unknown isotope can then be expressed as

$$\mu_{unknown} = \frac{I_{unknown}}{I_{ref}} \frac{A_{unknown}}{A_{ref}} \mu_{ref}, \qquad (2.3.25)$$

where $\mu_{unknown}$ is expressed in terms of the reference isotope.

Similarly for the spectroscopic quadrupole moment the gradient of the electric field at the nucleus, V_{zz} needs to be calculated or measured first. Once this quantity is known it is possible to determine the spectroscopic quadrupole moment using the ratios between the measured B hyperfine parameters. An isotope with a known spectroscopic quadrupole moment is used as a reference to calculate the quadrupole moments of other isotopes using

$$Q_{unknown} = Q_{ref} \frac{B_{ref}}{B_{unknown}}, \qquad (2.3.26)$$

where $Q_{unknown}$ is the unknown quadrupole moment, Q_{ref} is the quadrupole moment for the reference isotope, and B_{ref} and $B_{unknown}$ the hyperfine B-parameter for the reference isotope and the isotope of interest, respectively.

Changes in nuclear charge radii

The final nuclear observable up for discussion is the nuclear mean-squared charge radius. The mean-squared charge radius can be extracted from the isotope shift. In the previous section the isotope shift was defined in equation 2.3.23.

The mean-squared charge radius can be extracted from the measured isotope shift, $\delta\nu_{IS}^{AA'}$, if the mass shift, (M), and field shift, (F), parameters are known for at least one transition [46]. The equation above can then be solved for $\delta\langle r^2 \rangle^{AA'}$.

If the mass shift and field shift parameters are known for a transition, the King plot method [47] can be used to determine the unknown parameters for other transitions. The King plot can be used to determine the changes in nuclear mean-squared charge radius from the isotope shift for various transitions. When considering two transitions, labelled 1 and 2, the King Plot method assumes that the changes in nuclear mean-squared charge radius stay constant for both transitions [46]. Equation 2.3.23 can be written in terms of the changes in mean-squared charge radius

$$\delta\langle r^2 \rangle^{AA'} = \frac{1}{F} \left(\delta\nu_{IS}^{AA'} - M \frac{m_{A'} - m_A}{m_A m_{A'}} \right). \qquad (2.3.27)$$

Then it follows for transitions 1 and 2 that

$$\frac{1}{F_1} \left(\delta\nu_1^{AA'} - M_1 \frac{m_{A'} - m_A}{m_A m_{A'}} \right) = \frac{1}{F_2} \left(\delta\nu_2^{AA'} - M_2 \frac{m_{A'} - m_A}{m_A m_{A'}} \right). \qquad (2.3.28)$$

A reduced mass, $\mu_{AA'}$, can be introduced where $\mu_{AA'} = \frac{m_A m_{A'}}{m_{A'} - m_A}$. The expression above then becomes

$$\frac{1}{F_1} \left(\mu_{AA'} \delta \nu_1^{AA'} - M_1 \right) = \frac{1}{F_2} \left(\mu_{AA'} \delta \nu_2^{AA'} - M_2 \right) \qquad (2.3.29)$$

This equation can be rearranged in terms of the isotope shift of the first transition,

$$\mu_{AA'} \delta \nu_1^{AA'} = \frac{F_2}{F_1} \mu_{AA'} \delta \nu_2^{AA'} - \frac{F_2}{F_1} M_2 + M_1. \qquad (2.3.30)$$

Equation 2.3.30 is essentially a straight line with a slope of $\frac{F_2}{F_1}$ and an intercept of $-\frac{F_2}{F_1} M_2 + M_1$. This can then be used to determine unknown field and mass shift parameters, which in turn make it possible to use equation 2.3.23 to determine $\delta \langle r^2 \rangle^{AA'}$.

2.4 Resonance ionization spectroscopy

In the previous section it was made clear that lasers can be used to obtain information regarding the atom as well as the atomic nucleus. In this section some of the principles surrounding laser spectroscopy and specifically resonance ionization spectroscopy are discussed.

2.4.1 Optical Transitions and selection rules

Atoms have discrete energy levels. The factors that determine these levels have been discussed in section 2.2. When photons interact with the atom, the electrons surrounding the atom can absorb the incident light and be excited into a higher energy level. This excitation however can only happen if the photon has the right amount of energy to reach the excited state. The photon energy, $h\nu$, has to be equal to the difference in energy between the two states,

$$h\nu = E_2 - E_1 \qquad (2.4.1)$$

where ν is the frequency of the photon and E_1 and E_2 the energy of the lower and upper energy states respectively. The energy difference should account for the fine structure, hyperfine structure, as well as the isotope shift. The required photon energy can then be expressed as

$$\begin{aligned} h\nu &= h\nu_0 + \Delta E_{FS} + \Delta E_{HFS}, \\ &= h\nu_0 + (E_{FS_2} - E_{FS_1}) + (E_{HFS_2} - E_{HFS1}), \end{aligned} \qquad (2.4.2)$$

where $h\nu_0$ corresponds to the photon energy of the transition between configurations described by n and l quantum numbers. E_{FS} and E_{HFS} are given by

Table 2.3: Selection Rules for atomic transitions.

Type	Rule	Exceptions
Rigorous Rules	$\Delta J = 0, \pm 1$	$0 \to 0$ forbidden
	$\Delta M = 0, \pm 1$	$0 \to 0$ forbidden when $\Delta J = 0$
LS-Coupling	$\Delta S = 0$	N/A
	$\Delta L = 0, \pm 1$	$0 \to 0$ forbidden

equation 2.2.24 and equation 2.3.11, respectively.

Other than the energy requirement associated with a transition, there are also selection rules which govern which transitions are allowed. These selection rules stem from the quantum mechanical interaction between the incident photons and the atom. The selection rules for transitions has been summed up in Table 2.3 [39].

In Table 2.3 the selection rules for atomic transitions have been split into two sections, namely the rigorous selection rules and the selection rules in the LS-coupling scheme. The rigorous selections are always followed, regardless of the system. The change in electronic angular momentum, J, is only allowed to be $+1, -1$, or 0 with the transition between a $J = 0$ level and another $J = 0$ level being forbidden. For the M_J values the allowed transitions follow a change of $+1, -1$, or 0, where the transition between a $M_J = 0$ level and another $M_J = 0$ level is forbidden when $\Delta J = 0$. For a purely LS-coupled system no change in the spin is allowed during transitions. This means only singlet-singlet or triplet-triplet transitions are allowed. The change in orbital angular momentum, L, is allowed to be $+1, -1$, or 0 with the exception that $L = 0$ to $L = 0$ is forbidden. Purely LS-coupled systems are rare, therefore the last two rules are not always followed and serve more as guidelines than strenuous rules.

With the basic ideas highlighted for the interaction between light and atoms, the attention now shifts towards one of the most useful spectroscopic techniques, namely resonance ionization spectroscopy.

2.4.2 Resonance ionization spectroscopy schemes

Resonance ionization spectroscopy (RIS) is a resonant multi-photon excitation process for the selective ionization of an atom [51; 52]. The process involves a series of atomic excitations, with at least one resonant transition, and ends when the atom is ionized. The RIS technique came into existence during the 1970s. A two-step resonance ionization scheme for rubidium was proposed by Letokhov in 1969 [53]. The first experiments using the two-step resonance ionization technique was performed on Rubidium in 1971 [54]. After the break-

through using the two-step resonant ionization process, multiphoton excitation and ionization processes were suggested as a method to ionize various atoms and molecules using RIS. Since then the technology of surrounding lasers has developed to such an extent that nearly all the elements on the periodic table are accessible via RIS [51].

The RIS method has quite a few advantages. These can be summed up as [55]:

- RIS is very sensitive. Therefore the technique can be applied to rare or exotic elements across the nuclear chart. The reason RIS is so efficient is that it relies on the detection of ions or electrons, which can be collected and detected more efficiently than photons.

- Since the atomic structure changes for different elements, the photon energy needed to excite the atom resonantly will be different for the different elements. Therefore RIS excitation schemes can be element and even isotope specific. Furthermore the element selective nature of RIS limits isobaric contamination observed in conventional mass spectrometry.

- The ion detection methods used for RIS limits the background in measurements.

All the different resonance ionization schemes used during RIS can be classified by their characteristic features [52]. These features include

- the number of excitation stages,

- the number of absorbed photons,

- the different number of frequencies (wavelengths) used for excitation.

The different resonance ionization schemes have been illustrated in Figure 2.6.

As illustrated in Figures 2.6, ionization can take place via three mechanisms. The atom can be resonantly excited by one photon (illustrated in blue) or it can be resonantly excited via two photon absorbtion (illustrated in red). It is also possible to have more than one resonant excitation, this is illustrated by the yellow and green path in Figure 2.6. Once the atom has been excited it can be ionized. The excited atom can be non-resonantly ionized, which is illustrated by the pink path in Figure 2.6. It is also possible to resonantly excite the atom into an auto-ionizing state (illustrated by the light blue). Autoionization states are bound atomic states that lie above the ionization limit of the atom [52]. Above the ionization limit of the atom there also exists the ionization continuum. Atoms excited to an auto-ionizing level are likely to transfer to the continuum and be ionized [52]. Lastly, the atom can be resonantly excited into a highly excited Rydberg state. These states are close to
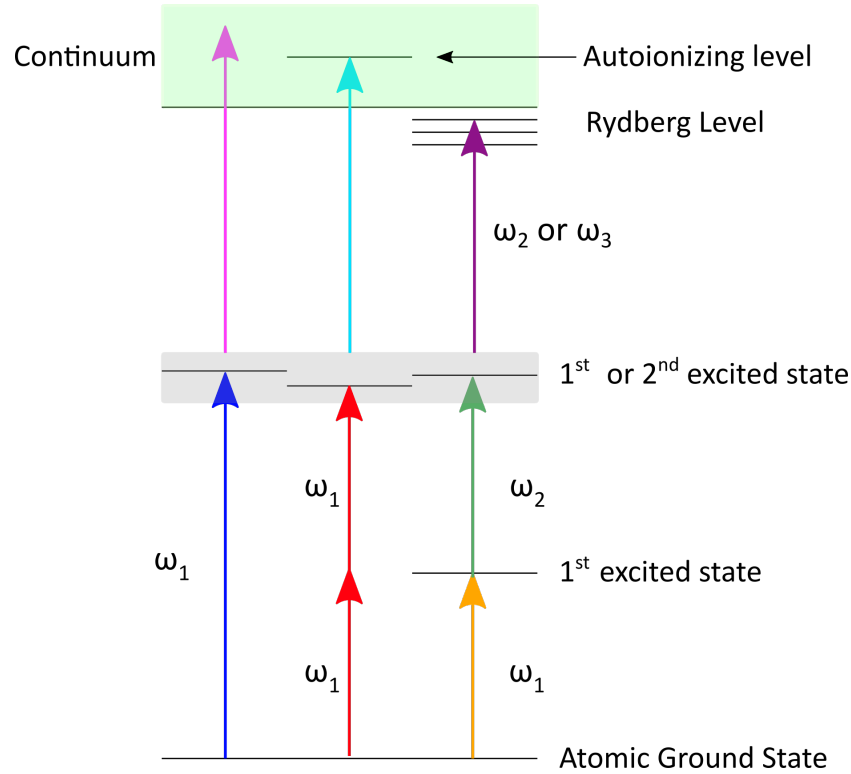
Figure 2.6: Schematic representation the different RIS schemes.

the ionization limit of the atom and can be ionized via pulsed electric fields, IR radiation pulses, or collisions with other particles [52]. Ionization via highly excited Rydberg states and auto-ionizing states is more efficient when compared to non-resonant ionization and therefore these two methods are more desired when looking at various ionization schemes [52]. It is however important to note that the Rydberg levels as well as auto-ionizing levels of various elements are not well known.

The selection of appropriate ionization schemes is determined by the energy levels and the ionization potential of the element of interest, as well as the accessible laser wavelengths. For various atoms a two-step ionization scheme is not useful, since the ionization limit of the atom is too high. The wavelengths needed to excite and ionize some elements are not readily available for two-step schemes. For these elements it is desirable to use three-step ionization schemes. The laser wavelengths used in three-step ionization schemes usually fall within the ultraviolet-visible region $(200 - 700\text{nm})$ and laser light in the these regions are easily produced.

For some elements, however, the first resonant transition lies within the vacuum ultra-violet (VUV) region $(< 200\text{nm})$. For these elements, the atom can be excited using two- or three-photon resonance processes [52].

To effectively ionize all the atoms irradiated with laser light, the so-called flux condition has to be satisfied. The flux condition states that the flux of incident photons, $F(cm^{-2}s^{-1})$, ionizing the atom has to be greater than the depopulation rate, β, of the excited state [46]. Depopulation occurs when the atom relaxes to a dark state that is not affected by the incident laser light. The flux condition can be written as [46]

$$\sigma_i F \gg \beta, \tag{2.4.3}$$

where σ_i is the ionization cross section for the excited state.

2.4.3 Resonance Ionization Schemes for tin

Resonance excitation schemes for tin have been identified from literature [56; 57]. These schemes have been chosen since the excitation wavelength is readily accessible at Stellenbosch University. All three the ionization schemes listed in Table 2.4 start with the tin atom in its ground state, $[Kr]\,4d^{10}5s^25p^2\,{}^3P_0$.

Table 2.4: Resonance ionization schemes for tin

Scheme	1st Excitation wavelength nm	1st Resonant Level	2nd Excitation wavelength (nm)	2nd Resonant Level	Ionization mechanism
1	286.3	$5p6s\,{}^3P_1$	617.2	$5p7p\,{}^3P_1$	Non-resonant ionization using a second 617.2 nm photon
2	286.3	$5p6s\,{}^3P_1$	615	$5p7p\,{}^3D_2$	Non-resonant ionization using a second 615 nm photon
3	224.68	$5p5d\,{}^3D_1$	628.1	$5p6f\,{}^2P_{\frac{1}{2}}$	Autoionization via $5p6f\,{}^2P_{\frac{1}{2}}$ level

Ionization scheme 1 and 2 consist of two resonant excitations, followed by a non resonant ionization step using a photon with the same frequency as the second excitation step. The third ionization scheme consists of two resonant excitations only. The second excitation for this scheme is to the $5p6f\,{}^2P_{\frac{1}{2}}$ level. This level is an auto-ionizing level, which will ionize by transferring to the continuum. This last scheme will be due to the 224.68 nm excitation wavelength being near the vacuum ultraviolet region, meaning the light is highly absorbing in any medium.

It is important to consider the isotope shift of the resonant level when considering appropriate RIS schemes. For the 286.3 nm line of Sn the isotope shifts are listed in Table 2.5 [29].

Table 2.5: The isotope shifts of the 286.3 nm line of Sn relative to ^{120}Sn

Isotope	Isotope Shift $(10^{-3}\ cm^{-1})$
112	-40.638
113	-36.00
114	-30.043
115	-26.849
116	-19.215
117	-15.725
118	-9.014
119	-5.990
120	0
121	3.03
122	7.850
123	9.91
124	14.715
125	16.8

2.4.4   Second harmonic generation

In order to produce the wavelengths needed for RIS of Sn it is necessary to frequency double the dye laser beam. Frequency doubling is performed by second harmonic generation in a suitable crystal such as Beta-Barium Borate (BBO).

In the undepleted pump approximation, and assuming slow varying field amplitudes it can be shown that the intensities of the second harmonic light, I_2, and the fundamental light, I_1, are related by [58]

$$I_2 \propto I_1^2 L^2 \left[\frac{\sin\left(\frac{\Delta kL}{2}\right)}{\frac{\Delta kL}{2}} \right]^2 = I_1^2 L^2 sinc^2 \left(\frac{\Delta kL}{2} \right), \qquad (2.4.4)$$

where Δk is the wave vector mismatch:

$$\Delta k = 2k_1 - k_2 = 2\frac{n_1 \omega_1}{c} - \frac{n_2 \omega_2}{c}. \qquad (2.4.5)$$

The factor $sinc^2 \left(\frac{\Delta kL}{2} \right)$ is the phase matching factor that shows efficient second harmonic generation is only possible when Δk is close to zero. From equation 2.4.5, $\Delta k = 0$ requires $n_1 = n_2$.

In a negative birefringent crystal such as BBO the ordinary index of refraction, n^o, is larger than the angle-dependent extraordinary index of refraction, $n^e(\theta)$,

for any frequency. The relation is [59]

$$\left(\frac{1}{n^e(\theta)}\right)^2 = \left(\frac{\sin\theta}{n^e(\theta=90°)}\right)^2 + \left(\frac{\cos\theta}{n^o}\right)^2. \tag{2.4.6}$$

Therefore angle tuning can be used to achieve phase matching.

For type I phase matching, the crystal is orientated in such a way that the fundamental light at ω_1 is polarized along the ordinary direction (seeing the index of refraction n_1^o). Second harmonic that is polarized perpendicular to the fundamental polarization (seeing the index of refraction $n_2^e(\theta)$) will be generated when the angle θ is optimized to achieve $n_1^o = n_2^e(\theta)$.

The extraordinary refractive index $n_2^e(\theta)$ can be calculated using equation 2.4.6, resulting in

$$n_2^e(\theta) = \left[\left(\frac{\sin\theta}{n^e(\theta=90°)}\right)^2 + \left(\frac{\cos\theta}{n^o}\right)^2\right]^{\frac{-1}{2}}. \tag{2.4.7}$$

2.5   Time-of-flight mass spectrometry

This study investigated the use of a time-of-flight mass spectrometer (ToF-MS) to identify ionized species provided by an atomic beam source. The ToF-MS works on the principle that ions with different mass to charge (m/q) ratios will undergo different accelerations by electric fields from Newton's Second law,

$$\vec{a} = \frac{\vec{F}}{m} = \frac{q}{m}\vec{E}. \tag{2.5.1}$$

Therefore the ions will have different final velocities after acceleration and will take different times to travel through the ToF-MS. This type of mass spectrometer has been utilised since the 1950s, with one of the first major breakthroughs coming from Wiley and McLaren in 1955 [60]. Wiley and McLaren introduced the idea of spatial focus within the ToF-MS and delayed extraction of ions [60]. This greatly improved the resolution of the instrument. The spatial focus of the instrument compensates for the initial spatial distribution of the ions generated within the ToF-MS, while the delayed extraction compensates for a velocity spread in the ions [60]. The next major breakthrough came with the introduction of the mass reflectron. Mamyrin extended the existing ToF-MS by introducing an ion reflector [61]. The reflectron improves the mass resolution of the instrument by narrowing the velocity distribution of the ions.

The ToF-MS has a number of advantages over more traditional mass spectrometers. The advantages offered by ToF-MS include the following [62]

- high mass resolution,

- theoretically unlimited mass range,

- easy to design and construct.

In the following sections the basic ToF-MS will be discussed, followed by the introduction of the two stage ion source, and lastly the reflectron based ToF-MS.

2.5.1   Basic Time-of-flight mass spectrometers

The most basic version of a ToF-MS consists of an ionization region, a field free region, followed by an ion detector (see Figure 2.7 below). Ions are usually produced through laser ionization and are then accelerated by an homogeneous electric field. The ions exit the ionization region and enter the field free drift region. In this region the ions with different masses will start separating spatially, due to travelling at different velocities. The ions will then reach the ion detector, with the lighter ions reaching the detector first.
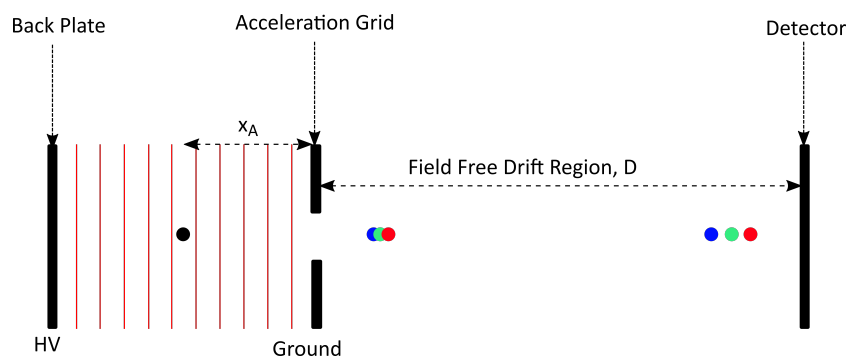
Figure 2.7: A basic Time-of-flight mass spectrometer. Electric equipotential lines are indicated in the acceleration region. Ions of different mass (for the same charge) are indicated by different colour dots.

In Figure 2.7 the ionization region consists of a back plate with an applied high voltage (HV) and a grounded acceleration plate or grid. Ions are generated within the black dot in the middle of the ionization region. The ions are then accelerated by the present electric field over the distance x_A. The red lines in the ionization region represent the equipotential lines. As the ions move through the field free drift region, separation occurs. The heavier ions will have a lower velocity when compared to the lighter ions. This is illustrated by the three coloured dots separating as they move closer to the end of the field free region.

The ions are accelerated due to the force generated by the electric field acting on them,

$$\left|\vec{F}\right| = q\left|\vec{E}\right| = m\left|\vec{a}\right|.$$

The acceleration can then be written as:

$$a = \frac{qE_A}{m}, \tag{2.5.2}$$

where q is the charge of the ion, E_A the electric field, and m the mass of the ion. Since the electric field is homogeneous, the acceleration is constant. Since the acceleration is constant, it is possible to derive the equations of motion. Assuming that $v = v(t = 0\,s) = 0\,\text{m/s}$ and $x_0 = x(t = 0\,s) = 0\,\text{m}$ it follows that

$$v = \int_0^{t_A} adt = at_A, \tag{2.5.3}$$

$$x_A = \int_0^{t_A} vdt = \frac{1}{2}at_A^2. \tag{2.5.4}$$

Combining equations 2.5.2 and 2.5.4, the time it takes for the ion to be accelerated, t_a, can be determined,

$$t_A = \sqrt{\frac{2x_A m}{qE_A}}. \tag{2.5.5}$$

The equation above can be rewritten in term of the potential applied to the backplate, $2U$.

$$t_A = \sqrt{\frac{2x_A m}{qE_A}} = 2x_A\sqrt{\frac{m}{2qU}}. \tag{2.5.6}$$

Since the ions are not accelerated any further once they reach the field free drift region, the flight time of the ions in this region can be determined using the kinetic energy of the ion. The kinetic energy of the ion at the end of the acceleration region is given by:

$$E_{Kin} = \frac{1}{2}mv^2 = qx_A E_A = qU. \tag{2.5.7}$$

The velocity of the ion is then determined by

$$v = \sqrt{\frac{2qx_A E_A}{m}} = \sqrt{\frac{2qU}{m}}. \tag{2.5.8}$$

The flight time through the field free drift tube can then be calculated using

$$t_D = \frac{D}{v} = D\sqrt{\frac{m}{2qU}} = \frac{D}{\sqrt{2x_A}}\sqrt{\frac{m}{qE_A}}. \tag{2.5.9}$$

The total flight time for a linear ToF-MS is then given as

$$
\begin{aligned}
t_{tot} = t_a + t_D &= 2x_A\sqrt{\frac{m}{2qU}} + D\sqrt{\frac{m}{2qU}} \\
&= 2\sqrt{x_A}\sqrt{\frac{m}{2q}}\sqrt{\frac{1}{E_A}} + \frac{D}{\sqrt{x_A}}\sqrt{\frac{m}{2q}}\sqrt{\frac{1}{E_A}} \\
&= 2\sqrt{x_A}C + \frac{D}{\sqrt{x_A}}C,
\end{aligned}
\tag{2.5.10}
$$

where $C = \sqrt{\frac{m}{2q}}\sqrt{\frac{1}{E_A}}$. The expressions listed above, assume that all the ions are generated at the same time and position, while also having no velocity in the acceleration direction. In reality the ions will be generated in a certain volume, over a certain time, and they will exhibit a transverse and longitudinal or parallel velocity distribution.

Since the ions are generated in a certain volume in space, some of the ions will be generated closer to the backplate of the ion source. These ions will be accelerated more, since they stay within the electric field longer. The ions generated closer to the back plate of the ion source will then enter the field free drift region with a higher velocity. This initial spatial distribution of the ions therefore contribute to a velocity distribution of the ions. There are a couple of ways to counteract the initial spatial distribution of ions. When using laser light to ionize a sample, a tight focus can reduce the volume where ionization takes place. This reduces the spread in the positions of the ions. The velocity distribution of the ions as they exit the acceleration region is therefore narrower. The second way to counteract the initial spatial distribution is to place the ion detector at the spatial focus of the ToF-MS [60]. The spatial focus will be discussed in detail in Section 2.5.2.

In reality not all ions are generated at the same time and this leads to a temporal distribution of the initial ions. The ions generated first will be accelerated by the static electric field first. To counteract this, the accelerating electric field can be pulsed. This ensures that the electric field starts acting on the ions at the same time. Short laser pulses (< 1 ns [62]) can also be used to reduce the temporal distribution. Short pulses ensure that the ions are generated at more or less the same time.

The ions can also have initial velocity distributions parallel and transverse to the accelerating electric field. Of the two distributions, the parallel velocity distribution has the biggest influence on the flight time of the ions. Ions with velocities along the acceleration access will cause a spread in the arrival time of the ions at the detector. To counteract this neutral atoms can be introduced into the ToF-MS orthogonal to the acceleration axis using an effusive atomic

beam or a supersonic gas jet. These atom sources, as will be described in Section 2.6, have the property of a small velocity distribution perpendicular to the atom beam. This results in a small velocity distribution parallel to the acceleration axis.

2.5.2   The Wiley-McLaren two stage ion source

In the previous section, it was mentioned that placing a detector at the spatial focus of the ToF-MS will counteract an initial spatial distribution of ions. The spatial focus can be described as a point in space where the higher energetic ions overtake lower energetic ions of the same species [62]. The ions generated closer to the back plate of the ionization region have a longer distance to travel, but gain a higher kinetic energy. Ions generated closer to the extraction grid have a shorter distance, but lower kinetic energy. Since the higher energetic ions travel faster than the ions generated closer to the acceleration grid, they will eventually catch up to these lower energetic ions. Placing the detector at this spot is ideal, since the ions of the same mass are all bunched together at this point. Therefore the spatial focus is crucial to increase the resolution of the ToF-MS [60].

The spatial focus of basic ToF-MS (see Figure 2.7) can be determined using

$$\frac{dt_{tot}}{dx_A} = 0. \tag{2.5.11}$$

Using the expression above with equation 2.5.10,

$$\frac{dt_{tot}}{dx_A} = 2\left(\frac{1}{2\sqrt{x_A}}\right)C + \left(\frac{-1}{2x_A^{3/2}}\right)DC = 0. \tag{2.5.12}$$

Solving in terms of D yields

$$D = 2x_A = x_{SF}. \tag{2.5.13}$$

The time it takes to reach the spatial focus is given by

$$t_{SF} = x_{SF}\sqrt{\frac{m}{2qU}}. \tag{2.5.14}$$

Therefore the spatial focus is found at the point $2x_A$ into the field free region (see Figure 2.8). This point is independent of the potentials applied to create the acceleration region. The problem, however, is that the distance $2x_A$ is quite short, therefore ions with different masses do not have enough time to separate. This problem can be solved by using a two stage ionization region [60].
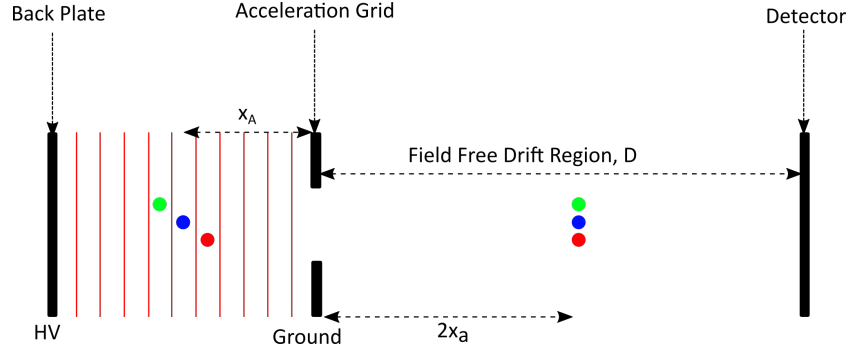
Figure 2.8: Spatial focus in a basic Time-of-flight mass spectrometer.

The two stage ionization region differs from the one illustrated in Figure 2.7 by including a second acceleration grid. The two stage ionization region is illustrated in Figure 2.9. The flight time for ions travelling through the first acceleration region is the same as for the simple ToF-MS described earlier and can be expressed as

$$t_{A1} = 2x_{A1}\sqrt{\frac{m}{2qU_{A1}}} = 2\sqrt{x_{A1}}\sqrt{\frac{m}{2q}}\sqrt{\frac{1}{E_{A1}}}. \qquad (2.5.15)$$
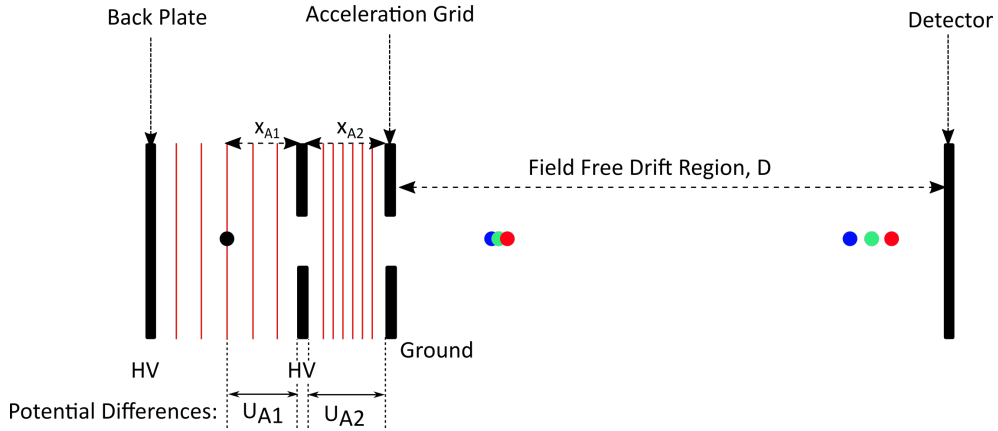
Figure 2.9: Two stage ion source ToF-MS. Potential on the electrodes are $2U$ on the back plate, $U - U_{A1}$ on the first acceleration grid and 0 V on the second acceleration grid. Potential differences traversed by the ions are U_{A1} and $U_{A2} = U - U_{A1}$.

For the second acceleration region the ions enter with a kinetic energy qU_{A1}. The time ions take to travel through the second acceleration region is then given by

$$t_{A2} = \frac{2x_{A2}}{U_{A2}}\left(\sqrt{U} - \sqrt{U_{A1}}\right)\sqrt{\frac{m}{2q}}. \qquad (2.5.16)$$

The total flight time of the ions is then given as:

$$t_{tot} = t_{A1} + t_{A2} + t_{SF}. \tag{2.5.17}$$

The intermediate acceleration grid introduces a second potential. This free parameter can be freely adjusted and implies that the spatial focus can be adjusted as well. For a two stage ion source the first order spatial focus can be positioned as far as $x_{SF} = 100$ cm [62] for the condition $\frac{dt_{tot}}{dx_{A1}} = 0$. The problem, however, is that for long flight paths the compression ability of the first order spatial focus deteriorates [62].

The second order spatial focus can be used to solve this problem. A second condition can be introduced, namely $\frac{d^2 t_{tot}}{dx_{A1}^2} = 0$. The second potential can be adjusted to satisfy this condition, leading to the formation of a second order spatial focus. For a two stage ion source the first and second order spatial focuses can be determined as [62]

$$\frac{dt_{tot}}{dx_{A1}} = \left(\frac{x_{A1}}{U_{A1}} - \frac{x_{A2}}{U_{A2}}\right) U_{A1}^{-\frac{1}{2}} + \left(\frac{x_{A2}}{U_{A2}} - \frac{x_{SF}}{2U}\right) U^{-\frac{1}{2}} = 0, \tag{2.5.18}$$

$$\frac{d^2 t_{tot}}{dx_{A1}^2} = \left(\frac{x_{A1}}{U_{A1}} - \frac{x_{A2}}{U_{A2}}\right) U_{A1}^{-\frac{3}{2}} + \left(\frac{x_{A2}}{U_{A2}} - \frac{x_{SF}}{2U}\right) U^{-\frac{3}{2}} = 0. \tag{2.5.19}$$

Solving equation 2.5.18 for the first order spatial focus in terms of x_{SF} leads to the following:

$$x_{SF} = 2\left(\frac{U}{U_{A1}}\right)^{\frac{3}{2}} \left(x_{A1} - a_{A2}\frac{U_{A1}}{U_{A2}} \left(1 - \sqrt{\frac{U_{A1}}{U_{A2}}}\right)\right) \tag{2.5.20}$$

This expression can be simplified further by using $U_{A2} = U - U_{A1}$ and introducing the ratio between potentials, $\gamma = \frac{U}{U_{A1}}$, [62]. The expression for x_{SF} then becomes:

$$x_{SF} = 2\gamma^{\frac{3}{2}} \left(x_{A1} - \frac{x_{A2}}{\gamma + \sqrt{\gamma}}\right). \tag{2.5.21}$$

This equation reduces to equation 2.5.13 when $x_{A2} = 0$ and the total potential $U = U_{A1}$.

To achieve a second order spatial focus, both equation 2.5.18 and equation 2.5.19 must be satisfied. To do this equation 2.5.18 is divided by U_{A1} and then set equal to equation 2.5.19 [62]. This leads to the following:

$$\left(\frac{x_{A1}}{U_{A1}} - \frac{x_{A2}}{U_{A2}}\right) U_{A1}^{-\frac{3}{2}} + \left(\frac{x_{A2}}{U_{A2}} - \frac{x_{SF}}{2U}\right) U^{-\frac{1}{2}} U_{A1}^{-1} =$$
$$\left(\frac{x_{A1}}{U_{A1}} - \frac{x_{A2}}{U_{A2}}\right) U_{A1}^{-\frac{3}{2}} + \left(\frac{x_{A2}}{U_{A2}} - \frac{x_{SF}}{2U}\right) U^{-\frac{3}{2}}. \tag{2.5.22}$$

The terms containing $U_{A1}^{-\frac{3}{2}}$ can then be eliminated. The equation is then multiplied with U^2.

$$\left(\frac{x_{A2}}{U_{A2}} - \frac{x_{SF}}{2U}\right) U^{\frac{3}{2}} U_{A1}^{-1} = \left(\frac{x_{A2}}{U_{A2}} - \frac{x_{SF}}{2U}\right) U^{\frac{1}{2}} \tag{2.5.23}$$

The $\gamma = \frac{U}{U_{A1}}$ ratio is used once again as well as the ratio $\frac{U}{U_{A1}} = \frac{\gamma}{\gamma-1}$. The equation above then simplifies to [62]:

$$\gamma = \frac{3x_{SF}}{x_{SF} - 2x_{A2}}. \tag{2.5.24}$$

The second order spatial focus can then be found by solving for x_{SF}.

2.5.3 Reflectron Time-of-flight mass spectrometer

While the introduction of the spatial focus increases the resolution of the ToF-MS, a significant further improvement can be made by introducing a ion reflector or reflectron into the setup. Mamyrin *et al* [61] designed and implemented the first reflectron Tof-MS in 1973. The reflectron ToF-MS is shown schematically in Figure 2.10.
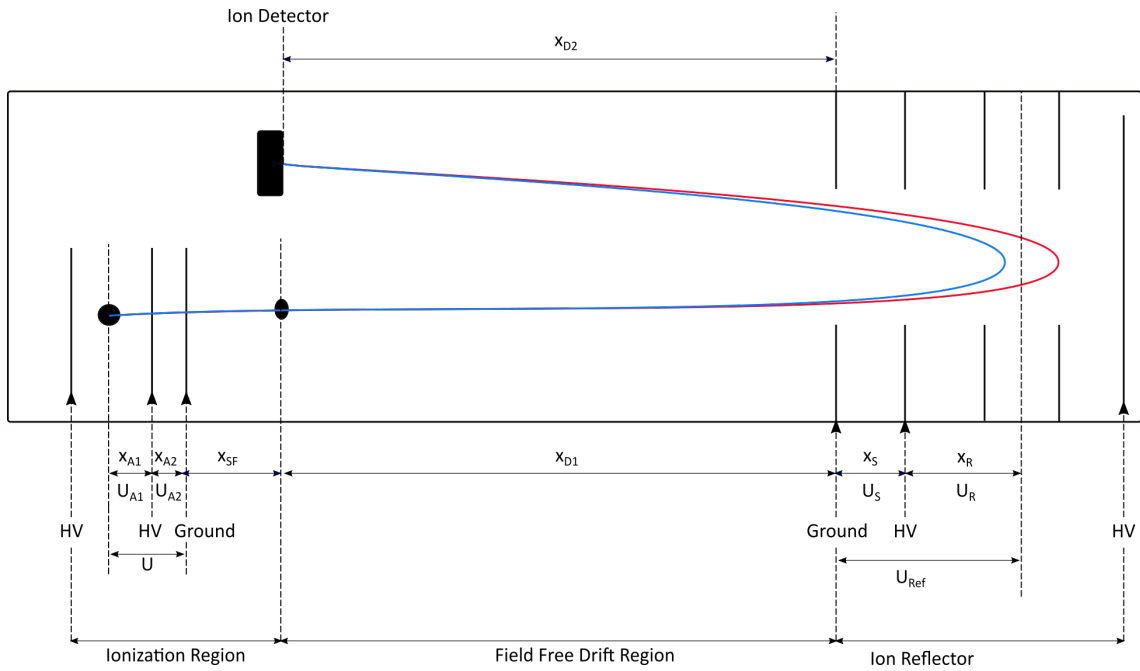
Figure 2.10: The reflectron time-of-flight mass spectrometer.

The reflectron consists of a bunch of grids. Voltages are applied to the back plate of the reflectron and one of the intermediate grids, U_S. The rest of the

grids are connected to the back plate usually through a resistor chain and the potentials are allowed to float to values determined by this chain. The front grid of the reflectron is grounded to keep the field free drift region.

The reflectron compensates for the kinetic energy distribution of the ions as they reach the reflectron. Higher energetic ions will take longer to be slowed down and turned around, meaning they travel deeper into the reflectron. The lower energetic ions, will be turned around earlier in the reflectron. This is illustrated in Figure 2.10 where the red line represents the faster moving ions and the blue line represents the slower moving ions. An appropriately designed reflectron will reduce the spread in the flight times of ions with the same mass, but different kinetic energies because of the different initial positions or velocities in the ionization region. The reflectron produces a spatial focus of the ions at the detector by means of the energy-dependent time delay in the reflectron.

In a similar fashion to the two-stage ion source, the reflectron also has a spatial focus. Ideally the detector will be placed at this spot. The position of the reflectron's spatial focus is determined using the same approach as the two-stage ion source.

From Figure 2.10 the distance the ion travels through the field free drift region is given by $x_D = x_{D1} + x_{D2}$. The potential where the ion turns around, U_{Ref}, is defined as $U_{Ref} = U_R + U_S$. $U_{Ref} = U$ if the initial velocity of the ion in the acceleration direction is zero. The total flight time from the reflectron to the detector is then given by:

$$t_{total} = t_{xR} + t_{xS} + t_{x_{D2}}. \qquad (2.5.25)$$

The second order spatial focus is then determined by the two conditions:

$$\frac{dt_{total}}{dx_R} = 0,$$

$$\frac{d^2 t_{total}}{dx_R^2} = 0.$$

Using the parameters of the reflectron the two equations above reduce to [62]:

$$\frac{dt_{total}}{dx_R} = \left(\frac{x_R}{U_R} - \frac{x_S}{U_S}\right) U_R^{-\frac{1}{2}} + \left(\frac{x_S}{U_S} - \frac{\frac{1}{2}x_D}{2U_{Ref}}\right) U_{Ref}^{-\frac{1}{2}} = 0, \qquad (2.5.26)$$

$$\frac{d^2 t_{total}}{dx_R^2} = \left(\frac{x_R}{U_R} - \frac{x_S}{U_S}\right) U_R^{-\frac{3}{2}} + \left(\frac{x_S}{U_S} - \frac{\frac{1}{2}x_D}{2U_{Ref}}\right) U_{Ref}^{-\frac{3}{2}} = 0. \qquad (2.5.27)$$

Following the same procedure as for the two stage ion source. Equation 2.5.26 is then divided by U_R and set equal to equation 2.5.27. The terms containing

$U_R^{-\frac{3}{2}}$ can be eliminated and the equation is multiplied by U^2, this leads to:

$$\left(\frac{x_S}{U_S} - \frac{\frac{1}{2}x_D}{2U_{Ref}}\right) U_{ref}^{\frac{3}{2}} U_R^{-1} = \left(\frac{x_S}{U_S} - \frac{\frac{3}{2}x_D}{2U_{Ref}}\right) U^{\frac{1}{2}}. \tag{2.5.28}$$

The potential ratios $\frac{U_{Ref}}{U_R} = \gamma$ and $\frac{U_{Ref}}{U_R} = \frac{\gamma}{\gamma-1}$ are used to further reduce the equation. This leads to

$$\gamma = \frac{\frac{3}{2}x_{D2}}{\frac{1}{2}x_D - 2x_S}. \tag{2.5.29}$$

The spatial focus can then be determined by solving equation 2.5.29 for x_D [62].

2.6 Atomic beam sources

Numerous sources exist for the production of neutral atoms or molecules. These sources include thermal sources, jet sources, and fast beam sources formed by neutralization of ion beams [63]. Atomic beam sources can be used in tandem with ToF-MS to great effect. These atomic beam sources are usually set up in such a way that the beam enters the apparatus orthogonal to the acceleration axis of the ToF-MS. To decide which atom source is best suited for experimental purposes, knowledge of its characteristic properties are needed [64]. Characteristic properties include the angular distribution of the beam, its forward intensity, velocity spread and internal energy. In this section two sources will be discussed, namely the thermal or effusive atom source and the free gas jet source, as these are the atomic beam sources considered for the planned experimental setup in our laboratory.

2.6.1 Effusive beams

For this study a thermal source of tin atoms will be implemented as neutral atom source for the ToF-MS. Thermal atomic sources depend on the principles of the kinetic theory of gases as highlighted in various sources of literature [63; 64]. For effusive sources the sample chamber usually consists of a small chamber containing atoms in gas or vapour form [63]. The size and thickness of the aperture of the sample chambers are much smaller than the mean free path so that the number of collisions experienced by the atoms as they exit the sample chamber is close to zero. Therefore the atoms leave the chamber through effusion and not hydrodynamic flow [65; 66].

The number of atoms, dQ, leaving an effusive source per second traveling in a solid angle $d\Omega$ at an angle of θ, relative to the aperture normal, can then be determined as [66]

$$dQ = \frac{d\Omega}{4\pi} n\bar{v} \cos\theta A_s, \tag{2.6.1}$$

where n is the number of atoms per unit volume, $\bar{v}$ the mean speed of the atoms inside the source, and A_s the area of the source exit. The number density of the atoms, n, can be determined through the ideal gas law relating pressure, p, and temperature, T,

$$p = nkT. \tag{2.6.2}$$

The total number of atoms to leave the source, Q, can be determined by integrating over the solid angle of the forward direction. The solid angle in equation 2.6.1 is taken as $d\Omega = 2\pi \sin\theta d\theta$. Equation 2.6.1 is then integrated in terms of θ from 0 to $\frac{1}{2}\pi$. The total number of atoms to leave the source is then given by

$$Q = \frac{1}{4}n\bar{v}A_s. \tag{2.6.3}$$

In equations 2.6.1 and 2.6.3, two assumptions are inherently true [66]. The first assumption is that all atoms that reach the aperture or slit of the source pass through it and does not have their direction changed [66]. The second assumption is that the spatial and speed distribution of atoms inside the source are not affected by the effusion of atoms from the source [66].

The speed distribution inside the source chamber follows the regular Maxwell distribution [65]. If dN represents the number of atoms within a speed distribution v to $v + dv$ and N represents the total number of atoms per unit volume, the Maxwell distribution gives the following:

$$\frac{dN}{dv} = Nf(v) = \frac{4N}{\sqrt{\pi}}\frac{v^2}{\alpha^3}e^{\frac{-v^2}{\alpha^2}}, \tag{2.6.4}$$

where

$$\alpha = \sqrt{\frac{2k_BT}{m}}. \tag{2.6.5}$$

In the equation above, m is the mass of the atom and k_B the Boltzmann constant. For the case where $v = \alpha$, it can be shown that $d^2N/dv^2 = 0$. Therefore, α can be described as the most probable speed of the atoms inside the source [66]. The other characteristic speeds to consider include the mean speed and the Root mean square (RMS) speed. The mean speed can be defined as [66]

$$\bar{v}_g = \int_0^\infty vf(v)dv = \frac{2}{\sqrt{\pi}}\alpha \approx 1.13\alpha. \tag{2.6.6}$$

In equation 2.6.6 the mean speed, $\bar{v}$, is expressed in terms of the probable speed, α, defined in equation 2.6.5. The RMS-speed can also be defined as [66]

$$v_{RMS,g} = \left[\int_0^\infty v^2f(v)\right]^{\frac{1}{2}} = \sqrt{\frac{3}{2}}\alpha \approx 1.22\alpha. \tag{2.6.7}$$

The *g*-subscript has been used to indicate the speeds are for atoms in a volume of gas. These characteristic speeds hold true for atoms in a volume of gas. In 1920, however, Otto Stern observed that the measured mean speed of atoms in an atomic beam differs from the mean speed of atoms in a gas [67]. The reason for the discrepancy is that the probability of the atom escaping the source chamber is proportional to its speed, this is reflected in the speed dependence of equation 2.6.1. The speed dependence in the beam is then proportional to equation 2.6.4 multiplied by v [66]. The proportionality constant can be determined by normalizing with regards to the full beam intensity, I_0. If $I(v)dv$ represents the beam intensity ($atoms\, s^{-1}\, m^{-2}$) for atoms with velocities between v and $v + dv$, then

$$I(v) = \frac{2I_0}{\alpha^4}v^3 e^{\frac{-v^2}{\alpha^2}}. \tag{2.6.8}$$

Integrating equation 2.6.8 over all speeds equals the full beam intensities [63]. The most probable velocity of atoms in the beam can then be derived from

$$\frac{dI(v)}{dv} = 0. \tag{2.6.9}$$

The most probable speed in the beam, v_B, is then given by

$$v_B = \sqrt{\frac{3}{2}}\alpha \approx 1.22\alpha. \tag{2.6.10}$$

The other two characteristic speeds can then be defined as [66]:

$$\bar{v_B} = \frac{3}{4}\sqrt{\pi}\alpha \approx 1.33\alpha, \tag{2.6.11}$$

for the average speed of atoms in the beam, and

$$v_{RMS,B} = \sqrt{2}\alpha \approx 1.30\alpha, \tag{2.6.12}$$

for the RMS-speed in the beam. Here the subscript B has been used to indicate the speeds are for atoms in atomic beams. The characteristic speeds listed above can be related to the temperature of the beam using equation 2.6.5.

At an angle, θ, relative to the aperture normal, the forward ($v_\parallel$) and transverse ($v_\perp$) velocity components are related by $\frac{v_\parallel}{v_\perp} = \tan\theta$. The velocity components are related to the speed, v, by $v^2 = v_\parallel^2 + v_\perp^2$. Therefore

$$v_\parallel(\theta) = \frac{v}{\sqrt{1 + (\tan\theta)^2}} = v\cos\theta, \tag{2.6.13}$$

and

$$v_\perp(\theta) = \frac{v\tan\theta}{\sqrt{1 + (\tan\theta)^2}} = v\sin\theta. \tag{2.6.14}$$

These relations hold for the most probable, mean, RMS speed and velocity components at an angle θ. The spread in the values of the parallel and transverse velocity components at an angle θ can be calculated using

$$dv_{\parallel}(\theta) = \frac{2\sigma}{\sqrt{1 + (\tan\theta)^2}} = 2\sigma\cos\theta, \tag{2.6.15}$$

and

$$dv_{\perp}(\theta) = \frac{2\sigma\tan\theta}{\sqrt{1 + (\tan\theta)^2}} = 2\sigma\sin\theta. \tag{2.6.16}$$

In equations 2.6.15 and 2.6.16 σ represents the variance of the speed distribution. According to Maxwell Boltzmann statistics the variance of the speed distribution is given by

$$\sigma = \sqrt{\frac{k_B T}{m}}\sqrt{\frac{3\pi - 8}{\pi}}. \tag{2.6.17}$$

The result of these relations is that when a small solid angle of the beam around $\theta = 0$ is selected by skimmers, then the transversal velocity components of the skimmed beam is limited to a small fraction of the forward velocity component. Therefore the Doppler broadening in the transverse direction is reduced. The relationship between the forward velocity component, $v_{\parallel}$, the transverse velocity component, $v_{\perp}$, and angular spread, $\Delta\theta$, for a skimmed beam has been illustrated in Figure 2.11.

The typical number density ($atoms\,m^{-3}$) a distance R away from the beam source can be approximated using [68]:

$$n(R, \theta) = \frac{n_0\cos\theta}{4\pi R^2}dA, \tag{2.6.18}$$

where n_0 can be calculated using equation 2.6.2.

2.6.2 Free gas jets

Other than just an effusive source, a gas jet source was also proposed as a means to introduce tin atoms into the ToF-MS. Argon seeded with tin atoms will be used to form a jet source that can be injected into the system. Supersonic gas jets are useful tools to provide atomic and molecular beams with a well-defined kinetic energy. The theoretical basis for gas jet expansion was first proposed in 1951 [69], with experimental proof following shortly afterwards [70; 71; 72]. One of the most important considerations regarding the gas jet method is pumping speed close to the source as well as the method used to transfer the beam into a high vacuum region [68]. Sufficient pumping is required to keep the pressure low enough in the source chamber to ensure proper functioning of the gas jet.
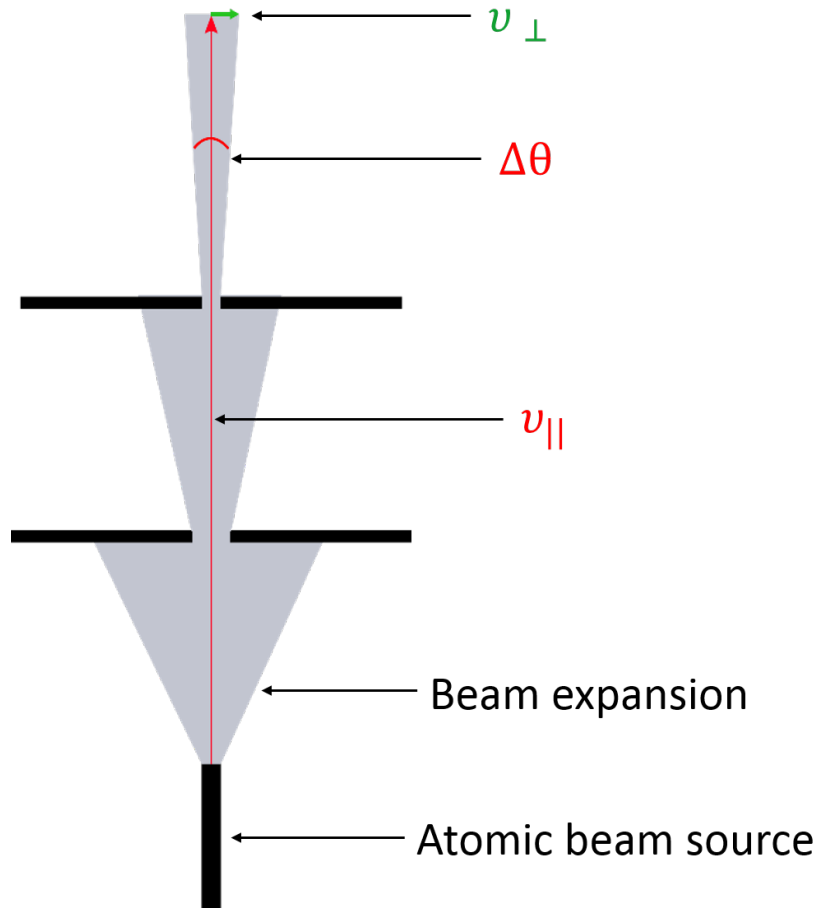
Figure 2.11: The relationship between $v_\parallel$ and $v_\perp$ in a skimmed atomic beam.

When gas expands from a high pressure reservoir through a small orifice into a vacuum chamber, a supersonic gas jet is formed via supersonic free-jet expansion. During the expansion the atoms experience collisions and this leads to adiabatic cooling of the internal energy of the atoms [68]. As the atoms pass through the aperture, collisions occur that propel the atoms primarily in the forward direction, thus increasing the forward velocity of the atoms. Since the expansion takes place adiabatically, the increase in forward velocity must be compensated for. The random thermal motion of the atoms decreases in order to preserve the total energy of the atom. Therefore, during the expansion the atomic beam is accelerated and cooled down.

Before expansion occurs, the thermal energy of the atoms consists of translational, transverse, vibrational and rotational energies. These energies can be expressed as temperature. For a stagnant gas all these temperatures are equal, $T_0 = T_\parallel = T_\perp = T_r = T_v = T_e$ [73]. In this expression T_0 represents the temperature in the source, $T_\parallel$ the temperature in the direction parrallel to the

jet, and $T_\perp$ represents the temperature perpendicular to the jet. T_r and T_v represent the rotational and the vibrational temperature, respectively, of the atoms in the jet. T_E represents the distribution of population over electronic energy levels of atoms.

Cooling of the different temperatures happens at different rates as the gas expands [73]. The translational temperature cools more efficiently than the rotational temperature or the vibrational temperature. This is due to the fact that the cross sections for elastic collisions is larger than the cross section for collision-induced rotational transitions [73]. The cross sections for collision-induced vibrational and electronic transitions are even smaller than both of the other cross sections. Adiabatic cooling of the translational temperature continues until the terminal Mach number is reached [74]. The Mach number is defined as the ratio of the average flow velocity of the expanding gas to the local speed of sound of the gas [74]. At the point of the terminal Mach number the collision frequency in the jet essentially becomes zero and the jet enters a free-flow regime [75]. This region is usually referred to as the "zone of silence". The transverse temperature, however, continues to drop, purely as a result of the physical geometric effects [74]. The atoms with the highest transverse velocity components move away from the centre of the jet and are lost during propagation and skimming. Thus, after the adiabatic expansion the temperature components can be arranged as follows: $T_\perp < T_\parallel < T_r < T_v < T_e$ [73].

The terminal Mach number for a free argon jet can be calculated using [76]

$$M_\infty = 133 \left(P_0 D\right)^{0.4},\qquad\qquad(2.6.19)$$

where P_0 is the pressure in the reservoir measured in atmospheres and D is the diameter of the nozzle measured in centimeters. The translational temperature of the gas as it reaches the terminal Mach number is called the terminal translational temperature. The terminal translational temperature for an argon jet can defined as [73]:

$$T_{\parallel\infty} \approx \frac{T_0}{1 + 5896 \left(P_0 D\right)^{0.8}},\qquad\qquad(2.6.20)$$

where T_0, P_0, and D are measured in Kelvin, atmosphere, and centimeters, respectively.

The gas jet has a complex structure as illustrated in Figure 2.12. The core of the jet is surrounded by a paraboloid-shaped barrel shock boundary [74]. The barrel shock ends at another shock zone called the Mach disk. The Mach disk forms a nearly flat terminal shock wave that is perpendicular to the flow of the beam [74]. Determining the position of the Mach disk is important, since the position of the Mach Disk signifies the end of the "zone of silence" of the jet. As atoms reach the Mach disk their velocities are randomized through
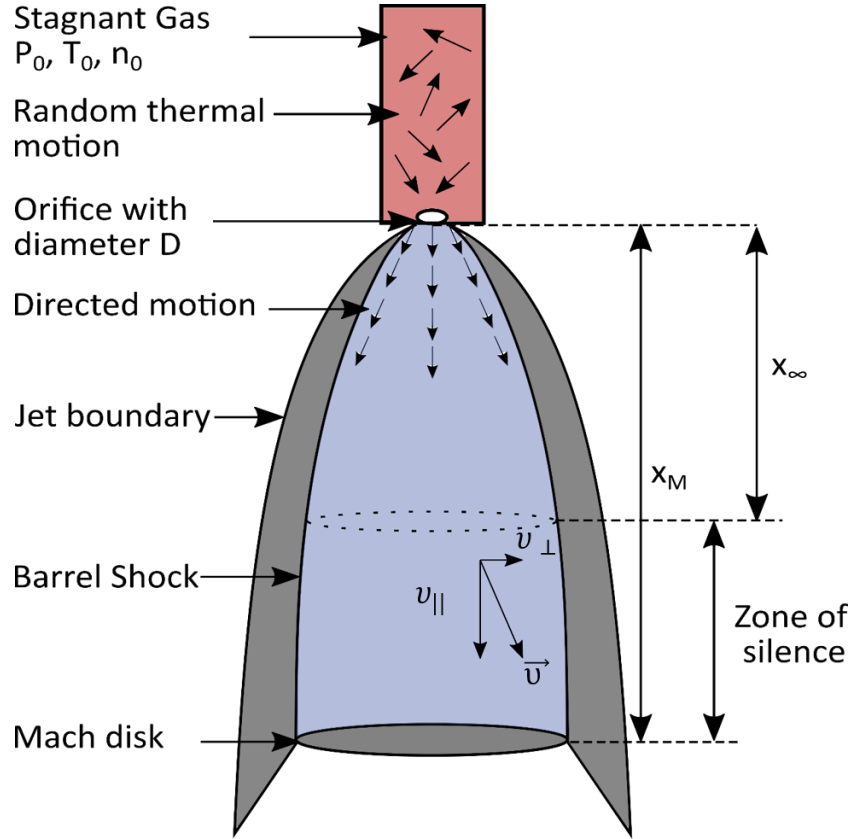
Figure 2.12: The structure of a free gas jet expansion for a stagnant gas with pressure P_0, temperature T_0, and number density n_0.

various collisions with the background gas [74; 77]. Therefore spectroscopy is usually performed after the position of the terminal Mach number and before the Mach disk. This is also the region from which atomic beams are sampled using a skimmer, which typically has a conical shape. The skimmer is placed within the "zone of silence" and the core of the jet expansion is transmitted.

The position of the Mach disk, x_M, can be calculated as [78]

$$x_M = 0.67D\sqrt{\frac{P_0}{P_B}}, \tag{2.6.21}$$

where D is the diameter of the nozzle, P_0 is the stagnation pressure in the reservoir, and P_B is the background pressure inside the vacuum system.

The temperature, T, density, ρ, and the pressure, P, in the supersonic gas jet are related to the corresponding variables of the stagnant gas before expansion. These parameters are related via the effective Mach number, M_{eff}. The effective Mach number at a position x for a mono-atomic gas can be defined

as [78; 77]

$$M_{eff}(x) = 3.26 \left(\frac{x}{D} - 0.075 \right)^{0.67} - 0.61 \left(\frac{x}{D} - 0.075 \right)^{-0.67}, \qquad (2.6.22)$$

where D refers to the nozzle diameter. This expression can be approximated to

$$M_{eff}(x) = 3.26 \left(\frac{x}{D} \right)^{0.67}. \qquad (2.6.23)$$

The temperature, pressure, and the number density of the gas in the supersonic jet can then be expressed in terms of the effective Mach number [69; 76]:

$$\frac{T}{T_0} = \left[1 + \left(\frac{\gamma - 1}{2} \right) M_{eff}^2 \right]^{-1}, \qquad (2.6.24)$$

$$\frac{P}{P_0} = \left[1 + \left(\frac{\gamma - 1}{2} \right) M_{eff}^2 \right]^{\frac{-\gamma}{\gamma - 1}}, \qquad (2.6.25)$$

$$\frac{n}{n_0} = \left[1 + \left(\frac{\gamma - 1}{2} \right) M_{eff}^2 \right]^{\frac{-1}{\gamma - 1}}, \qquad (2.6.26)$$

where γ is the heat capacity ratio $\frac{C_P}{C_V}$. For mono-atomic gases $\gamma = \frac{5}{3}$. The forward velocity of the atoms in the supersonic jet can be approximated in terms of the temperature of the gas. The average forward velocity component, $\upsilon_{\parallel,j}$, is then given by [68]

$$\upsilon_{\parallel,j} = \sqrt{\frac{5k_B(T_0 - T)}{m}}. \qquad (2.6.27)$$

If the gas jet is allowed to cool such that $T \ll T_0$, the expression above can be simplified to

$$\upsilon_{\parallel,j} = \sqrt{\frac{5k_B T_0}{m}}, \qquad (2.6.28)$$

where k_B is the Boltzmann constant.

If the argon jet is seeded with tin atoms of a relative small concentration before jet formation, then the conditions of the jet are determined by the properties of the argon gas. The translational temperature of the tin atoms is expected to be similar to the translational temperature of the argon atoms.

2.7 IBSimu Ion Beam Simulations

Ion Beam Simulator or IBSimu is an ion optical computer simulation library developed by Taneli Kalvas of the University of Jyväskylä, Finland [79]. IBSimu was used to simulate particle trajectories within a ToF-MS. The parameters

used for the ToF-MS in the simulation were taken from a laboratory set-up under development at Stellenbosch University. IBSimu is an open-source C++ library that can be used on both Linux and Windows.

IBSimu is capable of solving electric fields in one-dimensional, two-dimensional, or three-dimensional simulation geometries, where the simulation space is discretized as evenly sized square Cartesian grids [79]. The nodes of the grid can be defined as vacuum nodes, solid nodes, Neumann boundary nodes, or Dirichlet boundary nodes. The Neumann boundary condition implies that the first derivative of the potential with respect to the outward normal of that surface stays constant. The Dirichlet boundary conditions implies that the potential is constant at that surface. In IBSimu simulations the solid geometries in the simulation all have the Dirichlet boundary conditions. Solids can be defined mathematically or in AutoCAD. The AutoCAD files can be imported, but this currently only works for the two-dimensional case [79].

IBSimu calculates the electric potential, electric field, magnetic field, and particle trajectories within the simulation area. To calculate the electrostatic potentials , IBSimu uses the the finite difference method (FDM) to solve Poisson's equation on the nodes of the Cartesian grid [79]. The FDM is a method of solving partial differential equations by approximating them with linear combinations of function values at the nodes of a grid. Poisson's equation for electrostatics relates the electrostatic potential to the charge density and is given by

$$\nabla^2 \phi = \frac{-\rho}{\epsilon_0} \qquad (2.7.1)$$

where ϕ refers to the electrostatic potential, ρ the charge density, and ϵ_0 the permittivity of free space. The FDM can then be used to determine the potential for the various nodes within the simulation area. Once Poisson's equation for the electrostatic potential has been solved, the electric field can be determined. The external electric field is related to the electrostatic potential through the gradient of the potential

$$\vec{E} = -\vec{\nabla}\phi. \qquad (2.7.2)$$

The electric field is calculated using numerical differentiation and interpolation of the potential at neighbouring mesh nodes. Once the external electric field has been determined, the force acting on charge particles within the simulation area can be calculated.

Once the forces within simulation area are determined, the equations of motion of each particle in the simulation can be set up. The equations of motion will

resemble the following

$$m\ddot{\vec{r}}_j = q_j\vec{E} + q_j\dot{\vec{r}}_j \times \vec{B} + q_j \sum_{i \neq j}^{N} \frac{q_i}{4\pi\epsilon_0} \frac{\vec{r}_{ij}}{|\vec{r}_{ij}|^3}, \tag{2.7.3}$$

where $\vec{r}_j$ is the position vector of the jth ion and $\dot{\vec{r}}_j$ and $\ddot{\vec{r}}_j$ the first and second derivative of the vector, respectively. The first two terms in equation 2.7.3 represent the Lorentz force acting on the jth particle, while the last term accounts for the repulsion between the jth ion and the rest of the ions present. Particle trajectories are then determined by integrating the equations of motion with an embedded Runge-Kutta method. The particle trajectories are then introduced to the simulation area. Therefore IBSimu can be used to define geometries and simulate particle trajectories through the given geometries.

Chapter 3

Planned Experimental Setup

The planned experimental setup will be described in this section. Due to administrative problems the actual time-of-flight mass spectrometer (ToF-MS) was only received in August 2018. Therefore the instrument could not be implemented within the time frame of this MSc project. However, two experimental setups have been designed and developed as far as possible by the author. Both setups make use of resonance ionization and time-of-flight mass spectrometry, but the sample introduction method differs.

The design and construction of the ToF-MS will be described first. The experimental setup for using an effusive beam will then be described, followed by the planned setup to produce a tin seeded argon jet.

3.1   Time-of-flight mass spectrometer

The ToF-MS to be used in this setup has been illustrated in Figure 3.1. The instrument can be divided into three sections namely the ionization region, the field free region, and the reflectron. This instrument was provided to the CSIR by Kore Technology, and is made available to Stellenbosch University on a long term lease from the CSIR National Laser Centre Rental Pool. The instrument has been applied at the CSIR for research on small molecules [80].

The ionization region consists of a backplate, an extraction ring with an embedded mesh, and intermediate electrode, and a final grounded ring with an embedded mesh. The backplate, the extraction ring, and the intermediate electrode are connected to high voltage power supplies. The backplate is set to 2 kV, while the extraction ring is supplied with 1.6 kV. The intermediate electrode is set to 0.9 kV.

The reflectron consists of a backplate, a reflector plate, an intermediate electrode, a grounded electrode, and 21 ring electrodes. The reflector and the

intermediate electrode are supplied with 2 kV and $0.8 - 1.2$ kV respectively. The ring electrodes are placed between the reflector and the grounded electrode and are connected through a resistor chain, allowing the electrode potentials to float to the values determined by the resistor chain and the voltage applied to the reflector.

The detector is placed in the field free drift region. The original detector is in the process to be replaced by a dual microchannel plate (Photonis APD 2MA 18/12/10/12 D 60:1, part number 35691). The detector is fitted to a high-speed pre-amplifier (1.5 ns rise time, 20 times analogue gain).

A 3 mm aperture between the ionization region and the field free region and turbo-molecular pumps in both regions facilitate differential pumping.

3.2   Effusive atomic beam experiment

The optical setup to be used in for this experiment has been illustrated in Figure 3.2.

The setup consists of three different lasers. The first is a Nd:YAG (Neodymium-doped Yttrium Aluminium garnet) Pro-270-10 Quanta-Ray Spectra-Physics laser. This laser well be used to pump two dye lasers. The Nd:YAG operates at 1064 nm. This wavelength is then upconverted to 355 nm by means of frequency doubling, followed by sum-frequency mixing. The laser output at 355 nm is ≈ 550 mJ per pulse with a pulse duration of 10 ns and a repetition rate of 10 Hz. The laser pulse is split by a beam splitter and directed into the two dye lasers. The first dye laser is the Sirah CSTR-D-24 dye laser. This laser will be operated using Rhodamine B (alternatively called Rhodamine 610), which has a tuning range of $588 \rightarrow 632$ nm. The laser light provided will be used as the second resonant excitation and subsequent ionization step in the RIS scheme (see Table 2.4). The second dye laser is the Lambda Physik Fl 3001 laser. The dye used in this laser is either going to be Rhodamine 6G (Rhodamine 590) with a tuning range of $563 \rightarrow 597$ nm or Coumarin 47 (Coumarin 460) with a tuning range of $442 \rightarrow 479$ nm. The choice of dye will depend on the RIS scheme being used (see Table 2.4). This laser will provide the first resonant excitation step in the RIS scheme.

The laser light provided by the Lambda Physik laser will be frequency doubled in a second harmonic generation unit. This unit consists of two crystals, a compensator and a BBO (Beta Barium Borate) crystal. The laser light first passes through the compensator, which is used to correct for the beam steering introduced when passing through the BBO crystal. The BBO crystal is responsible for frequency doubling of the incident laser light. This is
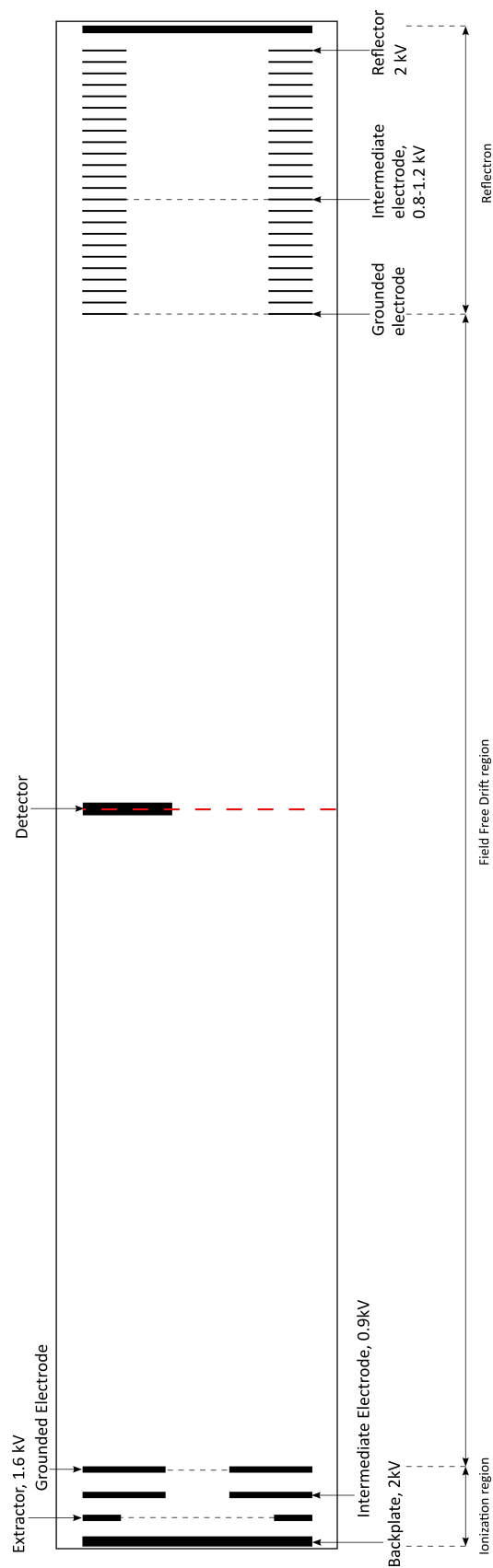
Figure 3.1: The ToF-MS to be used in the experimental setup. The red dashed line indicates the interface between the two regions in the simulation as discussed in Chapter 4.
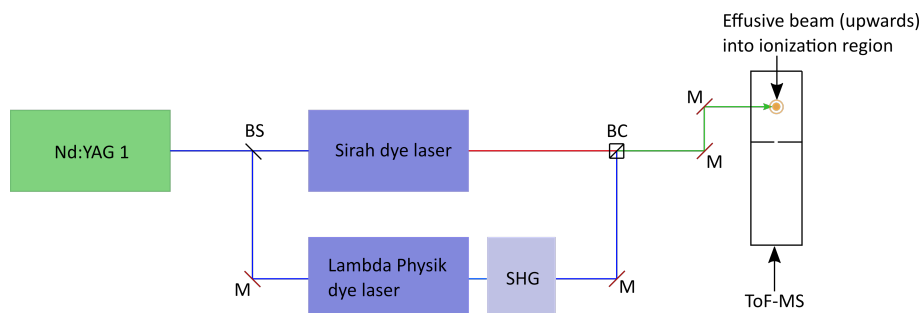
Figure 3.2: Schematic diagram of the experimental setup to be used to perform resonance ionization spectroscopy (RIS) on an effusive beam of Sn atoms. Components to be used: Beamsplitters (BS), mirrors (M), a second harmonic generation stage (SHG), Glan Taylor beam combiners (BC), ToF-MS, and an effusive atomic beam source.

necessary to produce laser light with wavelengths < 400 nm. The BBO crystal makes use of type I phase matching, meaning that the vertically polarized fundamental light is converted to horizontally polarized second harmonic light.

The beams from the two dye lasers are combined in a Glan Taylor beam combiner. The Glan Taylor prism is orientated to transmit the vertically polarized light from the Sirah dye laser, and reflect the horizontally polarized frequency doubled light from the Lambda Physik dye laser. Two additional mirrors are used to steer the combined beam into the ionization region of the ToF-MS.

In the ToF-MS the laser light will intersect the effusive atom beam. This laser light will be incident perpendicular to the atomic beam, in order to reduce Doppler broadening. Once the atomic beam has been ionized the ions will be accelerated by the electric field present in the ToF-MS.

The effusive source has been illustrated in Figure 3.3. A tin sample is placed in a long channel (a modified hypodermic needle) embedded in a copper housing. The hypodermic needle is resistively heated by passing a current through it. As the needle heats up, the tin will be vaporized and will start effusing through a small aperture at the top into the ToF-MS. This type of source has been tested successfully with ytterbium at Stellenbosch University and is expected to be as useful for Sn that has a lower melting point.

The effusive source will be placed underneath the ionization region of the ToF-MS and the beam will travel vertically into this region. Two skimmers will be used to collimate the atomic beam. The skimmers are also useful for reducing the transverse velocity spread of the atomic beam, as discussed in Section 2.6.1.
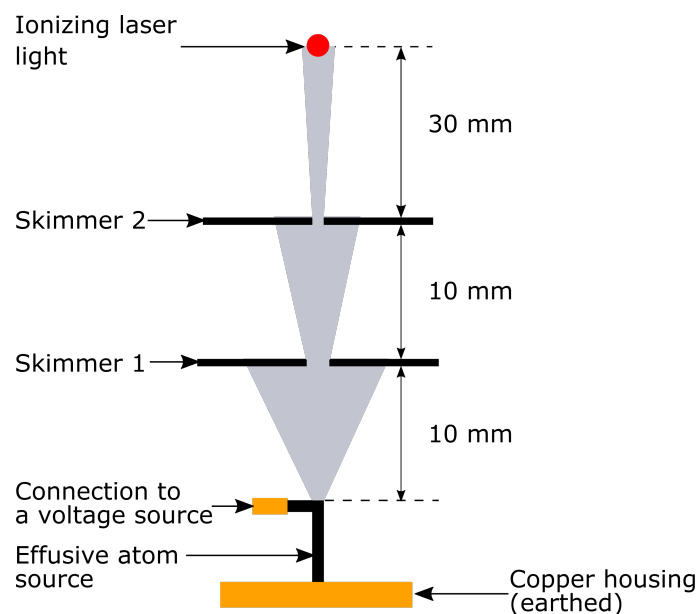
Figure 3.3: Schematic of the atomic beam source to be used to produce an effusive tin beam.

The effusive beam source described above, has been designed and constructed (See Figure 3.4). It consists of a metallic frame designed to fit into the one vacuum flange at the bottom of the ionization chamber of the ToF-MS, a copper housing and three hypodermic needles. The skimmer setup will still be added at a later date.
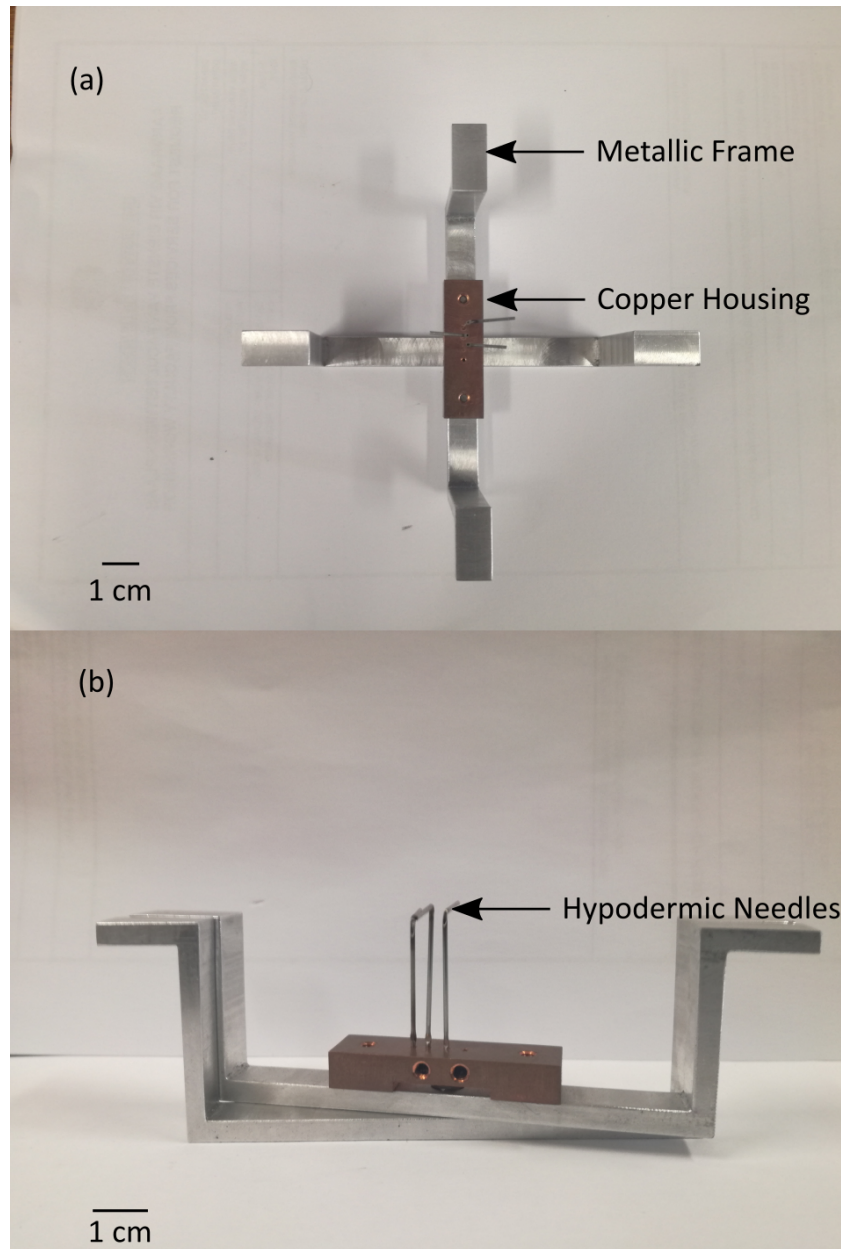
Figure 3.4: Photos of the atomic beam source to be used to produce an effusive tin beam ((a) top view and (b) side view). The metalic frame can swivel to make it easier to maneuver into the vacuum chamber. Only one of the hypodermic needles will be heated at a time.

3.3   Supersonic jet experiment

The laser setup for this part is the same as described in the previous section, but with the addition of a second Nd:YAG laser. The second Nd:YAG is a Continuum Powerlite PL8020 laser. The fundamental laser wavelength is 1064

nm, which undergoes frequency doubling creating 532 nm laser pulses. The laser operates at 10 Hz with a pulse duration of 10 ns. This laser will be used as a dedicated ablation laser, vaporizing tin. The vaporized tin is then seeded into an argon jet. The proposed laboratory setup is illustrated in Figure 3.5.
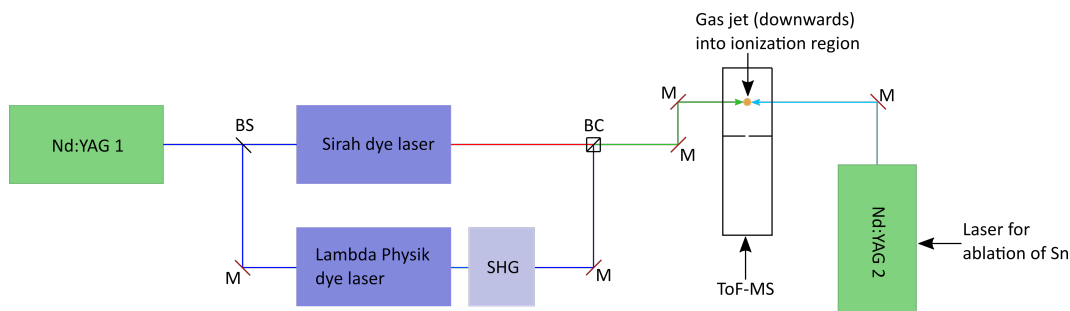
Figure 3.5: Schematic diagram of the experimental setup to be used to perform resonance ionization spectroscopy (RIS) on a supersonic gas jet seeded with Sn atoms. Components to be used: Beamsplitters (BS), mirrors (M), a second harmonic generation stage (SHG), Glan Taylor beam combiners (BC), ToF-MS, and a gas jet atomic beam source.

The dye lasers will be using the same dye as described in the previous section, since the same RIS schemes will be used. The major difference between this setup and the setup for the effusive atomic beam is the sample introduction by means of laser ablation and a supersonic gas jet. The gas jet source is a separate chamber attached to the ToF-MS. The gas jet chamber is illustrated in Figure 3.6. Tin metal is inserted in a grove of a movable rod in the sample housing. The rod will be moved by a stepper motor during ablation to keep the ablation area from being depleted. The ablated atoms are seeded into a pulsed argon jet that is synchronized with the ablation laser. Below the sample chamber there will be a set of deflection plates. During the ablation process some of the tin can be ionized and the deflection plates will steer the already ionized tin atoms away from the ToF-MS. This ensures that only neutral atoms enter the ToF-MS.

The gas jet source has been designed by the author and manufactured by the in-house mechanical workshop staff, as seen in Figure 3.7. A commercial rotational feedthrough is used to connect the movable rod to the stepper motor. The chamber has been vacuum tested, and is ready for implementation.
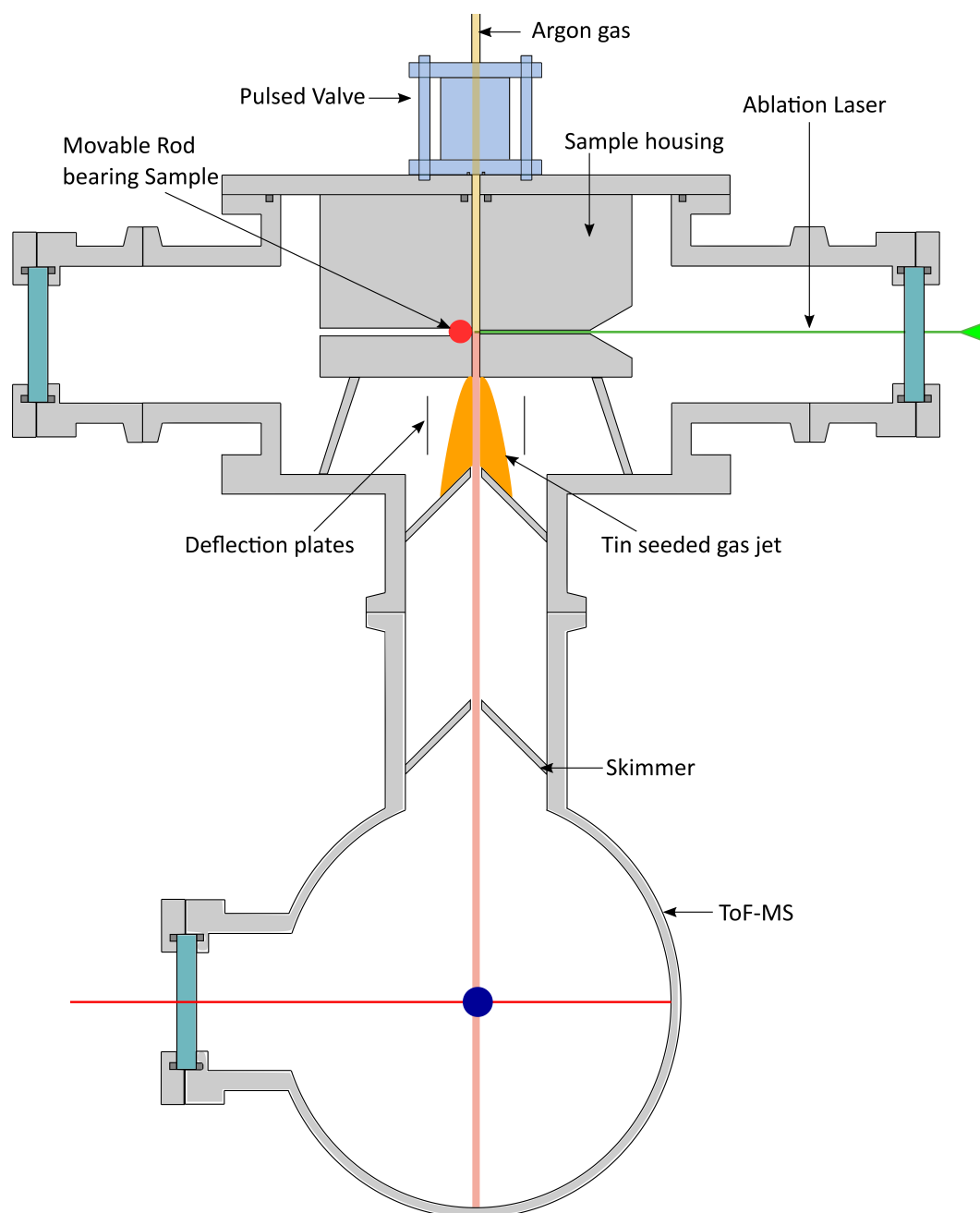
Figure 3.6: Schematic of the gas jet chamber attached to the ToF-MS.
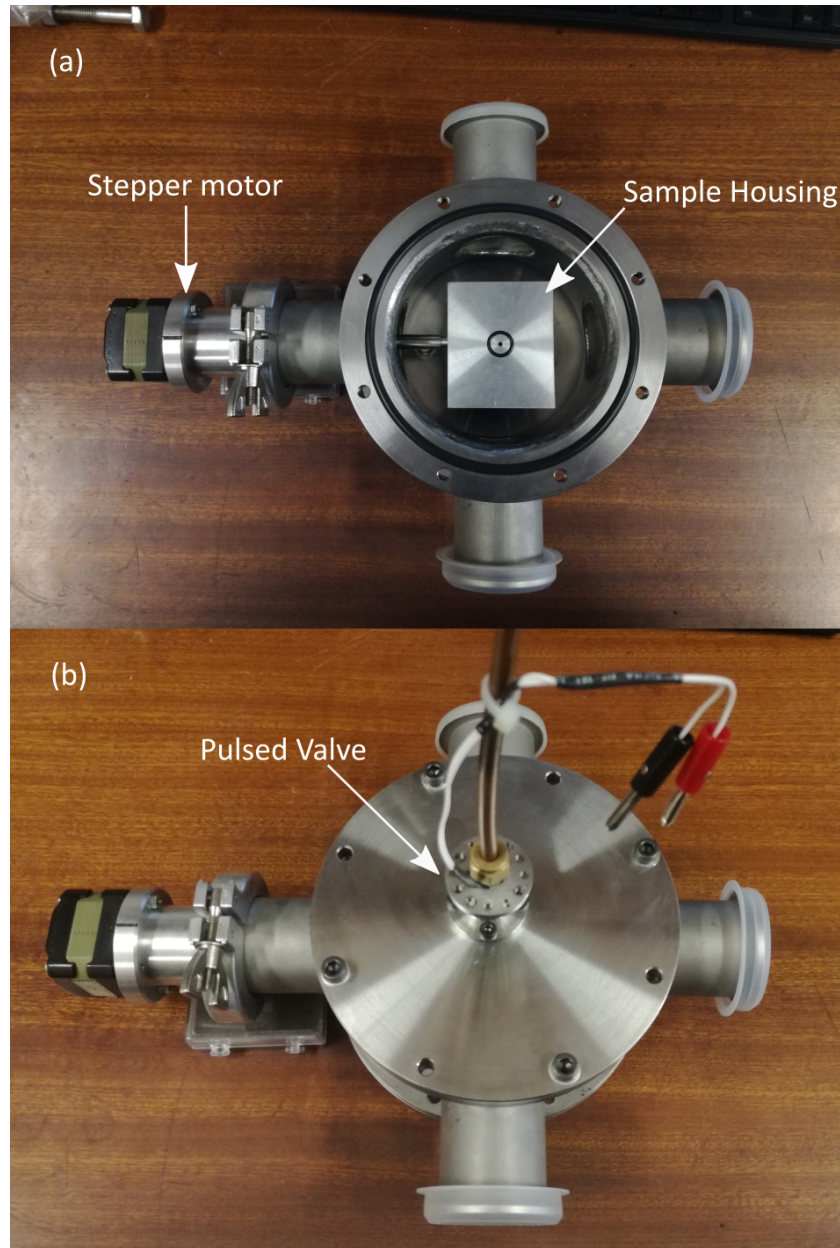
Figure 3.7: Photos of the ablation source chamber to be used to produce a seeded tin gas jet. Both are viewed from the top (a) without the top cover and (b) with the top cover and pulsed valve fitted.

Chapter 4

Simulating a time of flight mass spectrometer

The IBSimu library was used to simulate ions travelling through a Time-of-flight mass spectrometer (ToF-MS). The principles of the IBSimu library were briefly described in section 2.7.

In this section the code used in the simulations will be explained. The simulations are split up into two sections. The first section simulates the ionization region of the ToF-MS, while the second section simulates the reflectron portion of the instrument. This has been illustrated in Figure 3.1, the simulation has been split at the red dashed line. Both sections of the simulation follow the same general structure. This structure will be explained below. For the full code see Appendix A.

As mentioned previously, solids can either be defined mathematically or using AutoCAD. Before the acceleration grids can be constructed the geometry of the simulation area needs to be defined. This can be done as follows

```
1   Geometry geom( MODE_3D, Int3D(91,301,91), Vec3D(−0.045,0,−0.045), 1e−3 );
```

The first argument of the statement specifies the dimension of the simulation, in this case the simulation area is defined as three dimensional. The *Int3D*-argument defines the size of the simulation mesh. For this case it has 91 nodes along both the x- and z-axes and 301 nodes along the y-axis. The y-axis has been chosen to be parallel to the acceleration axis of the ToF-MS. The third argument is used to define the origin of the simulation area. The last argument gives the spacing between nodes in meters, in this case the nodes are separated by 0.001m. After the simulation area has been defined, the backplate and the acceleration grids of the ToF-MS have to be defined.

For the purposes of this simulation the backplate as well as the acceleration grids of the ToF-MS were described mathematically. An example of the code

64

to define these solid objects is:

Listing 4.1: Describing solid geometries

```
1  bool solid1( double x, double y, double z )
2  {
3      double r = sqrt(x*x+z*z);
4      return( y <= 0.004 && r >= 0.0);
5  }
```

This example of code defines a circular disk in Cartesian coordinates positioned perpendicular to the y-axis. The disk starts at the origin and is 0.004 m thick along the y-axis. The disk is solid for the radius $r = \sqrt{x^2 + z^2} \geq 0$ around the y-axis. Similar code was used to define the acceleration grids of the ToF-MS. The objects described by the code above need to be defined and inserted into the simulation area. This is done using:

Listing 4.2: Defining solids

```
1  Solid *s1 = new FuncSolid( solid1 );
2      geom.set_solid( 7, s1 );
```

The object is constructed using the *new* operator in C++. The defined solid is then inserted into the simulation area using the set_{solid} function. User defined solids are assigned numbers and the numbering starts at 7. The boundaries of the simulation area are assigned numbers 1 to 6.

After the geometry has been defined the potentials of the grids as well as the boundary conditions for the simulation area need to be defined.

Listing 4.3: Defining potentials and boundary conditions

```
1  geom.set_boundary( 1, Bound(BOUND_NEUMANN,      0.0  ) );
2  geom.set_boundary( 2, Bound(BOUND_NEUMANN,      0.0  ) );
3
4  geom.set_boundary( 7, Bound(BOUND_DIRICHLET,  2.0e3) );
```

In the code above, 1 and 2 refer to the minimum and maximum x boundaries. These boundaries are assigned Neumann boundary conditions. The last line assigns a Dirichlet boundary to the first user defined solid. The potential assigned to this solid is 2000 V. The boundary conditions have to be defined in a similar way for all user defined solids as well as the minimum and maximum y- and z- boundaries. After all the boundaries have been described, the mesh for the simulation area is built using:

```
1  geom.build_mesh();
```

This is followed by defining objects that can be used to store electric potentials and to calculate electric fields.

```
1  MeshScalarField scharge( geom );
2  MeshScalarField scharge_ave( geom );
3  MeshVectorField bfield;
4  EpotEfield efield( epot );
5  field_extrpl_e efldextrpl[6] = { FIELD_EXTRAPOLATE, FIELD_EXTRAPOLATE,
6                        FIELD_SYMMETRIC_POTENTIAL, FIELD_EXTRAPOLATE,
7                        FIELD_EXTRAPOLATE, FIELD_EXTRAPOLATE };
8  efield.set_extrapolation( efldextrpl );
```

The *MeshScalarField* is a scalar electric potential field based on the mesh in
the geometry of *geom*. The *EpotEfield* object is used to calculate the electric
field in the simulation area from the electric potential data.

The final part of the code is responsible for finding self-consistent solutions for
the electric potential and beam propagation in the geometry of the simulation.
This is done using an iterative method.

Listing 4.4: Particle beam parameters

```
1  for( size_t i = 0; i < 5; i++ ) {
2      solver.solve( epot, scharge );
3      efield.recalculate();
4      pdb.clear();
5      pdb.add_cylindrical_beam_with_velocity( N, J, q, m,
6                            v, dv_p, dv_t,
7                            c,
8                            dir1,
9                            dir2,
10                           r );
11     pdb.iterate_trajectories( scharge, efield, bfield );
12     }
```

The iterator first solves for the electric potential without the presence of parti-
cles. The electric field is then calculated from the potential using *efield.recalculate*();.
The particle beam is then defined by *add_cylindrical_beam_with_velocity*.
This function defines the particle beam as a disk that will propagate through
a three dimensional geometry, forming a cylindrical beam. These particles are
propagated through the geometry and the space charge effect of the beam is
calculated.

The *add_cylindrical_beam_with_velocity* function takes numerous arguments.
N refers to the number of particles per disk and is the number of ions that
will be propagated in the simulation, J is the beam current density (in units
of $Cm^{-2}s^{-1}$), q is the charge of the particles in terms of electron charge, m
refers to the mass in atomic mass units. The next three arguments state the
speed of the beam, v, as well as the parallel, dv_p, and transverse, dv_t, speed
distributions. For these arguments the speed distribution is defined parallel

and transverse to the speed of the beam. The propagation direction of the beam is determined by crossproduct of two vectors called $dir1$ and $dir2$.

The particle beam is defined as a disk with starting position centered around c with a radius r. c is defined with 3 coordinates (x, y, z). The disk is orientated perpendicular to the velocity of the beam, therefore in the plane defined vectors $dir1$ and $dir2$.

The velocity components dv_p and dv_t are sampled from a Gaussian distribution with a standard deviation $\sqrt{\frac{k_b T}{m}}$, where T is the temperature in the parallel or transverse directions [79].

The beam current density is used to calculate the space charge effects of the ions and can be understood in the following way. The defined disk is a two dimensional projection of the three dimensional volume where the atomic beam and the laser pulse overlap, with a thickness h, a volume $V = \pi r^2 h$, and a particle density $n = \frac{N}{V} = \frac{N}{\pi r^2 h}$. Therefore the current density

$$J = \frac{N}{\pi r^2 h}\, vq\, e. \tag{4.0.1}$$

In the real experiment J will be the current density of the travelling ion beam after ionization but before it has been accelerated by the electric field.

The code example showed above (Listing 4.4) was used to introduce four different beams into the simulation area. Three beams of charged particles and one neutral beam was introduced. The three beams were defined to represent the three most abundant isotopes of Tin and their abundances. The three isotopes were ^{120}Sn, ^{118}Sn, and ^{116}Sn.

Finally the data from the simulation can be extracted by using IBSimu's inbuilt diagnostics function.

Listing 4.5: Exporting particle diagnostics

```
1  std::vector<trajectory_diagnostic_e> diagnostics;
2      diagnostics.push_back( DIAG_T  );
3      diagnostics.push_back( DIAG_X   );
4      diagnostics.push_back( DIAG_VX );
5      diagnostics.push_back( DIAG_Y  );
6      diagnostics.push_back( DIAG_VY );
7      diagnostics.push_back( DIAG_Z  );
8      diagnostics.push_back( DIAG_VZ );
9      diagnostics.push_back( DIAG_MASS  );
10     TrajectoryDiagnosticData tof_effusive;
11     pdb.trajectories_at_plane( tof_effusive, AXIS_Y, 0.3, diagnostics );
12     tof_effusive.export_data   ( "tof_effusive.txt" );
```

A vector object *diagnostics* is defined and populated with the time, position, as well as the velocity components of the beam. The mass of each particle is also stored. The data are taken at a plane along the *y*-axis and are stored as a *.txt* file.

The data stored using this code can also be binned using any of the stored variables. Binning with respect to the arrival time data is shown in Listing 4.6.

Listing 4.6: Histogram data

```
1  const TrajectoryDiagnosticColumn &time = tof_effusive(0);
2
3  Histogram1D tofeffusive_histo( 61, time.data());
4  vector<double> time_data = tofeffusive_histo.get_data();
5  ofstream of_histo( "tofeffusive_histo.txt" );
```

The diagnostic data were binned (in 61 bins in this example) using the scatter time data. The number of bins was chosen for each simulation in order to obtain a suitable time resolution over the relevant time range. There has to be a limit to the smallest bin size as the time resolution of the code has some limitation. This limit has not been investigated in this study. Producing a histogram in this fashion can then be used to generate a graph of the number of particles versus the arrival time. If such a histogram is produced from the data collected at the position of the detector of the instrument it represents the time-of-flight mass spectrum that would have been recorded.

The diagnostic data were also used to integrate the simulation of the ionization region and the reflectron-detector region of the ToF-MS. Data recorded at the end of the ionization region simulation region were used as the input data for the reflectron portion in order to simulate beam propagation through the whole instrument. The diagnostic data include all coordinates and velocity components of each ion, therefore no information is lost when the data are transferred between the two simulations.

Chapter 5

Results and discussion

In this chapter the results obtained from experimental measurements, calculations, and the simulations described in Chapter 4 will be reported and discussed. The second harmonic generation unit described in Chapter 3 has been calibrated and the results will be reported in this chapter. The beam parameters used in the simulations can be justified using the theory laid out in Chapter 2 section 2.6. After reporting on the BBO calibrations and the calculations of the beam parameters, the simulated results will be discussed.

5.1 Second harmonic generation unit calibration

The second harmonic generation (SHG) unit was briefly described in Chapter 3. It consists of two crystals, a compensator and a BBO (Beta Barium Borate) crystal. The two crystals are driven by a stepper motor. The stepper motor adjusts the angle of the crystals relative to the incident laser light. This adjusts the phase matching needed to achieve second harmonic generation. The steps of the stepper motor are therefore related to the phase matching angle. Phase matching has been described in Chapter 2.4.4.

To calibrate the SHG unit, the Lambda Physik dye laser is set to double the wavelength that is needed in the experiment. For example, if 250 nm is required the dye laser will be set to 500 nm. With the dye laser set to the desired wavelength, the crystals of the SHG unit will be rotated by the stepper motor and the intensity of the second harmonic laser light will be measured as a function of the number of steps of the stepper motor. This process is repeated for a wavelength region surrounding the desired second harmonic wavelength. Once enough data has been collected a calibration curve relating wavelength and number of steps can be plotted. This calibration curve can be used to control the stepper motor using a program such as LabView. The desired wavelength is then used as input and the correct number of steps to achieve

the wavelength is determined using the calibration. The stepper motor moves this number of steps, changing the orientation of the SHG crystals and SHG is achieved.

The SHG unit was calibrated for a wavelength region around 214 nm. This wavelength was used as the first excitation of zinc. Zinc is the element of interest in another project running in the same laboratory at Stellenbosch University.

The theoretical phase matching curve for this wavelength can be determined from the theory outlined in Chapter 2.4.4. The angle dependent extraordinary refractive index at various angles can be determined by using equation 2.4.7. For a BBO crystal the refractive indices n_2^o and n_2^e at 214 nm are 1.8284 and 1.6622, respectively [81].

After calculating the angle dependent extraordinary refractive index, the wave vector mismatch, Δk, can be calculated using equation 2.4.5. To calculate Δk, $n_1^0 = 1.6879$ [81] and $\omega_2 = \frac{2\pi 3 \times 10^8}{214 \times 10^{-9}}$ were used. The $L^2 \text{sinc}^2 \left(\frac{\Delta k L}{2} \right)$ factor was calculated using the values of Δk, with $L = 0.0005$ m. $L^2 \text{sinc}^2 \left(\frac{\Delta k L}{2} \right)$ as a function of the angle θ has been plotted in Figure 5.1
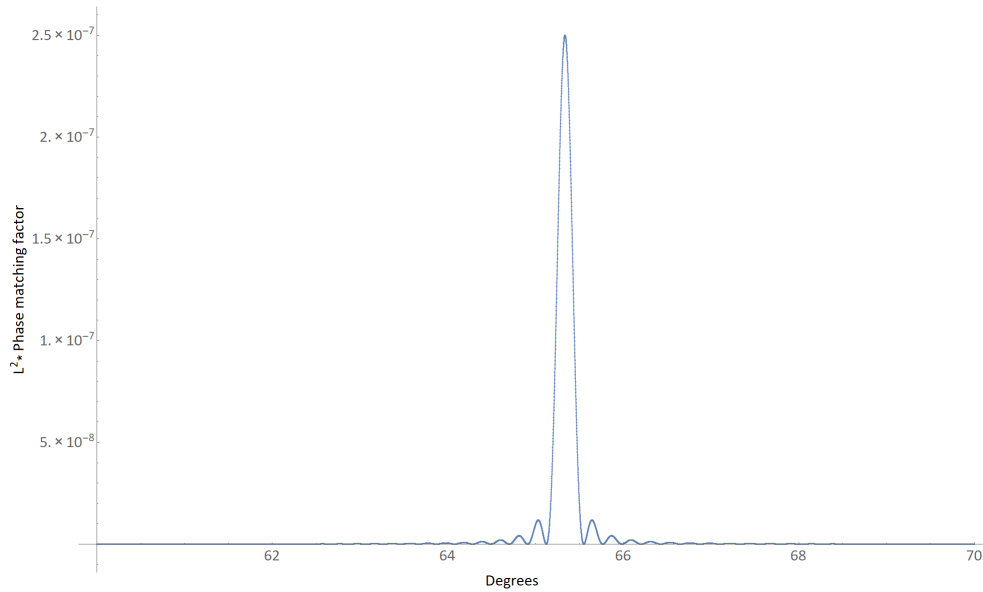
Figure 5.1: The thoeretical phase matching curve measured as a function of angle.

After the theoretical phase matching curve was determined, phase matching curves were measured in the laboratory. It was expected that the measured

curve phase matching curves should look similar to the theoretical curve plotted in Figure 5.1. A single phase matching curve was measured every 0.2 nm from 213 nm to 215 nm. As an example, the measured phase matching curve for 214 nm has been plotted in Figure 5.2. The measured phase matching curve agrees with theoretical phase matching curve.
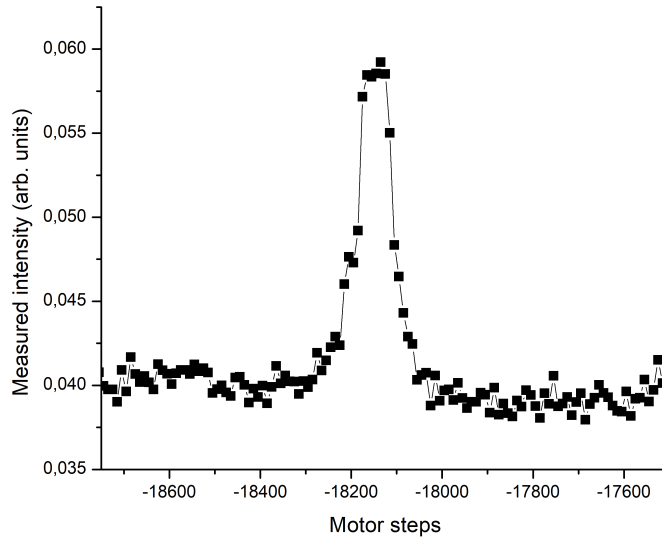
Figure 5.2: The measured phase matching curve for 214 nm as a function of motor steps.

After all the phase matching curves were measured, the peaks were analysed to determine the centre of the peak in terms of the number of steps. The second harmonic wavelength as a function of stepper motor steps have been plotted in Figure 5.3. The calibration curve was used to update a LabView program that controls the SHG unit.
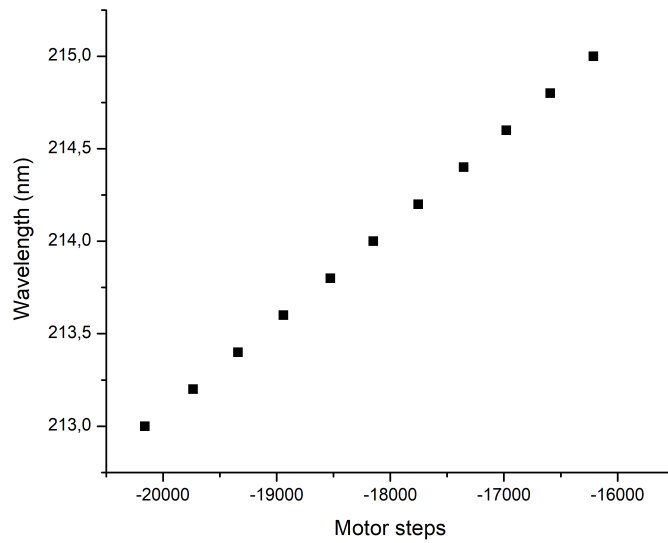
Figure 5.3: The calibration curve needed to calibrate the second harmonic generation unit.

Following the calibration of the SHG unit, the reproducibility of the unit had to be tested. Phase matching curves were measured for 214 nm and after each measurement the SHG unit was zeroed (the crystals were returned to the zero angle). The centres of the peaks in terms of wavelength were extracted from the measured spectra using a Gaussian fit. The extracted wavelengths were compared for the different measurements to see whether the SHG unit will move to the same phase matching angle each time. The measured peaks should be centred around 214 nm in the measured spectra, deviation from this wavelength indicates that the SHG unit does not move back to the exact position every time. Figure 5.4 shows the extracted wavelength for each measurement with the error bars representing the standard error of the fit. From the data represented in Figure 5.4 it is observed that the centre of the peaks show a standard deviation of 1.8×10^{-3} nm relative to 214 nm.
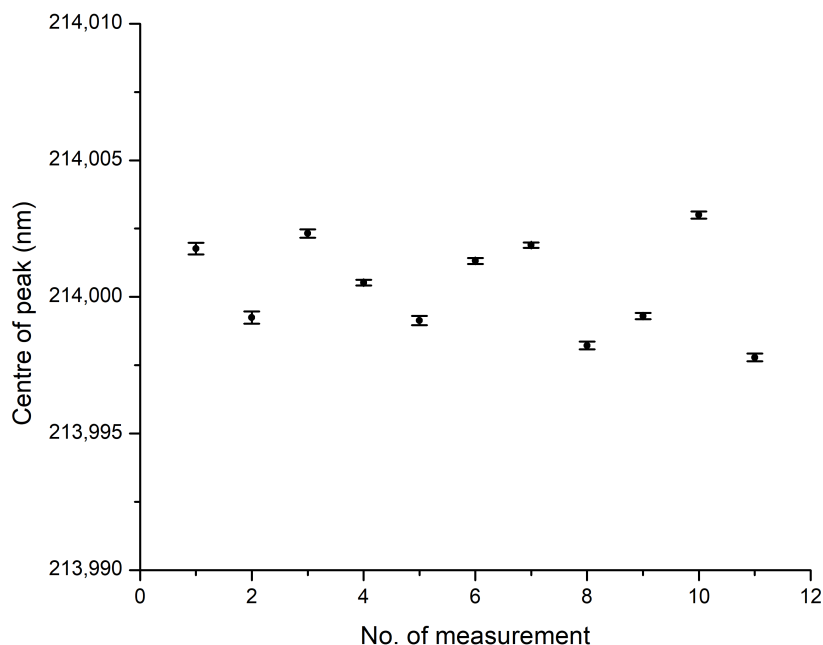
Figure 5.4: The second harmonic wavelengths extracted from phase matching curves to check the reproducibility of the second harmonic generation unit. The error bars represent the standard error from the fit.

While 214 nm will not be used in the experimental setup for Sn, the experimental techniques needed to do the calibration will not change. The calibration of the SHG unit will be repeated when the desired wavelength is changed to 286.3 nm.

5.2   Atomic beam source calculations

The atomic beam parameters have been determined for two different regimes, namely the effusive region and the supersonic regime. From the perspective of the simulations, the most important aspect of both the effusive and the supersonic regime is the speed and speed distribution of the atoms produced in either regime.

5.2.1   Effusive sources

The average speed of atoms in a beam produced through an effusive source is given in equation 2.6.11. For this study an effusive source has been designed to produce a beam of tin atoms. The melting point of tin is 232 °C (505

K). The boiling point of tin metal is 2603 °C (2876 K). We assume that local heating to temperatures of ~ 1350 K (~ 1077 °C) will be achievable in the experimental Sn source. From equation 2.6.11 the average speeds of the three different isotopes at 1350 K in the effusive beam will be

$$\bar{v} = \frac{3}{4}\sqrt{\pi}\sqrt{\frac{2k_B T}{m}} \approx 580\,\mathrm{m/s}. \tag{5.2.1}$$

Using equation 2.6.17 the variance of the speed distribution is

$$\sigma = \sqrt{\frac{k_B T}{m}}\sqrt{\frac{3\pi - 8}{\pi}} \approx 208\,\mathrm{m/s}, \tag{5.2.2}$$

giving a width $dv = 2\sigma = 416$ m/s.

The parallel and transverse velocity components in a skimmed beam can be determined from the experimental geometry. From the planned experimental setup (see Figure 3.3) we estimate the maximum angle for the velocity of the atoms in the beam to be $\theta_{max} = \frac{\Delta\theta}{2} = 1.7°$. Equations 2.6.13 and 2.6.14 can be used to estimate the parallel and transverse velocity components at a given angle. For the three isotopes $\bar{v}_{\parallel} \approx 580$ m/s for any $\theta \leq \theta_{max}$. However $\bar{v}_{\perp}$ changes more with the angle, for example $\bar{v}_{\perp}(\theta_{max}) \approx 17$ m/s, $\bar{v}_{\perp}(\frac{\theta_{max}}{2}) \approx 9$ m/s, and $\bar{v}_{\perp}(0) \approx 0$ m/s.

The spread in the values of the parallel velocity components can be calculated using

$$dv_{\parallel} = \frac{dv}{1 + \tan\theta} \approx dv. \tag{5.2.3}$$

Using equation 2.6.15 the spread in the values of the parallel velocity components is calculated as

$$dv_{\parallel} = \frac{2\sigma}{\sqrt{1 + \tan\theta}} \approx 416\,\mathrm{m/s}. \tag{5.2.4}$$

We now want to approximate the velocity component perpendicular to the beam, $v_{\perp}$, in one Cartesian direction. The angular spread of the atom's movement is symmetric around $\theta = 0$, therefore the velocity distribution must be symmetric around $v = 0$ m/s and the average velocity is $\bar{v} = 0$ m/s.

Due to the small angular spread in the effusive beam after skimming the density distribution can be considered a uniform disk with a radius $R = D\tan\theta_{max}$, where D is the distance from the source to the laser beam and θ_{max} the maximum angular spread of the beam. The number of atoms with a velocity vector at angle θ must be proportional to the area of a thin slice through the disk,

$$N \propto \cos\left(\theta\frac{\pi}{\theta_{max}}\right).$$

This implies that $N \propto 1$ at $\theta = 0$, $N \propto 0$ at $\theta = \theta_{max}$, and N reaches its half value at $\theta = \frac{\theta_{max}}{2}$. For this reason we can approximate the spread in the velocity along one Cartesian direction as

$$2 \left(\bar{v}_\perp \left(\frac{\theta_{max}}{2} \right) + \frac{dv_\perp \left(\frac{\theta_{max}}{2} \right)}{2} \right), \tag{5.2.5}$$

where $\bar{v}_\perp \left(\frac{\theta_{max}}{2} \right)$ is the transverse velocity component at $\theta = \frac{\theta_{max}}{2}$ and $\frac{dv_\perp \left(\frac{\theta_{max}}{2} \right)}{2}$ is the variance in $\bar{v}_\perp$ at the same angle. Equations 2.6.14 and 2.6.16 can be used to calculate $\bar{v}_\perp$ and $dv_\perp$. This results in a transverse velocity spread of

$$2 \left(\bar{v}_\perp \left(\frac{\theta_{max}}{2} \right) + \frac{dv_\perp \left(\frac{\theta_{max}}{2} \right)}{2} \right)$$
$$= 2 \left(8.7 + \frac{6.5}{2} \right)$$
$$\approx 24 \, \text{m/s} \tag{5.2.6}$$

The density of the tin atoms at the laser beam can be estimated using 2.6.18.

$$n(R, \theta) = \frac{n_0 \cos \theta}{4\pi R^2} \, dA \approx 10^{14},$$

where R is a distance of 0.05 m from the source to the laser beam, $\theta \approx 0$, dA was used as 2×10^{-3} m^2, calculated from an aperture with a 0.5 mm diameter (the inner diameter of the hypodermic needle). The value of $n_0 \approx 10^{19}$ was calculated using equation 2.6.2, with the Sn vapour pressure at 1.33×10^{-1} Pa at a temperature of 1350 K.

The assumption is made that all the irradiated atoms are ionized, therefore the density of the ions will be the same as the density of the atoms. The irradiated volume can be estimated as

$$V = \pi r^2 h$$

where r is the laser beam radius of 0.5 mm and h the atomic beam width. The beam width was estimated to be 4 mm at the laser beam position. The number of ions created will then be

$$N_{ions} = nV = (10^{14})(3 \times 10^{-9}) \approx 300000.$$

The number of ions per isotope is estimated to agree with their natural abundances.

$$N_{116} = 0.1453 N_{ions} \approx 43590,$$
$$N_{118} = 0.2422 N_{ions} \approx 72660,$$
$$N_{120} = 0.3259 N_{ions} \approx 97770.$$

Using these values the beam current density, J, can be calculated. J was defined in equation 4.0.1 in the previous Chapter.

5.2.2 Supersonic Gas jet

For the jet source, tin atoms are seeded into a jet formed by argon gas. The average speed of argon in a gas jet is given by equation 2.6.28. The average forward speed is then determined for argon

$$\bar{v} = \sqrt{\frac{5k_B T_0}{m_{Ar}}} = 560\,\text{m/s}, \tag{5.2.7}$$

where $T_0 = 300$ K.

The assumption is then made that the heavier tin atoms will be accelerated to velocities close to that of the argon atoms in the jet. Therefore the average velocity of the tin atoms in the jet is

$$\bar{v}_{120} = \bar{v}_{118} = \bar{v}_{116} \approx 560\,\text{m/s}. \tag{5.2.8}$$

The effective Mach number, defined in Chapter 2.6.2, in terms of the nozzle diameter can be calculated using equation 2.6.23:

$$M_{eff}(x) = 3.26 \left(\frac{x}{D}\right)^{0.67} \approx 61.4. \tag{5.2.9}$$

Where $x = 16$ cm is the distance from the nozzle of the jet to the laser spot and $D = 0.2$ cm is the nozzle diameter. To calculate σ, the temperature of the jet at the laser beam spot had to be calculated. The temperature of the atoms in the jet is related to the effective Mach number through equation 2.6.24.

$$T = T_0 \left[1 + \left(\frac{\gamma - 1}{2}\right) M_{eff}^2\right]^{-1} \approx 238\,\text{mK}. \tag{5.2.10}$$

The temperature of the jet will be higher than this in practice due to experimental limitations, but temperatures of a few Kelvin is readily achievable in a gas jet. For the simulations the value of 30 K was used.

The angle θ has been estimated from the setup illustrated in Figure 3.6 to be $\theta_{max} \approx 0.3°$. The spread in the velocities can be determined using equation 2.6.15:

$$d\bar{v}_\parallel = \frac{2\sigma}{\sqrt{1 + (tan\theta)^2}} \approx 60\,\text{m/s} \tag{5.2.11}$$

where $\theta = \frac{\theta_{max}}{2}$ and σ was determined using equation 2.6.17

$$\sigma = \sqrt{\frac{k_B T}{m}} \sqrt{\frac{3\pi - 8}{\pi}} \approx 30\,\text{m/s}. \tag{5.2.12}$$

The transverse velocity spread can be determined following the same argument as for the effusive beam. The spread in the transverse velocity component along one cartesian direction is then determined as

$$
\begin{aligned}
2 & \left(\bar{v}_\perp \left(\frac{\theta_{max}}{2} \right) + \frac{dv_\perp \left(\frac{\theta_{max}}{2} \right)}{2} \right) \\
& = 2 \left(1.5 + \frac{0.16}{2} \right) \\
& \approx 3.2 \, \text{m/s},
\end{aligned}
\tag{5.2.13}
$$

where $\bar{v}_\perp$ and $dv_\perp$ were calculated using equations 2.6.14 and 2.6.16, respectively.

It is difficult to estimate the density of Sn in the Ar jet. The Sn density will depend on the efficiency of the laser ablation process. The Sn density calculation has been omitted.

5.3   Time of flight mass spectrometer simulations

IBSimu was used to simulate the flight of three different isotopes of tin through ToF-MS instrument. The three isotopes used are ^{116}Sn, ^{118}Sn, and ^{120}Sn as these are the most abundant stable isotopes of tin, as listed in Table 2.1. The flight times of the isotopes will always be the shortest for ^{116}Sn and longest for ^{120}Sn. The parameters used to introduce the isotopes were provided using the format provided in the previous section Listing 4.4. The typical beam parameters used in the simulations are summed up in Table 5.1. These values will be used for most of the simulations unless otherwise stated.

The following investigations were performed via simulation:

- Definition of the mass resolution.

- Influence of the size of the ionization volume.

- Influence of the velocity.

- Impact of the reflectron.

- Influence of the intermediate electrode of the reflectron.

- Comparison between an effusive atomic and a supersonic gas jet.

Table 5.1: Summary of typical parameter values used in the simulations.

Parameter	^{116}Sn	^{118}Sn	^{120}Sn
N	43590	72660	97770
m (atomic mass units)	116	118	120
q (electron charge)	1	1	1
Ion beam radius (m)	0.0005		
Centre of sample disk, c (m)	(0.0, 0.009, 0.00)		
Voltage on the reflector (V)	2000		
Voltage on the intermediate electrode (V)	1000		
Voltages on the ionization region electrodes (V)	2000		
	1600		
	900		
Effusive beam as a sample			
v (m/s)	580		
$dv_\parallel$ (m/s)	416		
$dv_\perp$ (m/s)	24		
J (C s^{-1} m^{-2})	1.3×10^{-3}	2.2×10^{-3}	3.0×10^{-3}
Seeded supersonic jet as sample			
v (m/s)	560		
$dv_\parallel$ (m/s)	60		
$dv_\perp$ (m/s)	3.2		
J (C s^{-1} m^{-2})	1.3×10^{-3}	2.2×10^{-3}	3.0×10^{-3}

5.3.1   Definition of the mass resolution

Figure 5.5 shows a typical time-binned histogram of data acquired at the position of the detector. The typical parameter values listed in Table 5.1 for the effusive atomic beam has been used. The ratio, $\frac{D}{d}$, where d is the averaged FWHM of the peaks in the mass spectrum and D the averaged distance between the centre of two neighbouring peaks is considered to be a measure of the resolution of the spectrum. The time axis in a mass spectrum such as the one shown in Figure 5.5 can be calibrated to represent the mass. To do this, the mass of the ions as a function of time can be plotted. The resulting graph can be fitted with a straight line (see Figure 5.6).

The straight line function can then be used to convert the time axis into a mass axis. Figure 5.7 shows a calibrated mass spectrum. It is important to note that the ratio $\frac{D}{d}$ does not change when the calibration of the time axis is

performed. In both Figures 5.5 and 5.7 the ratio $\frac{D}{d}$ stays the same at 15.
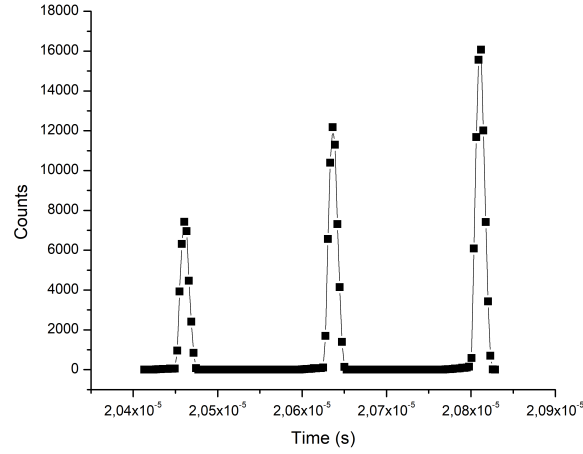
Figure 5.5:   The mass spectrum of three tin isotopes (^{116}Sn, ^{118}Sn, and ^{120}Sn from shorter to longer flight times) produced by the IBSimu simulation after passing through the reflectron. The beam was defined to have a radius of 0.0005 m and an initial speed distribution of $v_x = v_y = 24$ m/s perpendicular to the incident beam, and a speed distribution of $v_z = 416$ m/s parallel to the incident beam. The data were taken at the detector position. The ratio: $\frac{D}{d} \approx 15$.
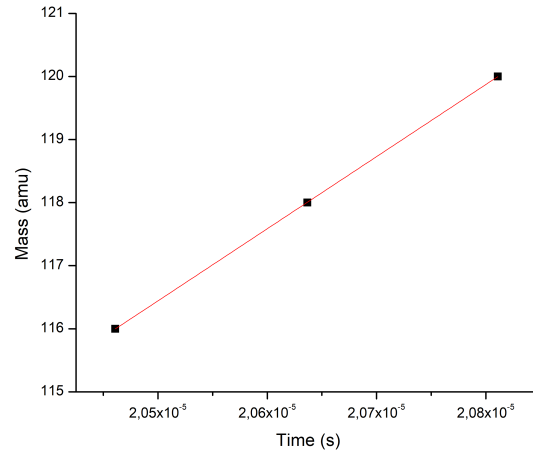
Figure 5.6:   The calibration curve between the mass and arrival time of the three tin isotopes (^{116}Sn, ^{118}Sn, and ^{120}Sn) produced from the IBSimu simulation data.
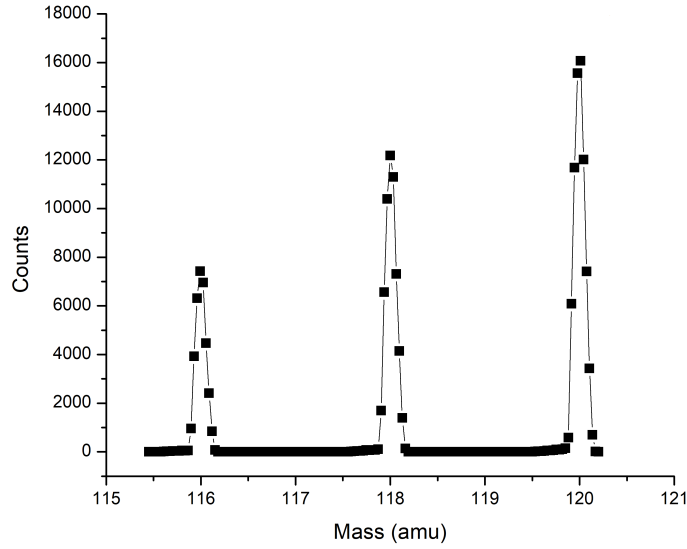
Figure 5.7:   The calibrated mass spectrum of three tin isotopes (^{116}Sn, ^{118}Sn, and ^{120}Sn from shorter to longer flight times) produced by the IBSimu simulation after passing through the reflectron. The beam was defined to have a radius of 0.0005 m and an initial speed distribution of $v_x = v_y = 24$ m/s perpendicular to the incident beam, and a speed distribution of $v_z = 416$ m/s parallel to the incident beam. The data were taken at the detector position. The ratio: $\frac{D}{d} \approx 15$.

Simulations were run to investigate the relationship between the ratio $\frac{D}{d}$ and ion mass. Ion beams were defined consisting of different pairs of masses, namely masses of 2 and 3 amu, 50 and 51 amu, 100 and 101 amu, 150 and 151 amu, and 200 and 201 amu. The mass spectra for these pairs were analyzed and the ratio $\frac{D}{d}$ for each pair was determined. The ratio $\frac{D}{d}$ was plotted as a function of mass in Figure 5.8.

From Figure 5.8, it is clear to see that $\frac{D}{d}$ decreases almost exponentially as the mass increases. It becomes more difficult to separate ions with a mass difference of 1 amu temporally as the mass becomes larger.

The IUPAC definition of the resolution of a mass spectrum is defined as

$$R = \frac{m}{dm}, \tag{5.3.1}$$

where dm is the smallest mass difference that can be resolved and m the observed mass. Different definitions of dm exist, for our purposes dm will be used as the 50% peak width or the FWHM of the peak and m as the time at the centre of the peak.
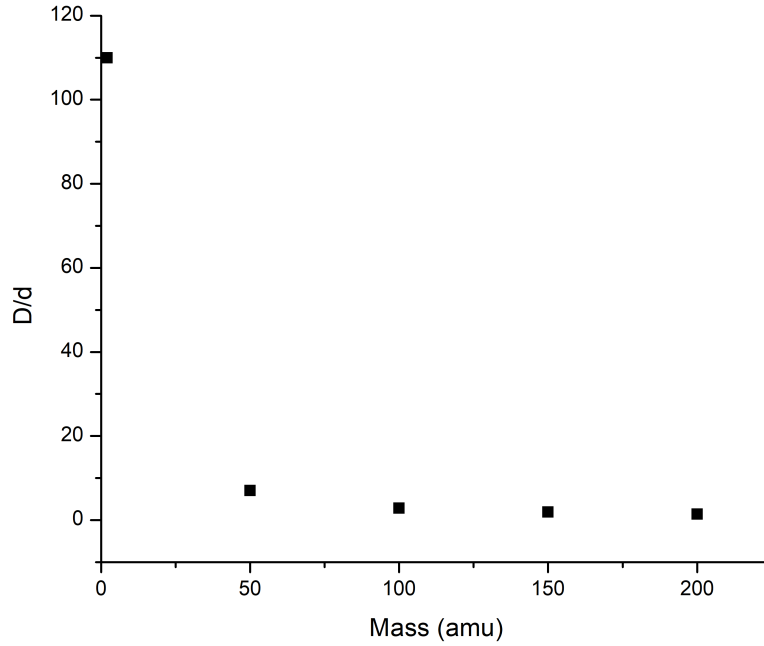
Figure 5.8: The ratio $\frac{D}{d}$ for different mass pairs have been plotted as a function of mass. The mass pairs that have been used are 2 and 3 amu, 50 and 51 amu, 100 and 101 amu, 150 and 151 amu, and 200 and 201 amu.

The same mass pairs as mentioned previously have been used to determine $\frac{m}{dm}$ as a function of mass. Figure 5.9 represents the resolution, $\frac{m}{dm}$, for each mass as a function of mass. The resolution fluctuates between $R = 560$ and $R = 580$, for ions beams with the same initial conditions. Therefore $\frac{m}{dm} = 570$ will be considered the resolution of our instrument.

For the purposes of following simulations we will be using $\frac{D}{d}$ to quantify the ability of the instrument to seperate the peaks of ^{116}Sn, ^{118}Sn, and ^{120}Sn. This is a convenient measure as the FWHM and the centre of the peak is directly obtained through analysis of the mass spectra produced by the simulation.

5.3.2   Influence of the size of the initial volume of ions

The beam parameters were kept the same as summarized in Table 5.1 for supersonic jet sources. The radius of the incident atomic beam was changed. The beam radius was changed between 0.125 mm, 0.250 mm, 0.500 mm, 1.000 mm, and 2.000 mm. For each of these values the ions travelling through the instrument were simulated and data acquired at the position of the detector. Two types of simulations were set up for each beam radius. The simulations
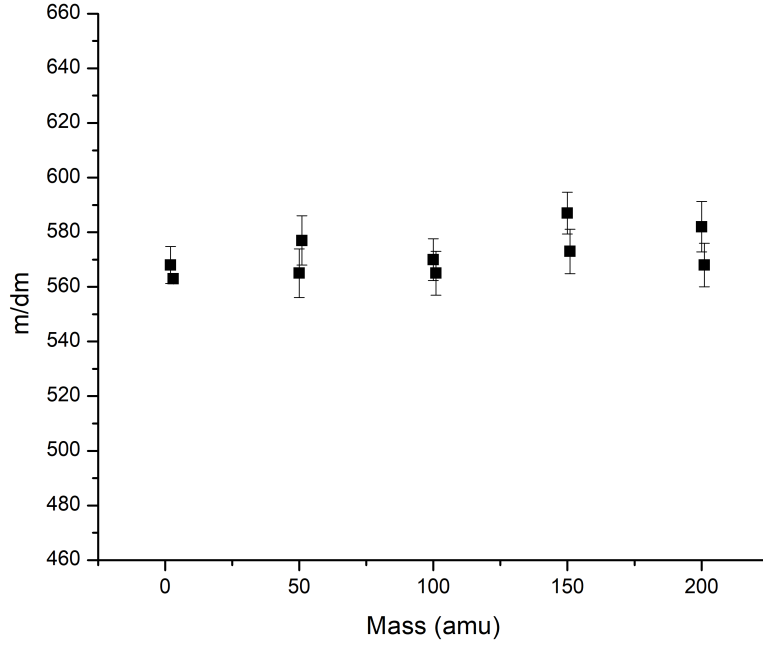
Figure 5.9: The resolution $\frac{m}{dm}$ for different mass pairs have been plotted as a function of mass. The mass pairs that have been used are 2 and 3 amu, 50 and 51 amu, 100 and 101 amu, 150 and 151 amu, and 200 and 201 amu.

were set to include and exclude the space charge effects. The space charge effect is calculated in the simulation based on the current density value of J. The relation between J and the beam radius is given by equation 4.0.1, therefore $J \propto \frac{1}{r^2 h}$ where $h = 0.004$ m was used. The other parameter values were used as given in Table 5.1. If the value of J is set to zero in the simulation the space charge effects are neglected without changing the other parameters.

d as a measure of the FWHM of the peaks has been plotted as a function of beam radius (See Figure 5.10). From the graph in Figure 5.10, we see that the d increases as the beam radius of the incident atomic beam in the simulation increases. This implies that the time resolution of the spectra worsens as the beam radius increase. For both cases, including and excluding space charge effects, the resolution decreases as the beam radius increases. The resolution of the spectra with no space charge effects is slightly better when compared to the spectra including space charge effects.

It was expected that in the absence of any space charge effects, d would decrease almost linearly as the beam radius increases. The space charge effects should become more prominent as the radius of the beam gets smaller, thereby
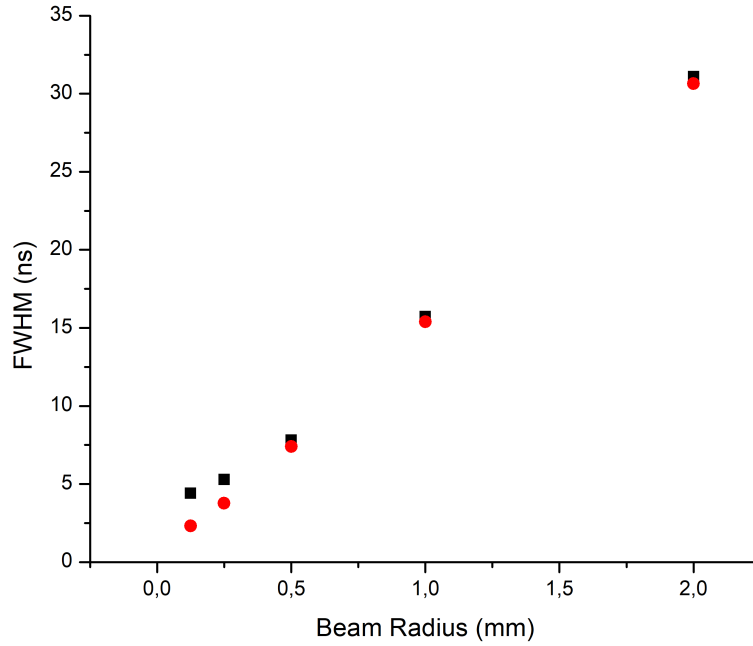
Figure 5.10: The FWHM of the mass spectrum as a function of incident atomic beam radius. The black data points are from spectra with space charge effects (based on the beam current density, J) taken into account. The red data points are from spectra simulated without space charge effects. The error bars are smaller than the data points.

reducing the resolution. The near linear decrease in the FWHM as the beam radius decreases can be seen from the red data points in Figure 5.10. The space charge effects can be observed when the beam radius is smaller than 0.500 mm, the FWHM is bigger for the simulated mass peaks when beam radii of 0.250 mm and 0.125 mm are used.

In the actual experiment the beam radius will be determined by the spot size of the laser. From these results, it is favourable to select a laser spot size that is small, to ensure a good time resolution in the mass spectra, however it should be noted that space charge effects can start reducing the resolution if the density of ions in the initial volume becomes too large.

For the rest of the simulations, an atomic beam radius of 0.500 mm will be used. This spot size is easily achievable in the planned experimental setup.

5.3.3   Influence of the speed distribution on the mass spectrum

The influence of the speed distribution of the atoms entering the ToF-MS has been investigated. The beam parameters used in the simulation will be kept constant, as summarized in Table 5.1 for supersonic gas jets, with the exception of the transverse and parallel velocity distributions. For the first simulation the velocity distribution will be present, while in the second simulation the velocity distribution will be set to $dv_\parallel = dv_\perp = 0$.

Figure 5.11:   The mass spectrum of three tin isotopes (^{116}Sn, ^{118}Sn, and ^{120}Sn from shorter to longer flight times) produced by the IBSimu simulation after passing through the reflectron. The beam was defined to have an initial speed distribution of $v_x = v_y = 3$ m/s perpendicular to the incident beam, and a speed distribution of $v_z = 10$ m/s parallel to the incident beam. The data were taken at the detector position. The ratio: $\frac{D}{d} \approx 22$.

While the spectra look similar, the FWHM of the peaks in spectra are different. The FWHM for the peaks in the spectra produced for a jet with initial speed distributions $dv_\parallel = dv_\perp = 0$ m/s reduced by $\sim 10\%$ for the three different isotopes, when compared to the corresponding peaks in the spectra produced for

Table 5.2: Data extracted for a tin seeded supersonic gas jet with initial speed distributions $dv_\parallel = 10$ m/s and $dv_\perp = 3$ m/s.

Isotope	Centre of peak [μs]	FWHM [μs]
116	20.5	7.84×10^{-3}
118	20.6	7.91×10^{-3}
120	20.8	7.97×10^{-3}

Table 5.3: Data extracted from mass spectrum for a supersonic jet source with initial speed distributions $dv_\parallel = dv_\perp = 0$ m/s.

Isotope	Centre of peak [μs]	FWHM [μs]
116	20.5	7.06×10^{-3}
118	20.6	7.11×10^{-3}
120	20.8	7.14×10^{-3}

a supersonic gas jet with initial speed distributions $dv_\parallel = 10$ and $dv_\perp = 3\,\mathrm{m/s}$.

Assuming that the transverse and parallel speed distribution of atoms in the effusive beam is zero, is not feasible from an experimental stand point. The results above indicate that the peak widths can be significantly influenced by the speed distribution of the ions. This highlights the importance of proper collimation of the atomic beam as it enters the ToF-MS. By properly collimating the beam, the transverse velocity components of the atoms in the jet can be limited, which in turn will help narrow the mass peaks in the measured mass spectra.

It is important to note that in the actual experiment the resolution of the mass spectra is limited by the duration of the incident laser pulses (~ 10 ns) as well as the speed of the detector.

5.3.4   Impact of the reflectron on the mass spectrum

Another important aspect to investigate when it comes to the ToF-MS is the influence the reflectron has. The following results were obtained for supersonic gas jet seeded with three different isotopes of tin. The simulations used an supersonic jet with a beam radius of 0.0005 m and 1000 V potential applied to the intermediate electrode of the reflectron. Flight time spectra (time binned histograms) were obtained at three different positions (i) at the spatial focus, (ii) just before the reflectron, and (iii) at the position of the detector after the reflectron. The spatial focus, defined in Chapter 2.5.2, is a special spot within the field free drift region where the ions are bunched together. The

time-binned histograms are presented in Figures 5.12, 5.13, and 5.14.

The spatial focus can be calculated using equation 2.5.24,

$$\gamma = \frac{3x_{SF}}{x_{SF} - 2x_{A2}}.$$

The equation can be written in terms of the spatial focus, x_{SF}, as

$$x_{SF} = \frac{2\gamma}{\gamma - 3} x_{A2}, \tag{5.3.2}$$

where γ is the ratio between U and U_{A1} and x_{A2} is the length of the second acceleration region (see Figure 3.1). The extractor grid of the ionization region was used as the separator between the first and second acceleration region. Therefore the potentials are $U = 1800$ V and $U_{A1} = 200$ V, resulting in $\gamma = 9$. The length of the second acceleration region is 21.5 mm. This region stretches from the extractor grid to grounded electrode. The spatial focus is then determined as

$$\begin{aligned}
x_{SF} &= \frac{2\gamma}{\gamma - 3} x_{A2} \\
&= \left(\frac{2(9)}{9 - 3} \right) (21.5) \\
&= 64.5 \, mm \tag{5.3.3}
\end{aligned}$$

The spatial focus is located 64.5 mm from the grounded electrode of the ionization region.

The effect of spatial focus is illustrated by comparing Figures 5.12 and 5.13. In both cases the data were taken before reaching the reflectron, but Figure 5.12 represents the flight times at the spatial focus at 0.0645 m, whereas Figure 5.13 represents the flight times 0.3555 m further at 0.42 m. At the spatial focus the peaks of the isotopes are clearly resolved whereas at 0.42 m the temporal spread of the three ions start to overlap, resulting in one broadened peak. The spatial focus is the position where the ions produced closer to the back plate of the ionization region overtake ions starting from positions further from the back plate. It is possible since the former ions are accelerated to a larger kinetic energy. At the spatial focus the ions bunch together, therefore having a smaller temporal distribution since the initial spatial distribution has been compensated for. By the position of 0.42 m (Figure 5.13) the more energetic ions have passed the slower ions, increasing the temporal spread.
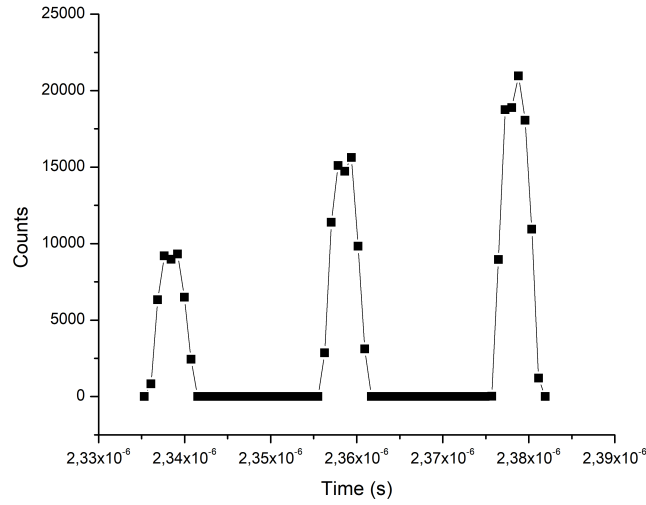
Figure 5.12: The mass spectrum of three tin isotopes (^{116}Sn, ^{118}Sn, and ^{120}Sn from shorter to longer flight times) produced by the IBSimu simulation before passing through the reflectron. The data were taken at the spatial focus, 64.5 mm from the last electrode of the ionization region. The ratio: $\frac{D}{d} \approx 6$.
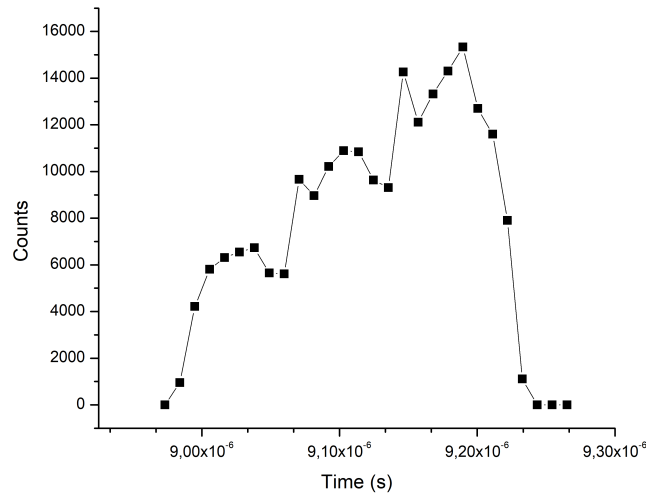
Figure 5.13: The mass spectrum of three tin isotopes (^{116}Sn, ^{118}Sn, and ^{120}Sn from shorter to longer flight times) produced by the IBSimu simulation just before passing through the reflectron. The data were taken 0.42 m from the last electrode in the ionization region, just before the reflectron. The separate mass peaks can not be resolved.

To determine the impact of the reflectron the data recorded at the spatial focus and at the detector position after the reflectron should be compared, since in the absence of a reflectron the detector would have been placed at the spatial focus of the ionization region.
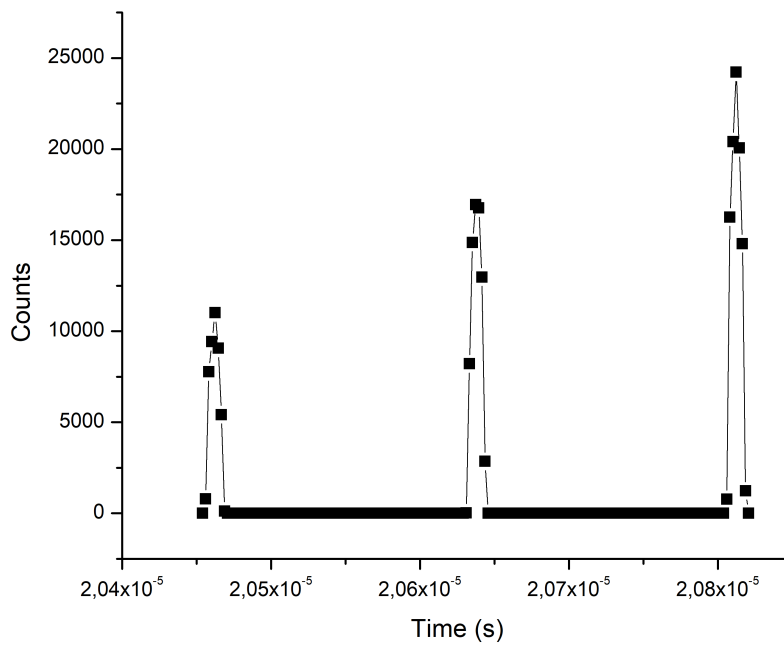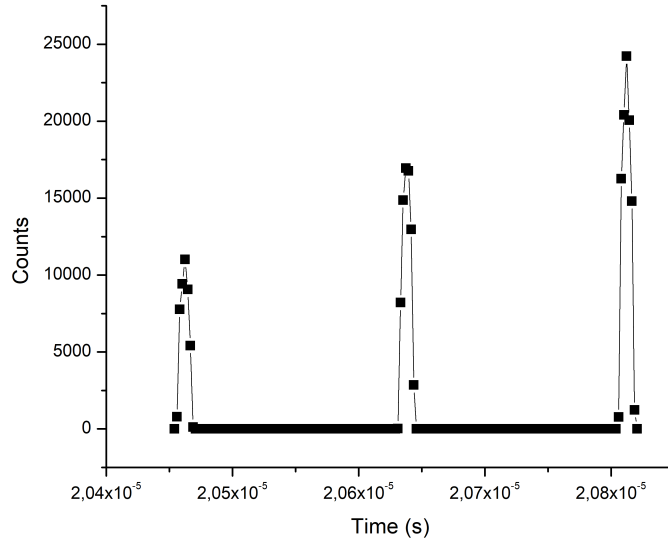

Figure 5.14: The mass spectrum of three tin isotopes (^{116}Sn, ^{118}Sn, and ^{120}Sn from shorter to longer flight times) produced by the IBSimu simulation after passing through the reflectron. The data were taken at position of the detector. The ratio: $\frac{D}{d} \approx 22$.

The data represented in Figures 5.12 and 5.14 were analysed to report the centre of the peak as well as the full-width at half-maximum (FWHM) for each peak. These values are reported in Table 5.4 for before and after the reflectron, respectively. The change in ratio $\frac{D}{d} = 6$ before the reflectron to $\frac{D}{d} = 22$ at the detector position is clear from Figures 5.12 and 5.14.

Table 5.4: Data extracted at the spatial focus and at the detector position

Isotope	At the spatial focus		At detector position	
	Centre of peak [μs]	FWHM [μs]	Centre of peak [μs]	FWHM [μs]
116	2.34	3.26×10^{-3}	20.5	7.84×10^{-3}
118	2.36	3.28×10^{-3}	20.6	7.91×10^{-3}
120	2.38	3.32×10^{-3}	20.8	7.97×10^{-3}

From the data gathered in Table 5.4 it becomes clear that the introduction of the reflectron improves the resolution of the ToF-MS. The peaks after the reflectron have been narrowed to a FWHM of ~ 7.9 ns. It is however important to note that the widths of these peaks in the spectra will be limited by the duration of the laser pulse. In the simulation all the ions are created at the same time, while in an actual experiment the ions are produced during the duration of the laser pulse, which is about 10 ns.

5.3.5   Influence of the intermediate electrode of the reflectron

The intermediate electrode that can be set to a chosen voltage is an advanced feature of the reflectron. According to the manufacturer the voltage on the intermediate electrode should be tuned to fine tune the shape of the mass peaks. We want to investigate this feature and its effects.

For this set of simulations the voltage applied to the intermediate electrode (see Figure 3.1) of the reflectron was changed. The applied voltage was changed between 800 V, 1000 V, and 1200 V. The resulting mass spectra have been plotted in Figures 5.15, 5.16, and 5.17.
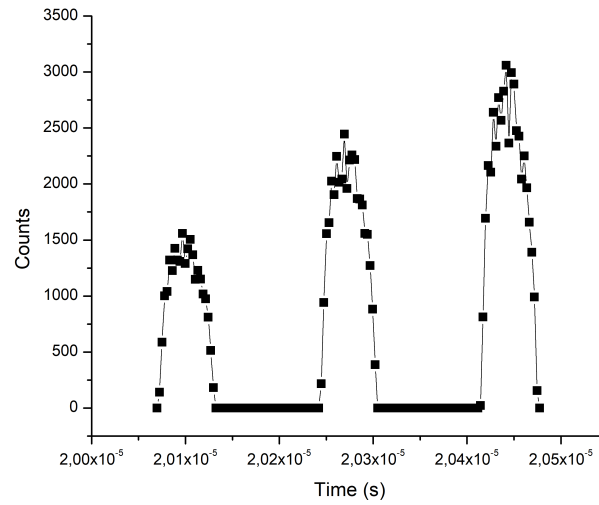
Figure 5.15: The mass spectrum of three tin isotopes (^{116}Sn, ^{118}Sn, and ^{120}Sn from shorter to longer flight times) produced by the IBSimu simulation for a reflectron with 800 V applied to the intermediate electrode. The data were taken at position of the detector. The ratio: $\frac{D}{d} \approx 4.2$.

Figure 5.16: The mass spectrum of three tin isotopes (^{116}Sn, ^{118}Sn, and ^{120}Sn from shorter to longer flight times) produced by the IBSimu simulation for a reflectron with 1000 V applied to the intermediate electrode. The data were taken at position of the detector. The ratio: $\frac{D}{d} \approx 22$.

Figure 5.17: The mass spectrum of three tin isotopes (^{116}Sn, ^{118}Sn, and ^{120}Sn from shorter to longer flight times) produced by the IBSimu simulation for a reflectron with 1200 V applied to the intermediate electrode. The data were taken at position of the detector. The ratio: $\frac{D}{d} \approx 3.7$.

The mass spectra have been analysed and the centre of the peaks and the FWHM are reported in Table 5.5.

Table 5.5: Data extracted from simulated flight time spectra showing the centre of the mass peaks and the FWHM of the peaks after passing through the reflectron for different voltages applied to the intermediate electrode.

Voltage applied:	800	900	1000	1100	1200
Isotope	Centre of peak $[\mu s]$				
116	20.1	20.3	20.5	20.7	21.0
118	20.3	20.5	20.6	20.9	21.2
120	20.4	20.6	20.8	21.1	21.3
Isotope	FWHM $[\mu s]$				
116	41.8×10^{-3}	27.8×10^{-3}	8.30×10^{-3}	15.3×10^{-3}	49.0×10^{-3}
118	41.7×10^{-3}	26.7×10^{-3}	8.46×10^{-3}	15.3×10^{-3}	49.3×10^{-3}
120	41.5×10^{-3}	27.5×10^{-3}	8.49×10^{-3}	15.5×10^{-3}	49.9×10^{-3}

From the data in Table 5.5 it is observed that the mass spectra peaks are narrowest for the case where 1000 V is applied to the intermediate electrode. It is expected that the spatial focus of the reflectron is located close to the detector position for the case where 1000 V is applied to the intermediate electrode. The data indicates that the a voltage between 1000 V and approximately 1100 V would give the narrowest peaks. To determine the optimal voltage to better accuracy either more simulations or an experimental investigation will be necessary.. At the spatial focus the ions are bunched together to reduce the temporal spread, and increase the resolution.

It is also clear that the flight times differ for the five cases. The flight times for ions are shorter when a lower voltage is applied to the intermediate electrode. To explain this phenomenon, the potential throughout the reflectron was extracted from the simulation. The potential on the y-axis of the reflectron has been plotted for 800 V, 1000 V, and 1200 V applied to the intermediate electrode in Figure 5.18.
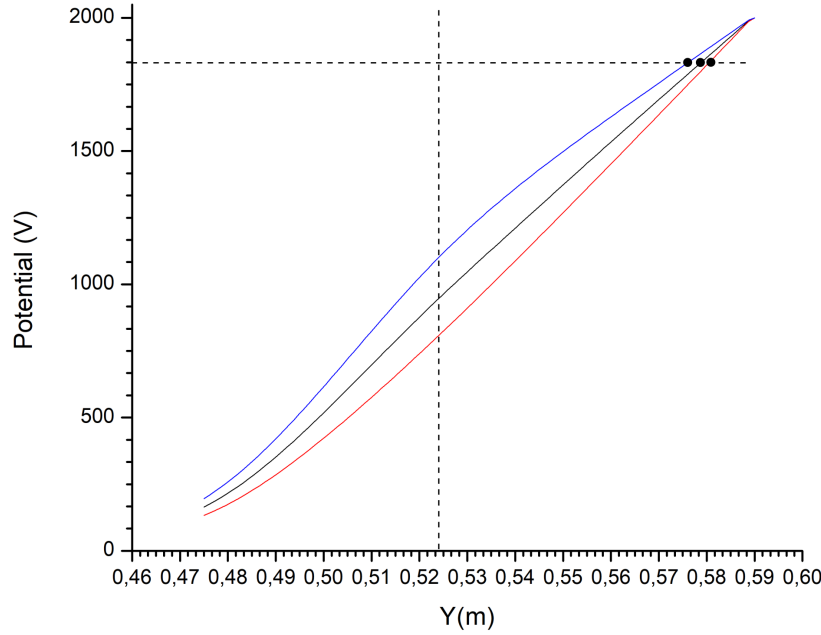
Figure 5.18: The potential (V) on the y-axis of the reflectron when 800 V (in red), 1000 V (in black), and 1200 V (in blue) is applied to the intermediate electrode. The vertical dashed line represents the position of the intermediate electrode along the y-axis. The horizontal dashed line represents the potential in the middle of the ionization region (1800 V). The turn-around point of the ions is marked with a black dot for each curve.

Figure 5.18 illustrates the potential along the y-axis of the reflectron. The horizontal dashed line has been inserted to illustrate the potential at the middle of the ionization region.

The total energy of the ions at their initial position in the middle of the ionization region is the sum of the potential energy U and the kinetic energy K.

$$E = U + K$$
$$= qV + \frac{1}{2}mv^2, \tag{5.3.4}$$

where q is the charge of the ion, V the potential acting on the ion, m the mass of the ion, and v the initial speed of the ion along the acceleration axis. The ions are generated in the middle of the ionization region where V = 1800 V, with a small speed along the acceleration axis. The total energy of the

Table 5.6: The percentage ions detected after passing through the reflectron for different voltages applied to the intermediate electrode.

Voltage applied:	800 V	1000 V	1200 V
Isotope	Ions detected (%)	Ions detected (%)	Ions detected (%)
116	54	100	100
118	51	100	100
120	48	100	100

generated ions is therefore given by

$$E = U + K \approx U = q(1800\,V),$$

as the kinetic energy is very small. For this reason the horizontal dashed line in Figure 5.18 represents the total energy of the ions in units of Joule per electron charge.

In the field-free region the ions have only kinetic energy. As the ions enter the potential field of the reflectron their kinetic energy decreases and potential energy increases. Therefore, the blue, black, and red curves in Figure 5.18 essentially represent the potential energy per electron charge of the ions. The distance between the dashed horizontal line and the coloured potential curves is related to the kinetic energy per electron charge of the ions. The smaller the distance, the lower the kinetic energy will be. The intersection between the potential curve and the horizontal dashed line is the turn-around position of the ions.

For all three simulations, the ions turn around at approximately the same depth in the reflectron. The turnaround points are located close to the reflector plate as marked by the dots in Figure 5.18. However, when the intermediate electrode is set to 1200 V the ions will have a lower kinetic energy for the time spent in the reflectron. This means the ions spend a longer time in the reflectron, contributing to the longer flight time.

It was also observed that when using an intermediate potential of 800 V a significant portion of the ions do not reach the detector position. This results in the peaks in Figure 5.15 having a lower amplitude when compared to the corresponding peaks in Figures 5.16 and 5.17. The percentage ions detected was calculated and the results have been reported in Table 5.6.

From these results it can be observed that $\sim 50\%$ of the ions are lost when a potential of 800 V is applied to the intermediate electrode. The loss of the ions can be clarified when looking at the equipotential lines of the reflectron.
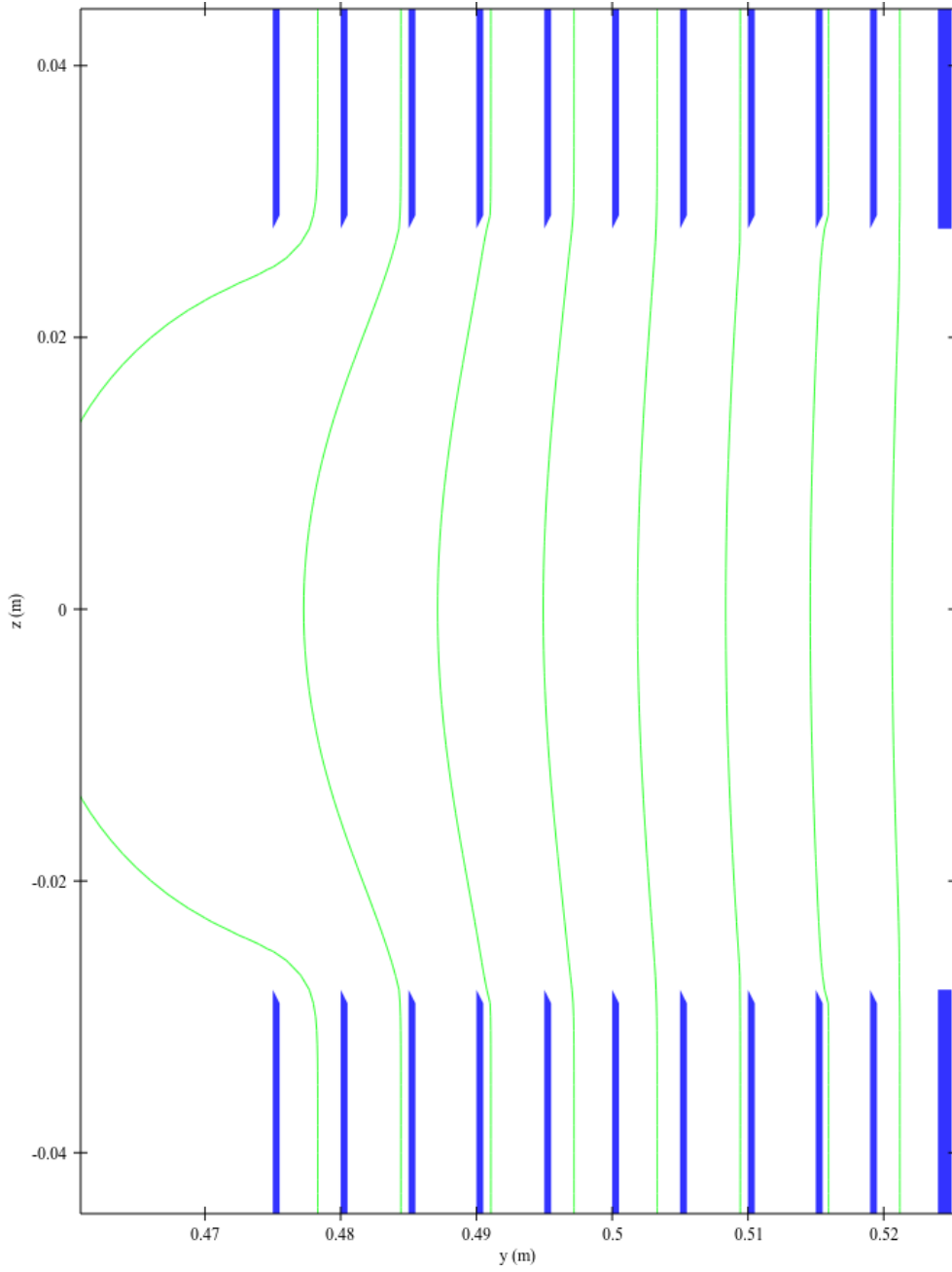
Figure 5.19: The front half of the reflectron up to the intermediate electrode as constructed using the IBSimu library. The equipotential lines are illustrate in green for the case of 800 V on the intermediate electrode (the right most electrode on the image).

In Figure 5.19 the reflectron and the present equipotential lines have been illustrated. During the simulations it was observed that the ions exit the reflectron at a slightly higher position along the z-axis when a potential of 800 V is applied to the intermediate electrode. The generated ions initially have a ve-

locity in the z-direction as this is the propagation direction of the atomic beam. Therefore ions enter the reflectron at a positive z-position, not at $z = 0$. The equipotential lines show that an ion moving along a line at $z > 0$ will experience a force $F_z = -\frac{dV}{dz}$ in the z-direction, and acquire an even larger velocity in the z-direction. This can cause the ions to miss the detector. This effect seems to be dominant in the 800 V case, probably due to the detail of the trajectory of the ions. In the experimental setup case this will be corrected by applying a static electric field in the $-z$-direction on the electrodes in the field free region.

From the results in this section it seems favourable to select a potential of 1000 V applied to the intermediate electrode. In the actual experiment the applied voltage should be fine tuned to achieve maximum resolution. The use of static electric fields to steer the ion beam, in particular in the direction parallel to the effusive beam will be necessary.

5.3.6   Comparison between an effusive atomic beam and a supersonic gas jet.

The two atom sources have been simulated and the resulting mass spectra were obtained through the simulation. The beam parameters that have been used are summarized in Table 5.1. As the Sn density in the supersonic jet could not be estimated, the same values of number of ions and current density were used in the supersonic jet as in the effusive beam.

The mass spectra obtained using the two different sources have been plotted in Figures 5.20 and 5.21. The peaks from Figures 5.20 and 5.21 were analyzed and the results are reported in Table 5.7. From the results it becomes clear that $\sim 30\%$ of the ions provided by the effusive atomic beam do not reach the detector. The effusive atomic beam provide the atoms with a higher speed distribution in the forward direction. This leads to ions missing the detector after travelling through the ToF-MS.

From the data in Table 5.7, it becomes clear that the mass peaks are broader for the ions generated from the effusive source due to the larger spread in $dv_\perp$ that functions as the initial velocity spread parallel to the direction of the acceleration. This leads to the change in $\frac{D}{d}$ that was indicated in Figures 5.20 and 5.21.

The mass peaks in Figure 5.21 will be broadened in an actual experiment. The FWHM of the peaks in the spectrum provided through the simulation is below the ~ 10 ns laser pulse duration.
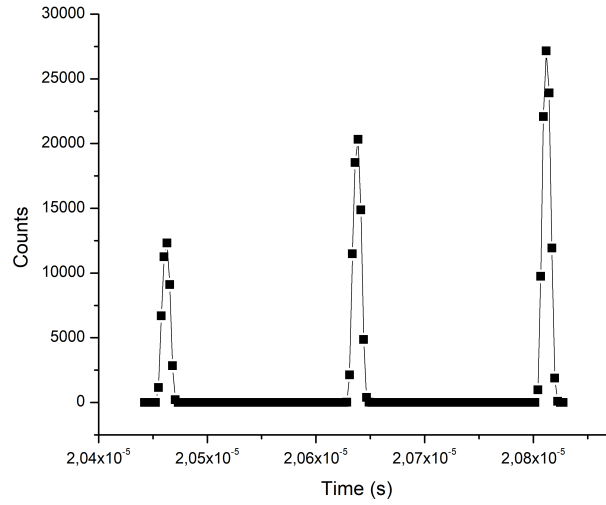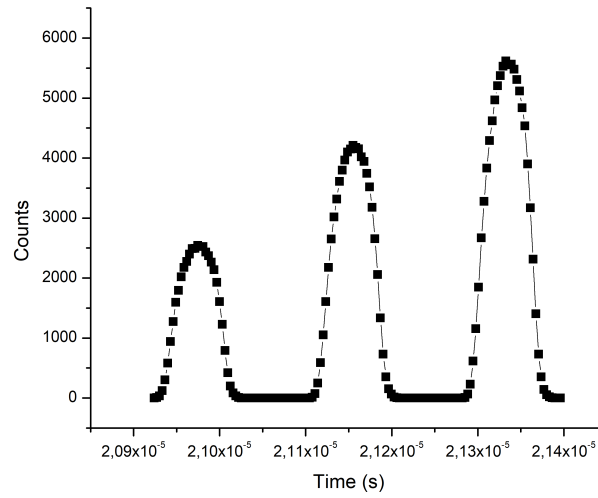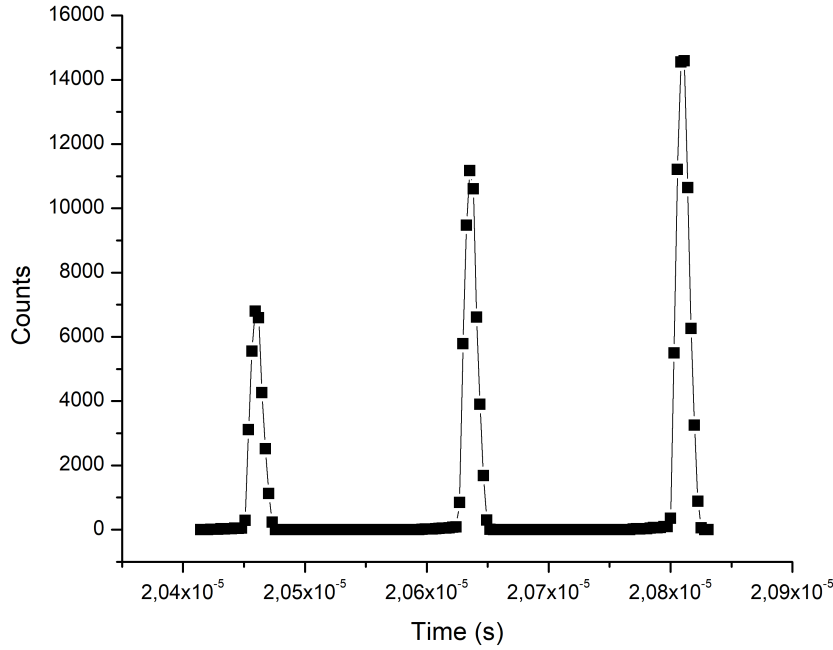
Figure 5.20: The mass spectrum of three tin isotopes (^{116}Sn, ^{118}Sn, and ^{120}Sn from shorter to longer flight times) produced by the IBSimu simulation after passing through the reflectron. An effusive atom source was used to introduce the atoms into the ToF-MS. The data were taken at the detector position. The ratio: $\frac{D}{d} \approx 15$.

Table 5.7: Data extracted from Figures 5.20 and 5.21 showing the centre of the mass peaks, the FWHM of the peaks, and the % ions detected after passing through the reflectron.

Isotope	Effusive beam			Supersonic jet		
	Centre of peak [μs]	FWHM [μs]	Ions Detected (%)	Centre of peak [μs]	FWHM [μs]	Ions Detected (%)
116	20.5	11.4×10^{-3}	70.5	20.5	7.84×10^{-3}	100
118	20.6	11.5×10^{-3}	69.9	20.6	7.91×10^{-3}	100
120	20.8	11.6×10^{-3}	69.4	20.8	7.97×10^{-3}	100

The peak widths (FWHM in Table 5.7) are of the same order for both the effusive atomic beam and the supersonic gas jet according to the ToF-MS simulation. In both cases the Sn isotopes are well resolved. The resolution is therefore not the main consideration for the choice of the atom source.

In general the atomic beam has the advantage that it is easier to implement as no additional synchronized laser is required to ablate the sample. For the su-
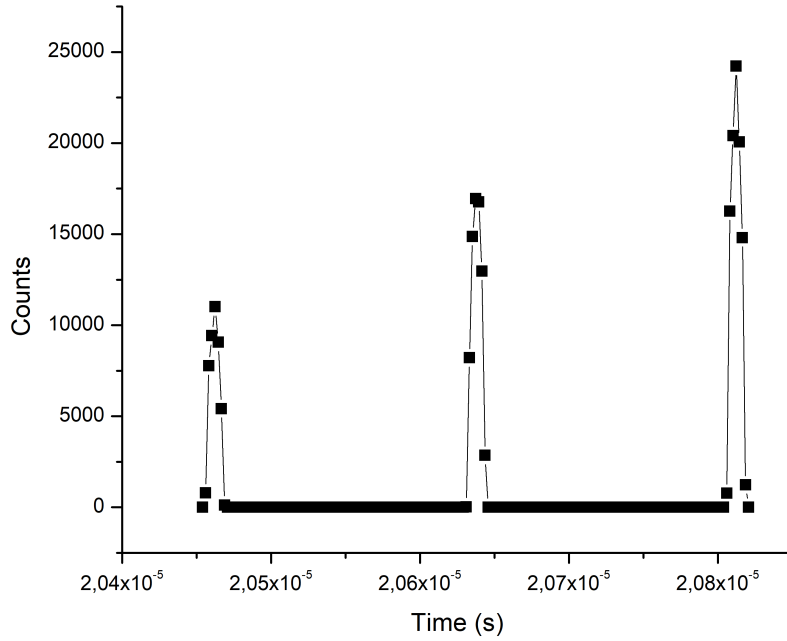
Figure 5.21:   The mass spectrum of three tin isotopes (^{116}Sn, ^{118}Sn, and ^{120}Sn from shorter to longer flight times) produced by the IBSimu simulation after passing through the reflectron. A supersonic jet source was used to introduce the atoms into the ToF-MS. The data were taken at the detector position. The ratio: is $\frac{D}{d} \approx 22$.

personic jet source the timing between the pulsed valve, the ablation laser and the ionizing laser light has to be fine tuned. This timing problem is avoided when using an effusive source. However the Doppler broadening of the spectral lines of the atoms may limit the feasibility to selectively ionize particular isotopes by resonance ionization. If Doppler broadening in the effusive beam is larger than the spectral isotope shift then isotope selective ionization is impossible, even if a laser with a bandwidth smaller than the isotope shifts is available.

The supersonic jet is therefore a more attractive option. The Doppler broadening for a supersonic jet is smaller compared to an effusive source. For the supersonic jet source, the laser bandwidth is most probably the limiting factor for selective ionization.

The Doppler widths for both sources can be calculated by starting with the

one dimensional velocity probability distribution:

$$f(\upsilon) = \sqrt{\frac{m}{2\pi k_B T}} \, exp\left\{\frac{-m\upsilon^2}{2k_B T}\right\}, \tag{5.3.5}$$

where υ is the velocity, k_B the Boltzmann constant, T the temperature, and m the mass. Through the Doppler effect the Doppler broadened line shape as a function of the angular frequency, ω, is then given as

$$S(\omega) = \frac{c}{\omega_0}\sqrt{\frac{m}{2\pi k_B T}} \, exp\left\{\frac{-m\left[\frac{c}{\omega_0}(\omega - \omega_0)\right]^2}{2k_B T}\right\}, \tag{5.3.6}$$

where ω_0 is the central frequency, ω the Doppler shift in the angular frequency, and c is the speed of light.

The Doppler broadened line shape has a Gaussian shape. The standard deviation, σ, of the Gaussian is defined as the square root and the variance. The standard deviation is defined as

$$\sigma = \frac{\omega_0}{c}\sqrt{\frac{k_B T}{m}}. \tag{5.3.7}$$

The FWHM of the Doppler broadened line can be determined by using the standard deviation defined in equation 5.3.7.

$$FWHM = \sigma\sqrt{8ln2} = \frac{\omega_0}{c}\sqrt{\frac{k_B T}{m}}\sqrt{8ln2}. \tag{5.3.8}$$

In terms of wavelength this becomes

$$FWHM = \frac{\lambda_0}{c}\sqrt{\frac{k_B T}{m}}\sqrt{8ln2}, \tag{5.3.9}$$

where λ_0 is the central wavelength.

Resonance ionization schemes were identified from literature and listed in Table 2.4 and the isotope shifts for the 286.3 nm line relative to ^{120}Sn are listed in Table 2.5. The Doppler widths for the 286.3 nm line for the effusive source and the supersonic jet can be calculated using equation 5.3.9. The results have been reported in Table 5.8.

From these results we see that the Doppler broadening is larger in the effusive atomic beam. In the effusive beam the Doppler broadening is of the same order of magnitude as the isotope shifts of the stable Sn isotopes (listed in Table 2.5) into one. Therefore selective excitation and subsequent ionization will be harder to achieve. With the current laser (Bandwidth $\approx 4 \times 10^{-2}$ cm^{-1}

Table 5.8: Doppler broadened linewidths in the supersonic jet and the effusive beam.

Atom Source	$\Delta\lambda$ in nm	$\Delta\frac{1}{\lambda}$ in cm^{-1}
Supersonic jet	1.14×10^{-5}	1.40×10^{-3}
Effusive beam	3.02×10^{-6}	3.68×10^{-4}

Table 5.9: Bandwidths of available pulsed dye laser in comparison to a state of the art narrowband pulsed laser.

Laser type	$\Delta\nu$ in Hz	$\Delta\frac{1}{\lambda}$ in cm^{-1}
Pulsed dye laser	1.2×10^9	40×10^{-3}
State of the art narrowband laser	1.0×10^5	3×10^{-3}

as listed in Table 5.9) one can probably excite all the Sn isotopes at the same time. This will make the Sn isotopes a good test for the resolution and sensitivity of the ToF-MS.

The Doppler broadened linewidth for the supersonic gas source is narrower than the optical isotope shifts listed in Table 2.5. If combined with a state of the art narrowband laser (for example a continuous wave dye laser with a pulsed amplifier) with a bandwidth of 3×10^{-3} cm^{-1} then selective excitation would be possible.

The Doppler broadening presents a problem when selective ionization is the goal. To counteract the problem of Doppler broadening, Doppler-free excitation techniques can be used. Two-photon absorption from counter propagating laser beams may be used to reduce Doppler broadening, especially in the effusive beam [82; 83].

Initial experiments will make use of the effusive atomic beam. As mentioned earlier, this method is easier to implement than the supersonic jet. The effusive beam method will be used to optimize the resonance ionization technique and investigate the Doppler-free technique. Subsequently, the change will be made to a seeded jet setup.

Chapter 6

Summary and Future work

6.1   Summary

Literature has been studied on the nuclear shell model and how the tin (Sn) nucleus can be used to test this model. It was reported how laser spectroscopy can be used to obtain information concerning the nucleus. The nuclear spin, nuclear moments, and changes in the nuclear charge radii can be extracted using laser spectroscopy. These parameters provide insight into the structure of the nucleus and can be used to update nuclear models.

From literature suitable resonance ionization spectroscopy (RIS) schemes have been identified and reported. A laser system was designed and set up to provide the required wavelength light. The frequency doubling of one of the beams was optimized and synchronized with the laser wavelength while tuning.

A time-of-flight mass spectrometer ToF-MS will be used to detect the ionized Sn. Before the ToF-MS can be used Sn sources had to be designed and manufactured.

Two different experimental setups have been designed and manufactured to produce Sn atoms and introduce it into ToF-MS. In both setups the atoms will enter the ToF-MS orthogonal to the acceleration axis of the instrument. This reduces the velocity spread of the sample along the acceleration axis of ToF-MS. The incident laser light will be orthogonal to the forward direction of the atomic beam, which in turn will reduce the Doppler broadening in the sample. The first setup is to produce an effusive beam of Sn atoms. The Sn sample will be resistively heated and allowed to effuse through skimmers into the ionization region of the ToF-MS. The second setup has been designed to produce a Sn seeded gas jet. This setup consists of a separate vacuum chamber that will be attached onto the ToF-MS. The tin sample will be placed in a housing in this chamber and a Nd:YAG laser will be used to ablate the sample.

100

The ablated Sn atoms will be seeded into an argon jet. The jet will be directed into the ToF-MS. The design of both of these setups have been highlighted in Chapter 3.

The properties of the effusive source as well as the supersonic gas jet have been calculated and reported in Chapter 5.2. The two atomic beam sources will provide Sn atoms with average speeds of 580 m/s for the effusive source and 560 m/s for the supersonic jet source. While the speeds of the atoms entering the ToF-MS are similar, the spread in velocities for the two sources differ. The effusive source provide Sn atoms with thermal energies, and due to this the atoms have a large velocity spread in the directions parallel and transverse to the atomic beam direction. Using the supersonic jet source has the advantage that the sample undergoes adiabatic cooling during the free jet expansion. The sample is cooled down to a few Kelvin, reducing the spread in velocities of the atoms in the jet. The supersonic jet source is ideal to reduce the effects of Doppler broadening, but implementation will be more complex than an effusive source. The supersonic jet source requires precise timing between the dedicated ablation laser, the pulsed valve, and the ionizing lasers.

The IBSimu simulation library [79] was used to simulate the flight of three Sn isotopes through the specific ToF-MS available at Stellenbosch University. The three most abundant isotopes of Sn (^{120}Sn, ^{118}Sn, and ^{116}Sn) were chosen as test cases for the simulations. The simulations were used to investigate the influence of various experimental parameters in an effort to predict the optimal parameters for the setup. The results of the simulations were reported in Chapter 5.3.

From the simulated time-of-flight spectra it was shown how the time axis can be calibrated to present the mass of the ions. The definition of the resolution of a ToF-MS was also provided. Different mass pairs were used to determine the mass resolution of the available ToF-MS instrument to be ~ 570, meaning the instrument will able to resolve mass peaks one atomic mass unit apart up to ~ 570.

The influence of the initial volume of ions was investigated. The ion beam radius in an actual experiment will be determined by the spot size of the ionizing laser light. From the simulated results it seems favourable to select a smaller spot size, as this will lead to a higher resolution. The spot size, however, should not be made too small. When the spot size becomes too small, space charge effects start to reduce the resolution of the mass spectra.

The impact of the velocity distribution on the widths of the mass peaks was investigated. It was observed that the peak widths only increased by $\sim 10\%$ when the speed distribution typical to the skimmed gas jet is introduced

($dv_\perp = 3$ m/s). The change in the peak widths illustrates the importance of proper collimation of incident atomic beams to reduce the spread in the transverse velocity components of the atoms, leading to a better resolution of the ToF-MS.

The ToF-MS available at Stellenbosch University is fitted with an ion reflector called a reflectron. The impact of the reflectron was studied by comparing simulated mass spectra at the spatial focus of the ionization region of the ToF-MS, just before the reflectron, and at the detector position after the reflectron. It was observed that the reflectron greatly improves the resolution of the instrument.

The reflectron is a crucial component to obtain high resolution spectra, and it was decided to investigate the influence of the reflectron. The reflectron consists of a grounded front electrode, an intermediate electrode with adjustable voltage, and a high voltage backplate. The design of the entire ToF-MS including the reflectron was illustrated in Chapter 3. The voltage applied to the intermediate electrode of the reflectron was changed between 800 V and 1200 V and the effect on the flight time and resolution was studied. A voltage close to 1000 V giving the most linear voltage gradient was found to be optimal.

Finally, a comparison was made between the time-of-flight mass spectra when using supersonic jet source and the effusive beam source respectively. It was observed that the effussive source leads to more ions being lost as they do not reach the detector. This is due to the high speed distribution of the atoms in the forward direction. The effect of Doppler broadening of the spectral lines in both sources was also compared. From the calculations, it was observed that the Doppler broadening in the effusive source was higher compared to the Doppler broadening in the jet. While the effusive source is easier to implement, the Doppler broadening is reduced in the supersonic jet. The supersonic jet source is therefore crucial if selective ionization of a specific isotope of Sn is required.

The ToF-MS could not be implemented during the time frame of this project due to administrative delays. The instrument only arrived in August 2018 and the process of replacing the detector will only be done in early 2019. For that reason the planned proof of concept experiments could not be done.

It can be concluded that the experimental setup has been developed as far as possible without the ToF-MS instrument. The laser setup and atom sources have been designed and built. The ToF-MS has been studied by simulation. This yielded an understanding of the relative effect of different instrumental parameters and sample conditions that will facilitate the implementation of the instrument in the setup in future.

6.2   Future Work

The following section will include some suggestions for future work based on the work done in this thesis.

The simulation of the ToF-MS was useful to observe the influence various experimental parameters will have on the resolution of the instrument. In the simulation all the ions are generated at the same time, in an actual experiment the ions will be generated over the duration of the laser pulse (~ 10 ns). In future, it would be worthwhile to look into implementing this time delay into the simulation.

The ToF-MS instrument should be commissioned and tested in the laboratory. The alignment of the ionizing laser light as well as the ablation laser has to be done and the atomic beam sources have to be integrated. The data acquisition procedure for the instrument should be set up and synchronized with the existing laboratory setup controlling the lasers.

Once the ToF-MS has been commissioned it will be useful to develop, test, and optimize RIS schemes for the element of interest using the ToF-MS. One way to increase the ionization efficiency of a RIS scheme is to use auto-ionization states. It would be useful to search for auto-ionization by adjusting the ionization wavelength and monitoring the ion yield through the mass spectra. The RIS schemes can also be adjusted to include different intermediate states before ionization. Different RIS schemes can be compared in terms of ionization effiency as well as isotope selectivity.

Doppler-free techniques should also be implemented, especially when using the effusive atomic beam. The Doppler-free techniques will provide the basis for performing isotope selective ionization, when a laser with a narrow enough bandwidth is used.

Appendices

Appendix A

Full IBSimu code

A.1   Ionization region of the ToF-MS

```cpp
1  #include "epot_bicgstabsolver.hpp"
2  #include "geometry.hpp"
3  #include "func_solid.hpp"
4  #include "epot_efield.hpp"
5  #include "meshvectorfield.hpp"
6  #include "particledatabase.hpp"
7  #include "geomplotter.hpp"
8  #include "ibsimu.hpp"
9  #include "error.hpp"
10 #include "gtkwindow.hpp"
11 #include "gtkplotter.hpp"
12 #include "geom3dplot.hpp"
13 #include "gtkparticlediagdialog.hpp"
14 #include "iostream"
15 #include "sstream"
16 #include "iomanip"
17 using namespace std;
18
19 bool solid1( double x, double y, double z )
20 {
21     double r = sqrt(x*x+z*z);
22     return( y <= 0.004 && r >= 0.0);
23 }
24
25
26 bool solid2( double x, double y, double z )
27 {
28     double r = sqrt(x*x+z*z);
29     return( y >= 0.014 && y <= 0.0165 && r >= 0.03 );
30 }
31
32
33 bool solid3( double x, double y, double z )
34 {
```

105

```
35        double  r = sqrt(x*x+z*z);
36        return( y >= 0.0255 && y <= 0.028 && r >= 0.0125);
37  }
38
39
40  bool solid4( double x, double y, double z )
41  {
42        double  r = sqrt(x*x+z*z);
43        return( y >= 0.038 && y <= 0.0405 && r >= 0.0125);
44  }
45
46
47  void simu ( int argc , char **argv )
48  {
49        Geometry geom( MODE_3D, Int3D(91,301,91), Vec3D(-0.045,0,-0.045), 1e-3 );
50
51        Solid *s1 = new FuncSolid( solid1 );
52        geom.set_solid( 7, s1 );
53        Solid *s2 = new FuncSolid( solid2 );
54        geom.set_solid( 8, s2 );
55        Solid *s3 = new FuncSolid( solid3 );
56        geom.set_solid( 9, s3 );
57        Solid *s4 = new FuncSolid( solid4 );
58        geom.set_solid( 10, s4 );
59
60        geom.set_boundary( 1, Bound(BOUND_NEUMANN,       0.0  ) );
61        geom.set_boundary( 2, Bound(BOUND_NEUMANN,       0.0  ) );
62        geom.set_boundary( 3, Bound(BOUND_NEUMANN,       0.0  ) );
63        geom.set_boundary( 4, Bound(BOUND_NEUMANN,       0.0  ) );
64        geom.set_boundary( 5, Bound(BOUND_NEUMANN,       0.0  ) );
65        geom.set_boundary( 6, Bound(BOUND_NEUMANN,       0.0  ) );
66
67        geom.set_boundary( 7, Bound(BOUND_DIRICHLET,  2.0e3) );
68        geom.set_boundary( 8, Bound(BOUND_DIRICHLET,  1.6e3) );
69        geom.set_boundary( 9, Bound(BOUND_DIRICHLET,  0.9e3) );
70        geom.set_boundary( 10, Bound(BOUND_DIRICHLET,   0.0e3) );
71        geom.build_mesh();
72        geom.save( "tofgeom.dat" );
73
74        EpotField epot( geom );
75        MeshScalarField scharge( geom );
76        MeshScalarField scharge_ave( geom );
77        MeshVectorField bfield;
78        EpotEfield efield( epot );
79        field_extrpl_e efldextrpl[6] = { FIELD_EXTRAPOLATE, FIELD_EXTRAPOLATE,
80                       FIELD_SYMMETRIC_POTENTIAL, FIELD_EXTRAPOLATE,
81                       FIELD_EXTRAPOLATE, FIELD_EXTRAPOLATE };
82        efield.set_extrapolation( efldextrpl );
83
84        EpotBiCGSTABSolver solver( geom, 1.0e-4, 1000000, 1.0e-4, 10, true
    );
85
```

```
86          ParticleDataBase3D pdb( geom );
87          bool pmirror[6] = { false, false, false, false, false, false };
88          pdb.set_mirror( pmirror );
89          pdb.set_surface_collision( false );
90
91          for( size_t i = 0; i < 5; i++ ) {
92          solver.solve( epot, scharge );
93          efield.recalculate();
94          //defining input particle beams or effusive sources
95          pdb.clear();
96          pdb.add_cylindrical_beam_with_velocity( 15000, 0, 1.0, 120,
97                                  351.74, 187.0, 7.03,
98                                  Vec3D(0.0,0.009,0.00),
99                                  Vec3D(1,0,0),
100                                 Vec3D(0,1,0),
101                                 0.0005 );
102         pdb.iterate_trajectories( scharge, efield, bfield );
103         pdb.add_cylindrical_beam_with_velocity( 11250, 0, 1.0, 118,
104                                 354.71, 189.0, 7.09,
105                                 Vec3D(0.0,0.009,0.00),
106                                 Vec3D(1,0,0),
107                                 Vec3D(0,1,0),
108                                 0.0005 );
109         pdb.iterate_trajectories( scharge, efield, bfield );
110         pdb.add_cylindrical_beam_with_velocity( 6750, 0 , 1.0, 116,
111                                 357.75, 190.0, 7.15,
112                                 Vec3D(0.0,0.009,0.00),
113                                 Vec3D(1,0,0),
114                                 Vec3D(0,1,0),
115                                 0.0005 );
116         pdb.iterate_trajectories( scharge, efield, bfield );
117         pdb.add_cylindrical_beam_with_velocity( 5000, 0.0, 0, 120,
118                                 351.74, 0.0, 0.0,
119                                 Vec3D(0.00,0.009,-0.045),
120                                 Vec3D(1,0,0),
121                                 Vec3D(0,1,0),
122                                 0.0005 );
123         pdb.iterate_trajectories( scharge, efield, bfield );
124         pdb.save("pdb.dat");
125
126         /*//defining input particle beams or gas jet sources
127         pdb.clear();
128         pdb.add_cylindrical_beam_with_velocity( 15000, 0, 1.0, 120,
129                                 558.89, 53.99, 2.83,
130                                 Vec3D(0.0,0.009,0.00),
131                                 Vec3D(1,0,0),
132                                 Vec3D(0,1,0),
133                                 0.0005 );
134         pdb.iterate_trajectories( scharge, efield, bfield );
135         pdb.add_cylindrical_beam_with_velocity( 11250, 0, 1.0, 118,
136                                 558.89, 53.99, 2.83,
137                                 Vec3D(0.0,0.009,0.00),
```

```
138                            Vec3D(1,0,0),
139                            Vec3D(0,1,0),
140                            0.0005 );
141       pdb.iterate_trajectories( scharge, efield, bfield );
142       pdb.add_cylindrical_beam_with_velocity( 6750, 0, 1.0, 116,
143                            558.89, 53.99, 2.83,
144                            Vec3D(0.0,0.009,0.00),
145                            Vec3D(1,0,0),
146                            Vec3D(0,1,0),
147                            0.0005 );
148       pdb.iterate_trajectories( scharge, efield, bfield );
149       pdb.add_cylindrical_beam_with_velocity( 5000, 0.0, 0, 120,
150                            558.89, 53.99, 2.83,
151                            Vec3D(0.00,0.009,-0.045),
152                            Vec3D(1,0,0),
153                            Vec3D(0,1,0),
154                            0.0005 );
155       pdb.iterate_trajectories( scharge, efield, bfield );
156       pdb.save("pdb.dat");*/
157
158       //saving trajectory diagnostics for effusive sources
159       std::vector<trajectory_diagnostic_e> diagnostics;
160       diagnostics.push_back( DIAG_T  );
161       diagnostics.push_back( DIAG_X  );
162       diagnostics.push_back( DIAG_VX );
163       diagnostics.push_back( DIAG_Y  );
164       diagnostics.push_back( DIAG_VY );
165       diagnostics.push_back( DIAG_Z  );
166       diagnostics.push_back( DIAG_VZ );
167       diagnostics.push_back( DIAG_MASS );
168       diagnostics.push_back( DIAG_QM );
169       diagnostics.push_back( DIAG_CURR );
170       TrajectoryDiagnosticData tof_effusive;
171       pdb.trajectories_at_plane( tof_effusive, AXIS_Y, 0.3, diagnostics );
172       tof_effusive.export_data   ( "tof_effusive.txt" );
173
174       const TrajectoryDiagnosticColumn &time = tof_effusive(0);
175
176
177       Histogram1D tofeffusive_histo( 61, time.data());
178       vector<double> time_data = tofeffusive_histo.get_data();
179       ofstream of_histo( "tofeffusive_histo.txt" );
180       for( uint32_t i = 0; i < tofeffusive_histo.n(); i++ ) {
181       of_histo << tofeffusive_histo.coord(i) << " "
182           << tofeffusive_histo(i) << "\n";
183       }
184       /*//saving trajectory diagnostics for jet sources
185       std::vector<trajectory_diagnostic_e> diagnostics;
186       diagnostics.push_back( DIAG_T  );
187       diagnostics.push_back( DIAG_X  );
188       diagnostics.push_back( DIAG_VX );
189       diagnostics.push_back( DIAG_Y  );
```

```
190        diagnostics.push_back( DIAG_VY );
191        diagnostics.push_back( DIAG_Z );
192        diagnostics.push_back( DIAG_VZ );
193        diagnostics.push_back( DIAG_MASS );
194        diagnostics.push_back( DIAG_QM );
195        diagnostics.push_back( DIAG_CURR );
196        TrajectoryDiagnosticData tof_jet;
197        pdb.trajectories_at_plane( tof_jet, AXIS_Y, 0.3, diagnostics );
198        tof_jet.export_data ( "tof_jet.txt" );
199
200        const TrajectoryDiagnosticColumn &time = tof_jet(0);
201
202
203        Histogram1D tofjet_histo( 61, time.data());
204        vector<double> time_data = tofjet_histo.get_data();
205        ofstream of_histo( "tofjet_histo.txt" );
206        for( uint32_t i = 0; i < tofjet_histo.n(); i++ ) {
207        of_histo << tofjet_histo.coord(i) << " "
208            << tofjet_histo(i) << "\n";
209        }*/
210
211        }
212        // Write output file containing all particles for effusive sources
213        string fnpout = "tofeffusive_out.txt";
214        ofstream fileOut( fnpout.c_str() );
215        for( size_t k = 0; k < pdb.size(); k++ ) {
216        // Output coordinates
217        Particle3D &pp = pdb.particle( k );
218        fileOut << setw(12) << pp.IQ() << " ";
219        fileOut << setw(12) << pp.m() << " ";
220        for( size_t j = 0; j < 7; j ++ )
221            fileOut << setw(12) << pp(j) << " ";
222        fileOut << "\n";
223        }
224        fileOut.close();
225
226        /*// Write output file containing all particles for jet sources
227        string fnpout = "tofjet_out.txt";
228        ofstream fileOut( fnpout.c_str() );
229        for( size_t k = 0; k < pdb.size(); k++ ) {
230        // Output coordinates
231        Particle3D &pp = pdb.particle( k );
232        fileOut << setw(12) << pp.IQ() << " ";
233        fileOut << setw(12) << pp.m() << " ";
234        for( size_t j = 0; j < 7; j ++ )
235            fileOut << setw(12) << pp(j) << " ";
236        fileOut << "\n";
237        }
238        fileOut.close();*/
239
240        // Set parameters for plotting
241        GeomPlotter geomplotter( geom );
```

```
242        geomplotter.set_size( 980, 980 );
243        geomplotter.set_epot( &epot );
244        geomplotter.set_particle_database( &pdb );
245        geomplotter.set_view( VIEW_YZ, 0 );
246        geomplotter.plot_png( "tofplot_yz.jpg" );
247        geomplotter.set_view( VIEW_XY, 0 );
248        geomplotter.plot_png( "tofplot_xy.jpg" );
249
250        if( true ) {
251            MeshScalarField tdens( geom );
252            pdb.build_trajectory_density_field( tdens );
253            GTKPlotter plotter( &argc, &argv );
254            plotter.set_geometry( &geom );
255            plotter.set_epot( &epot );
256            plotter.set_bfield( &bfield );
257            plotter.set_efield( &efield );
258            plotter.set_scharge( &scharge_ave );
259            plotter.set_trajdens( &tdens );
260            plotter.set_particledatabase( &pdb );
261            plotter.new_geometry_plot_window();
262            plotter.run();
263    }
264 }
265
266 int main( int argc, char **argv )
267 {
268      try {
269      ibsimu.set_message_threshold( MSG_VERBOSE, 1 );
270      ibsimu.set_thread_count( 4 );
271          simu(argc, argv);
272      } catch ( Error e ) {
273          e.print_error_message( ibsimu.message( 0 ) );
274          exit( 1 );
275      }
276
277      return( 0 );
278
279 }
```

A.2   Reflectron of the ToF-MS

```
1 #include "epot_bicgstabsolver.hpp"
2 #include "geometry.hpp"
3 #include "func_solid.hpp"
4 #include "epot_efield.hpp"
5 #include "meshvectorfield.hpp"
6 #include "particledatabase.hpp"
7 #include "geomplotter.hpp"
8 #include "ibsimu.hpp"
9 #include "error.hpp"
```

```cpp
10  #include "gtkwindow.hpp"
11  #include "gtkplotter.hpp"
12  #include "geom3dplot.hpp"
13  #include "gtkparticlediagdialog.hpp"
14  #include "readascii.hpp"
15  #include "iostream"
16  #include "sstream"
17  #include "iomanip"
18  using namespace std;
19  //defining geometries of reflectron
20  bool solid1( double x, double y, double z ) //Backplate van reflectron - 2kV
21  {
22      double r = sqrt(x*x+z*z);
23      return( y >= 0.5895 && r >= 0.0);
24  }
25
26
27  bool solid2( double x, double y, double z )
28  {
29      double r = sqrt(x*x+z*z);
30      return( y >= 0.5845 && y <= 0.5850 && r >= 0.028 );
31  }
32
33
34  bool solid3( double x, double y, double z )
35  {
36      double r = sqrt(x*x+z*z);
37      return( y >= 0.5795 && y <= 0.5800 && r >= 0.028 );
38  }
39
40
41  bool solid4( double x, double y, double z )
42  {
43      double r = sqrt(x*x+z*z);
44      return( y >= 0.5744 && y <= 0.5751 && r >= 0.028 );
45  }
46
47
48  bool solid5( double x, double y, double z )
49  {
50      double r = sqrt(x*x+z*z);
51      return( y >= 0.5693 && y <= 0.5701 && r >= 0.028 );
52  }
53
54
55  bool solid6( double x, double y, double z )
56  {
57      double r = sqrt(x*x+z*z);
58      return( y >= 0.5645 && y <= 0.5650 && r >= 0.028 );
59  }
60
61
```

```
62  bool solid7 ( double x , double y , double z )
63  {
64      double r = sqrt (x*x+z*z);
65      return ( y >= 0.5593 && y <= 0.5601 && r >= 0.028 );
66  }
67
68
69  bool solid8 ( double x , double y , double z )
70  {
71      double r = sqrt (x*x+z*z);
72      return ( y >= 0.5545 && y <= 0.5550 && r >= 0.028 );
73  }
74
75
76  bool solid9 ( double x , double y , double z )
77  {
78      double r = sqrt (x*x+z*z);
79      return ( y >= 0.5495 && y <= 0.5500 && r >= 0.028 );
80  }
81
82
83  bool solid10 ( double x , double y , double z )
84  {
85      double r = sqrt (x*x+z*z);
86      return ( y >= 0.5445 && y <= 0.5450 && r >= 0.028 );
87  }
88
89
90  bool solid11 ( double x , double y , double z )
91  {
92      double r = sqrt (x*x+z*z);
93      return ( y >= 0.5395 && y <= 0.5400 && r >= 0.028 );
94  }
95
96
97  bool solid12 ( double x , double y , double z )
98  {
99      double r = sqrt (x*x+z*z);
100     return ( y >= 0.5345 && y <= 0.5350 && r >= 0.028 );
101 }
102
103
104 bool solid13 ( double x , double y , double z )
105 {
106     double r = sqrt (x*x+z*z);
107     return ( y >= 0.5295 && y <= 0.5300 && r >= 0.028 );
108 }
109
110
111 bool solid14 ( double x , double y , double z )// Retard − 800−1200V
112 {
113     double r = sqrt (x*x+z*z);
```

```
114          return ( y >= 0.5240 && y <= 0.5250 && r >= 0.028 );
115  }
116
117
118  bool solid15 ( double x , double y , double z )
119  {
120          double r = sqrt (x*x+z*z );
121          return ( y >= 0.5190 && y <= 0.5195 && r >= 0.028 );
122  }
123
124
125  bool solid16 ( double x , double y , double z )
126  {
127          double r = sqrt (x*x+z*z );
128          return ( y >= 0.5150 && y <= 0.5155 && r >= 0.028 );
129  }
130
131
132  bool solid17 ( double x , double y , double z )
133  {
134          double r = sqrt (x*x+z*z );
135          return ( y >= 0.5100 && y <= 0.5105 && r >= 0.028 );
136  }
137
138
139  bool solid18 ( double x , double y , double z )
140  {
141          double r = sqrt (x*x+z*z );
142          return ( y >= 0.5050 && y <= 0.5055 && r >= 0.028 );
143  }
144
145
146  bool solid19 ( double x , double y , double z )
147  {
148          double r = sqrt (x*x+z*z );
149          return ( y >= 0.5000 && y <= 0.5005 && r >= 0.028 );
150  }
151
152
153  bool solid20 ( double x , double y , double z )
154  {
155          double r = sqrt (x*x+z*z );
156          return ( y >= 0.4950 && y <= 0.4955 && r >= 0.028 );
157  }
158
159
160  bool solid21 ( double x , double y , double z )
161  {
162          double r = sqrt (x*x+z*z );
163          return ( y >= 0.4900 && y <= 0.4905 && r >= 0.028 );
164  }
165
```

```
166
167   bool solid22( double x, double y, double z )
168   {
169        double r = sqrt(x*x+z*z);
170        return( y >= 0.4850 && y <= 0.4855 && r >= 0.028 );
171   }
172
173
174   bool solid23( double x, double y, double z )
175   {
176        double r = sqrt(x*x+z*z);
177        return( y >= 0.4800 && y <= 0.4805 && r >= 0.028 );
178   }
179
180
181   bool solid24( double x, double y, double z )//FFR − 0V
182   {
183        double r = sqrt(x*x+z*z);
184        return( y >= 0.4750 && y <= 0.4755 && r >= 0.028 );
185   }
186
187
188   void simu ( int argc, char **argv )
189   {
190        Geometry geom( MODE_3D, Int3D(91,301,91), Vec3D(−0.045,0.29,−0.045), 1e−3 );
191        //defining solids
192        Solid *s1 = new FuncSolid( solid1 );
193        geom.set_solid( 7, s1 );
194        Solid *s2 = new FuncSolid( solid2 );
195        geom.set_solid( 8, s2 );
196        Solid *s3 = new FuncSolid( solid3 );
197        geom.set_solid( 9, s3 );
198        Solid *s4 = new FuncSolid( solid4 );
199        geom.set_solid( 10, s4 );
200        Solid *s5 = new FuncSolid( solid5 );
201        geom.set_solid( 11, s5 );
202        Solid *s6 = new FuncSolid( solid6 );
203        geom.set_solid( 12, s6 );
204        Solid *s7 = new FuncSolid( solid7 );
205        geom.set_solid( 13, s7 );
206        Solid *s8 = new FuncSolid( solid8 );
207        geom.set_solid( 14, s8 );
208        Solid *s9 = new FuncSolid( solid9 );
209        geom.set_solid( 15, s9 );
210        Solid *s10 = new FuncSolid( solid10 );
211        geom.set_solid( 16, s10 );
212        Solid *s11 = new FuncSolid( solid11 );
213        geom.set_solid( 17, s11 );
214        Solid *s12 = new FuncSolid( solid12 );
215        geom.set_solid( 18, s12 );
216        Solid *s13 = new FuncSolid( solid13 );
217        geom.set_solid( 19, s13 );
```

```cpp
218        Solid *s14 = new FuncSolid( solid14 );
219        geom.set_solid( 20, s14 );
220        Solid *s15 = new FuncSolid( solid15 );
221        geom.set_solid( 21, s15 );
222        Solid *s16 = new FuncSolid( solid16 );
223        geom.set_solid( 22, s16 );
224        Solid *s17 = new FuncSolid( solid17 );
225        geom.set_solid( 23, s17 );
226        Solid *s18 = new FuncSolid( solid18 );
227        geom.set_solid( 24, s18 );
228        Solid *s19 = new FuncSolid( solid19 );
229        geom.set_solid( 25, s19 );
230        Solid *s20 = new FuncSolid( solid20 );
231        geom.set_solid( 26, s20 );
232        Solid *s21 = new FuncSolid( solid21 );
233        geom.set_solid( 27, s21 );
234        Solid *s22 = new FuncSolid( solid22 );
235        geom.set_solid( 28, s22 );
236        Solid *s23 = new FuncSolid( solid23 );
237        geom.set_solid( 29, s23 );
238        Solid *s24 = new FuncSolid( solid24 );
239        geom.set_solid( 30, s24 );
240
241        geom.set_boundary( 1, Bound(BOUND_NEUMANN,          0.0   ) );
242        geom.set_boundary( 2, Bound(BOUND_NEUMANN,          0.0   ) );
243        geom.set_boundary( 3, Bound(BOUND_NEUMANN,          0.0   ) );
244        geom.set_boundary( 4, Bound(BOUND_NEUMANN,          0.0   ) );
245        geom.set_boundary( 5, Bound(BOUND_NEUMANN,          0.0   ) );
246        geom.set_boundary( 6, Bound(BOUND_NEUMANN,          0.0   ) );
247
248        geom.set_boundary( 7,  Bound(BOUND_DIRICHLET,   2.0e3) );//reflect
249        geom.set_boundary( 8,  Bound(BOUND_DIRICHLET,   1.908e3) );
250        geom.set_boundary( 9,  Bound(BOUND_DIRICHLET,   1.815e3) );
251        geom.set_boundary( 10, Bound(BOUND_DIRICHLET,   1.723e3) );
252        geom.set_boundary( 11, Bound(BOUND_DIRICHLET,   1.631e3) );
253        geom.set_boundary( 12, Bound(BOUND_DIRICHLET,   1.538e3) );
254        geom.set_boundary( 13, Bound(BOUND_DIRICHLET,   1.446e3) );
255        geom.set_boundary( 14, Bound(BOUND_DIRICHLET,   1.354e3) );
256        geom.set_boundary( 15, Bound(BOUND_DIRICHLET,   1.262e3) );
257        geom.set_boundary( 16, Bound(BOUND_DIRICHLET,   1.169e3) );
258        geom.set_boundary( 17, Bound(BOUND_DIRICHLET,   1.077e3) );
259        geom.set_boundary( 18, Bound(BOUND_DIRICHLET,   0.985e3) );
260        geom.set_boundary( 19, Bound(BOUND_DIRICHLET,   0.892e3) );
261        geom.set_boundary( 20, Bound(BOUND_DIRICHLET,   0.8e3) );//retard
262        geom.set_boundary( 21, Bound(BOUND_DIRICHLET,   0.720e3) );
263        geom.set_boundary( 22, Bound(BOUND_DIRICHLET,   0.640e3) );
264        geom.set_boundary( 23, Bound(BOUND_DIRICHLET,   0.560e3) );
265        geom.set_boundary( 24, Bound(BOUND_DIRICHLET,   0.480e3) );
266        geom.set_boundary( 25, Bound(BOUND_DIRICHLET,   0.400e3) );
267        geom.set_boundary( 26, Bound(BOUND_DIRICHLET,   0.320e3) );
268        geom.set_boundary( 27, Bound(BOUND_DIRICHLET,   0.240e3) );
269        geom.set_boundary( 28, Bound(BOUND_DIRICHLET,   0.160e3) );
```

```
270        geom.set_boundary( 29, Bound(BOUND_DIRICHLET,   0.080e3) );
271        geom.set_boundary( 30, Bound(BOUND_DIRICHLET,   0.0e3) );//FFR
272
273        geom.build_mesh();
274        geom.save( "geom.dat" );
275
276        EpotField epot( geom );
277        MeshScalarField scharge( geom );
278        MeshVectorField bfield;
279        EpotEfield efield( epot );
280        field_extrpl_e efldextrpl[6] = { FIELD_EXTRAPOLATE, FIELD_EXTRAPOLATE,
281                        FIELD_SYMMETRIC_POTENTIAL, FIELD_EXTRAPOLATE,
282                        FIELD_EXTRAPOLATE, FIELD_EXTRAPOLATE };
283        efield.set_extrapolation( efldextrpl );
284
285        EpotBiCGSTABSolver solver( geom, 1.0e-4, 1000000, 1.0e-4, 10, true );
286
287        ParticleDataBase3D pdb( geom );
288        bool pmirror[6] = { false, false, false, false, false, false };
289        pdb.set_mirror( pmirror );
290        pdb.set_surface_collision( false );
291
292        // Input particles for effusive sources
293        ReadAscii din( "tofeffusive_out.txt", 9 );
294        cout << "Reading " << din.rows() << " particles\n";
295
296        /*// Input particles or jet sources
297        ReadAscii din( "tofjet_out.txt", 9 );
298        cout << "Reading " << din.rows() << " particles\n";*/
299
300
301        for( size_t i = 0; i < 5; i++ ) {
302        solver.solve( epot, scharge );
303        efield.recalculate();
304
305        pdb.clear();
306        // Go through all read particles
307        for( size_t i = 0; i < din.rows(); i++ ) {
308            double I  = din[0][i];
309            double m  = din[1][i];
310            double t  = din[2][i];
311            double x  = din[3][i];
312            double vx = din[4][i];
313            double y  = din[5][i];
314            double vy = din[6][i];
315            double z  = din[7][i];
316            double vz = din[8][i];
317
318        pdb.add_particle( I, 1.0, m/1.66054e-027, ParticleP3D(t,x,vx,y,vy,z,vz) );
319        }
320
321        pdb.iterate_trajectories( scharge, efield, bfield );
```

```
322
323        // Trajectory diagnostics for effusive sources
324        std::vector<trajectory_diagnostic_e> diagnostics;
325        diagnostics.push_back( DIAG_T );
326        diagnostics.push_back( DIAG_X   );
327        diagnostics.push_back( DIAG_VX );
328        diagnostics.push_back( DIAG_Y );
329        diagnostics.push_back( DIAG_VY );
330        diagnostics.push_back( DIAG_Z );
331        diagnostics.push_back( DIAG_VZ );
332        diagnostics.push_back( DIAG_MASS );
333        diagnostics.push_back( DIAG_QM );
334        diagnostics.push_back( DIAG_CURR );
335        TrajectoryDiagnosticData reflectron_effusive;
336        pdb.trajectories_at_plane( reflectron_effusive, AXIS_Y, 0.29, diagnostics );
337        reflectron_effusive.export_data ( "reflectron_effusive.txt" );
338        const TrajectoryDiagnosticColumn &time = reflectron_effusive(0);
339
340
341        Histogram1D refeffusive_histo( 150, time.data());
342        vector<double> time_data = refeffusive_histo.get_data();
343        ofstream of_histo( "refeffusive_histo.txt" );
344        for( uint32_t i = 0; i < refeffusive_histo.n(); i++ ) {
345        of_histo << refeffusive_histo.coord(i) << " "
346            << refeffusive_histo(i) << "\n";
347        }
348        /*// Trajectory diagnostics for jet sources
349        std::vector<trajectory_diagnostic_e> diagnostics;
350        diagnostics.push_back( DIAG_T );
351        diagnostics.push_back( DIAG_X   );
352        diagnostics.push_back( DIAG_VX );
353        diagnostics.push_back( DIAG_Y );
354        diagnostics.push_back( DIAG_VY );
355        diagnostics.push_back( DIAG_Z );
356        diagnostics.push_back( DIAG_VZ );
357        diagnostics.push_back( DIAG_MASS );
358        diagnostics.push_back( DIAG_QM );
359        diagnostics.push_back( DIAG_CURR );
360        TrajectoryDiagnosticData reflectron_jet;
361        pdb.trajectories_at_plane( reflectron_jet, AXIS_Y, 0.29, diagnostics );
362        reflectron_jet.export_data  ( "reflectron_jet.txt" );
363        const TrajectoryDiagnosticColumn &time = reflectron_jet(0);
364
365
366        Histogram1D refjet_histo( 150, time.data());
367        vector<double> time_data = refjet_histo.get_data();
368        ofstream of_histo( "refjet_histo.txt" );
369        for( uint32_t i = 0; i < refjet_histo.n(); i++ ) {
370        of_histo << refjet_histo.coord(i) << " "
371            << refjet_histo(i) << "\n";
372        }*/
373        }
```

```
374
375
376
377         // Set parameters for plotting
378         GeomPlotter geomplotter( geom );
379         geomplotter.set_size( 980, 980 );
380         geomplotter.set_epot( &epot );
381         geomplotter.set_particle_database( &pdb );
382         geomplotter.set_view( VIEW_YZ, 0 );
383         geomplotter.plot_png( "refplot_YZ1.jpg" );
384         geomplotter.set_view( VIEW_YX, 0 );
385         geomplotter.plot_png( "refplot_YX1.jpg" );
386
387         if( true ) {
388             MeshScalarField tdens( geom );
389             pdb.build_trajectory_density_field( tdens );
390             GTKPlotter plotter( &argc, &argv );
391             plotter.set_geometry( &geom );
392             plotter.set_epot( &epot );
393             plotter.set_bfield( &bfield );
394             plotter.set_efield( &efield );
395             plotter.set_scharge( &scharge );
396             plotter.set_trajdens( &tdens );
397             plotter.set_particledatabase( &pdb );
398             plotter.new_geometry_plot_window();
399             plotter.run();
400     }
401 }
402
403 int main( int argc, char **argv )
404 {
405     try {
406     ibsimu.set_message_threshold( MSG_VERBOSE, 1 );
407     ibsimu.set_thread_count( 4 );
408         simu(argc, argv);
409     } catch ( Error e ) {
410         e.print_error_message( ibsimu.message( 0 ) );
411         exit( 1 );
412     }
413
414     return( 0 );
415 }
```

List of References

[1] MEDICIS: a new CERN facility can help medical research into cancer. 2017.
Available at: https://ep-news.web.cern.ch/content/medicis-new-cern-facility-can-help-medical-research-cancer

[2] Couturier, O., Supiot, S., Degraef-Mougin, M., Faivre-Chauvet, A., Carlier, T., Chatal, J.-F., Davodeau, F. and Cherel, M.: Cancer radioimmunotherapy with alpha-emitting nuclides. *European Journal of Nuclear Medicine and Molecular Imaging*, vol. 32, no. 5, pp. 601–614, Apr 2005.
Available at: https://doi.org/10.1007/s00259-005-1803-2

[3] de Bruin, L.: UP leads the world in using nuclear therapy to fight cancer. 2018.
Available at: https://www.up.ac.za/news/post_2629948-up-leads-the-world-in-using-nuclear-therapy-to-fight-cancer-

[4] Sathekge, M., Bruchertseifer, F., Knoesen, O., Reyneke, F., Lawal, I., Lengana, T., Davis, C., Mahapane, J., Corbett, C., Vorster, M. and Morgenstern, A.: 225ac-PSMA-617 in chemotherapy-naive patients with advanced prostate cancer: a pilot study. *European Journal of Nuclear Medicine and Molecular Imaging*, vol. 46, no. 1, pp. 129–138, Sep 2018.
Available at: https://doi.org/10.1007/s00259-018-4167-0

[5] Bark, R. and Cornell, J.: A radioactive-ion beam facility at ithemba LABS. Tech. Rep., iThemba LABS, 2013.

[6] Mayer, M.G.: On closed shells in nuclei. *Phys. Rev.*, vol. 74, pp. 235–239, Aug 1948.
Available at: https://link.aps.org/doi/10.1103/PhysRev.74.235

[7] Mayer, M.G.: On closed shells in nuclei. ii. *Phys. Rev.*, vol. 75, pp. 1969–1970, Jun 1949.
Available at: https://link.aps.org/doi/10.1103/PhysRev.75.1969

[8] Schatz, H., Aprahamian, A., Barnard, V., Bildsten, L., Cumming, A., Ouellette, M., Rauscher, T., Thielemann, F.-K. and Wiescher, M.: End point of the *rp* process on accreting neutron stars. *Phys. Rev. Lett.*, vol. 86, pp. 3471–3474, Apr 2001.
Available at: https://link.aps.org/doi/10.1103/PhysRevLett.86.3471

119

[9] Wallace, R.K. and Woosley, S.E.: Explosive hydrogen burning. *The Astrophysical Journal Supplement Series*, vol. 45, pp. 389–420, 1981. ISSN 0067-0049.
Available at: `http://adsabs.harvard.edu/doi/10.1086/190717`

[10] Haxel, O., Jensen, J.H.D. and Suess, H.E.: On the "magic numbers" in nuclear structure. *Phys. Rev.*, vol. 75, pp. 1766–1766, Jun 1949.
Available at: `https://link.aps.org/doi/10.1103/PhysRev.75.1766.2`

[11] Casten, R.: *Nuclear structure from a simple perspective.* Oxford studies in nuclear physics. Oxford University Press, New York, N.Y., 1990. ISBN 0195045998.

[12] Caurier, E., Martínez-Pinedo, G., Nowacki, F., Poves, A. and Zuker, A.P.: The shell model as a unified view of nuclear structure. *Rev. Mod. Phys.*, vol. 77, pp. 427–488, Jun 2005.
Available at: `https://link.aps.org/doi/10.1103/RevModPhys.77.427`

[13] Lapoux, V., Somà, V., Barbieri, C., Hergert, H., Holt, J.D. and Stroberg, S.R.: Radii and binding energies in oxygen isotopes: A challenge for nuclear forces. *Phys. Rev. Lett.*, vol. 117, p. 052501, Jul 2016.
Available at: `https://link.aps.org/doi/10.1103/PhysRevLett.117.052501`

[14] Section, I.N.D.: Live chart of nuclides.
Available at: `https://www-nds.iaea.org/relnsd/vcharthtml/VChartHTML.html`

[15] Ferrer, R., Bree, N., Cocolios, T., Darby, I., De Witte, H., Dexters, W., Diriken, J., Elseviers, J., Franchoo, S., Huyse, M., Kesteloot, N., Kudryavtsev, Y., Pauwels, D., Radulov, D., Roger, T., Savajols, H., Van Duppen, P. and Venhart, M.: In-gas-cell laser ionization spectroscopy in the vicinity of ^{100}Sn: Magnetic moments and mean-square charge radii of N = 50-54 Ag. *Physics Letters B*, vol. 728, pp. 191–197, 2014. ISSN 03702693.
Available at: `http://linkinghub.elsevier.com/retrieve/pii/S0370269313009611`

[16] Allmond, J.M., Stuchbery, A.E., Galindo-Uribarri, A., Padilla-Rodal, E., Radford, D.C., Batchelder, J.C., Bingham, C.R., Howard, M.E., Liang, J.F., Manning, B., Pain, S.D., Stone, N.J., Varner, R.L. and Yu, C.H.: Investigation into the semimagic nature of the tin isotopes through electromagnetic moments. *Physical Review C - Nuclear Physics*, vol. 92, no. 4, pp. 1–5, 2015. ISSN 1089490X.

[17] Coraggio, L., Covello, A., Gargano, A., Itaco, N. and Kuo, T.T.: Shell-model study of quadrupole collectivity in light tin isotopes. *Physical Review C - Nuclear Physics*, vol. 91, no. 4, pp. 1–5, 2015. ISSN 1089490X. 1502.05822.

[18] Doornenbal, P., Takeuchi, S., Aoi, N., Matsushita, M., Obertelli, A., Steppenbeck, D., Wang, H., Audirac, L., Baba, H., Bednarczyk, P., Boissinot,

S., Ciemala, M., Corsi, A., Furumoto, T., Isobe, T., Jungclaus, A., Lapoux, V., Lee, J., Matsui, K., Motobayashi, T., Nishimura, D., Ota, S., Pollacco, E.C., Sakurai, H., Santamaria, C., Shiga, Y., Sohler, D. and Taniuchi, R.: Intermediate-energy Coulomb excitation of Sn 104: Moderate E2 strength decrease approaching Sn 100. *Physical Review C - Nuclear Physics*, vol. 90, no. 6, pp. 1–6, 2014. ISSN 1089490X. `arXiv:1305.2877v1`.

[19] Morris, T., Simonis, J., Stroberg, S., Stumpf, C., Hagen, G., Holt, J., Jansen, G., Papenbrock, T., Roth, R. and Schwenk, A.: Structure of the lightest tin isotopes. 2017. `arXiv:1709.02786`.

[20] Lewitowicz, M., Anne, R., Auger, G., Bazin, D., Borcea, C., Borrel, V., Corre, J., Dörfler, T., Fomichov, A., Grzywacz, R., Guillemaud-Mueller, D., Hue, R., Huyse, M., Janas, Z., Keller, H., Lukyanov, S., Mueller, A., Penionzhkevich, Y., Pfützner, M., Pougheon, F., Rykaczewski, K., Saint-Laurent, M., Schmidt, K., Schmidt-Ott, W., Sorlin, O., Szerypo, J., Tarasov, O., Wauters, J. and Zylicz, J.: Identification of the doubly-magic nucleus ^{100}Sn in the reaction ^{112}Sn + ^{nat}Ni at 63 MeV/nucleon. *Physics Letters B*, vol. 332, no. 1, pp. 20 – 24, 1994. ISSN 0370-2693.
Available at: `http://www.sciencedirect.com/science/article/pii/0370269394908524`

[21] Johnson, A., Seweryniak, D., Cederwall, B., Nyberg, J., Ata, A., Blomqvist, J., Cederkäll, J., Fahlander, C., Karny, M., Kerek, A., Kownacki, J., Norlin, L.-O., Wyss, R., Adamides, E., Grawe, H., Ideguchi, E., Julin, R., Juutinen, S., Karczmarczyk, W., Mitarai, S., Piiparinen, M., Schubart, R., Slotten, G., Törmänen, S. and Virtanen, A.: High-spin studies near ^{100}Sn with NORDBALL: New results on ^{102}In, ^{104}In and ^{108}Sb. *Nuclear Physics A*, vol. 557, no. Supplement C, pp. 401 – 410, 1993. ISSN 0375-9474.
Available at: `http://www.sciencedirect.com/science/article/pii/037594749390557E`

[22] Elomaa, V.-V., Vorobjev, G.K., Kankainen, A., Batist, L., Eliseev, S., Eronen, T., Hakala, J., Jokinen, A., Moore, I.D., Novikov, Y.N., Penttilä, H., Popov, A., Rahaman, S., Rissanen, J., Saastamoinen, A., Schatz, H., Seliverstov, D.M., Weber, C. and Äystö, J.: Quenching of the SnSbTe cycle in therpProcess. *Physical Review Letters*, vol. 102, no. 25, Jun 2009.
Available at: `https://doi.org/10.1103/physrevlett.102.252501`

[23] Erler, J., Birge, N., Kortelainen, M., Nazarewicz, W., Olsen, E., Perhac, A.M. and Stoitsov, M.: The limits of the nuclear landscape. *Nature*, vol. 486, no. 7404, pp. 509–512, 2012. ISSN 0028-0836.
Available at: `http://dx.doi.org/10.1038/nature11188`

[24] Langanke, K. and Wiescher, M.: Nuclear reactions and stellar processes. *Reports on Progress in Physics*, vol. 64, no. 12, p. 1657, 2001.
Available at: `http://stacks.iop.org/0034-4885/64/i=12/a=202`

[25] Seweryniak, D., Starosta, K., Davids, C.N., Gros, S., Hecht, A.A., Hoteling, N., Khoo, T.L., Lagergren, K., Lotay, G., Peterson, D., Robinson, A., Vaman, C., Walters, W.B., Woods, P.J. and Zhu, S.: α decay of ^{105}Te. *Phys. Rev. C*, vol. 73, p. 061301, Jun 2006.
Available at: https://link.aps.org/doi/10.1103/PhysRevC.73.061301

[26] Liddick, S.N., Grzywacz, R., Mazzocchi, C., Page, R.D., Rykaczewski, K.P., Batchelder, J.C., Bingham, C.R., Darby, I.G., Drafta, G., Goodin, C., Gross, C.J., Hamilton, J.H., Hecht, A.A., Hwang, J.K., Ilyushkin, S., Joss, D.T., Korgul, A., Królas, W., Lagergren, K., Li, K., Tantawy, M.N., Thomson, J. and Winger, J.A.: Discovery of ^{109}Xe and ^{105}Te: Superallowed α decay near doubly magic ^{100}Sn. *Phys. Rev. Lett.*, vol. 97, p. 082501, Aug 2006.
Available at: https://link.aps.org/doi/10.1103/PhysRevLett.97.082501

[27] Gamow, G. and Teller, E.: Selection rules for the β-disintegration. *Phys. Rev.*, vol. 49, pp. 895–899, Jun 1936.
Available at: https://link.aps.org/doi/10.1103/PhysRev.49.895

[28] Hinke, C., Böhmer, M., Boutachkov, P., Faestermann, T., Geissel, H., Gerl, J., Gernhäuser, R., Górska, M., Gottardo, A., Grawe, H., Grębosz, J., Krücken, R., Kurz, N., Liu, Z., Maier, L., Nowacki, F., Pietri, S., Podolyák, Z., Sieja, K., Steiger, K., Straub, K., Weick, H., Wollersheim, H.-J., Woods, P., Al-Dahan, N., Alkhomashi, N., Ataç, A., Blazhev, A., Braun, N., Čeliković, I., Davinson, T., Dillmann, I., Domingo-Pardo, C., Doornenbal, P., De France, G., Farrelly, G., Farinon, F., Goel, N., Habermann, T., Hoischen, R., Janik, R., Karny, M., Kaşkaş, A., Kojouharov, I., Kröll, T., Litvinov, Y., Myalski, S., Nebel, F., Nishimura, S., Nociforo, C., Nyberg, J., Parikh, A., Procházka, A., Regan, P., Rigollet, C., Schaffner, H., Scheidenberger, C., Schwertel, S., Söderström, P.-A., Steer, S., Stolz, A. and Strmeň, P.: Superallowed Gamow-Teller decay of the doubly magic nucleus ^{100}Sn. *Nature*, vol. 486, no. 7403, Jun 2012. ISSN 0028-0836.

[29] Anselment, M., Bekk, K., Hanser, A., Hoeffgen, H., Meisel, G., Göring, S., Rebel, H. and Schatz, G.: Charge radii and moments of tin nuclei by laser spectroscopy. *Phys. Rev. C*, vol. 34, pp. 1052–1059, Sep 1986.
Available at: https://link.aps.org/doi/10.1103/PhysRevC.34.1052

[30] Eberz, J., Dinger, U., Huber, G., Lochmann, H., Menges, R., Ulm, G., Kirchner, R., Klepper, O., Kühl, T.U. and Marx, D.: Nuclear spins, moments and charge radii of $^{108-111}$Sn. *Zeitschrift für Physik A Atomic Nuclei*, vol. 326, no. 2, pp. 121–129, Jun 1987. ISSN 0939-7922.
Available at: https://doi.org/10.1007/BF01283586

[31] Le Blanc, F., Cabaret, L., Cottereau, E., Crawford, J.E., Essabaa, S., Genevey, J., Horn, R., Huber, G., Lassen, J., Lee, J.K.P., Scornet, G.L., Lettry, J., Obert, J., Oms, J., Ouchrif, A., Pinard, J., Ravn, H., Roussière, B., Sauvage, J. and Verney, D.: Charge-radius change and nuclear moments in the heavy tin isotopes from laser spectroscopy: Charge radius of ^{132}Sn. *Phys. Rev. C*, vol. 72,

p. 034305, Sep 2005.
Available at: https://link.aps.org/doi/10.1103/PhysRevC.72.034305

[32] Fedosseev, V.N., Kudryavtsev, Y. and Mishin, V.I.: Resonance laser ionization of atoms for nuclear physics. *Physica Scripta*, vol. 85, no. 5, p. 058104, Apr 2012.
Available at: https://doi.org/10.1088/0031-8949/85/05/058104

[33] Vautherin, D. and Brink, D.M.: Hartree-Fock Calculations with Skyrme's Interaction. I. Spherical Nuclei. *Phys. Rev. C*, vol. 5, pp. 626–647, Mar 1972.
Available at: https://link.aps.org/doi/10.1103/PhysRevC.5.626

[34] Dechargé, J. and Gogny, D.: Hartree-Fock-Bogolyubov calculations with the $D1$ effective interaction on spherical nuclei. *Phys. Rev. C*, vol. 21, pp. 1568–1593, Apr 1980.
Available at: https://link.aps.org/doi/10.1103/PhysRevC.21.1568

[35] Berger, J., Girod, M. and Gogny, D.: Microscopic analysis of collective dynamics in low energy fission. *Nuclear Physics A*, vol. 428, no. Supplement C, pp. 23 – 36, 1984. ISSN 0375-9474.
Available at: http://www.sciencedirect.com/science/article/pii/0375947484902409

[36] Jones, K.L., Adekola, A.S., Bardayan, D.W., Blackmon, J.C., Chae, K.Y., Chipps, K.A., Cizewski, J.A., Erikson, L., Harlin, C., Hatarik, R., Kapler, R., Kozub, R.L., Liang, J.F., Livesay, R., Ma, Z., Moazen, B.H., Nesaraja, C.D., Nunes, F.M., Pain, S.D., Patterson, N.P., Shapira, D., Shriner, J.F., Smith, M.S., Swan, T.P. and Thomas, J.S.: The magic nature of ^{132}Sn explored through the single-particle states of ^{133}Sn. *Nature*, vol. 465, no. 7297, pp. 454–457, May 2010.
Available at: https://doi.org/10.1038/nature09048

[37] Urban, W., Kurcewicz, W., Nowak, A., Rząca-Urban, T., Durell, J., Leddy, M., Jones, M., Phillips, W., Smith, A., Varley, B., Bentaleb, M., Lubkiewicz, E., Schulz, N., Blomqvist, J., Daly, P., Bhattacharyya, P., Zhang, C., Ahmad, I. and Morss, L.: Neutron single-particle energies in the ^{132}Sn region. *The European Physical Journal A*, vol. 5, no. 3, pp. 239–241, Jul 1999.
Available at: https://doi.org/10.1007/s100500050280

[38] Borzov, I.N., Fayans, S.A., Krömer, E. and Zawischa, D.: Ground state properties and β-decay half-lives near ^{132}Sn in a self-consistent theory. *Zeitschrift für Physik A: Hadrons and Nuclei*, vol. 355, no. 1, pp. 117–127, Dec 1996.
Available at: https://doi.org/10.1007/bf02769674

[39] Foot, C.: *Atomic Physics*. The Oxford Master Series. Oxford University Press, New York, N.Y., 2005. ISBN 0198506953.

[40] Kramida, A., Yu. Ralchenko, Reader, J. and and NIST ASD Team: NIST Atomic Spectra Database, [Online]. Available: https://physics.nist.gov/asd

[2018, December 23]. National Institute of Standards and Technology, Gaithersburg, MD., 2018.

[41] Kluge, H.-J.: Atomic physics techniques for studying nuclear ground state properties, fundamental interactions and symmetries: status and perspectives. *Hyperfine Interactions*, vol. 196, no. 1, pp. 295–337, Feb 2010. ISSN 1572-9540.
Available at: `https://doi.org/10.1007/s10751-010-0172-9`

[42] Castel, B. and Towner, I.S.: *Modern Theories of Nuclear Moments (Oxford Studies in Nuclear Physics)*. Clarendon Press, 1990. ISBN 0198517289.

[43] Neugart, R. and Neyens, G.: *Nuclear Moments*, vol. 700, pp. 135–189. Aug 2006.

[44] Heyde, K.: *The Nuclear Shell Model.* Springer, 2013. ISBN 3642790542.

[45] Bohr, A. and Mottelson, B.: *Nuclear Structure: Single-Particle Motion: 001.* W. A. Benjamin, 1969. ISBN 0318354683.

[46] Cheal, B. and Flanagan, K.: Progress in laser spectroscopy at radioactive ion beam facilities. *Journal of Physics G: Nuclear and Particle Physics*, vol. 37, no. 11, p. 113101, 2010.
Available at: `http://stacks.iop.org/0954-3899/37/i=11/a=113101`

[47] King, W.: *Isotope Shifts in Atomic Spectra (Physics of Atoms and Molecules).* Springer, 1984. ISBN 9780306415623.

[48] Bodmer, A.: Nuclear scattering of electrons and isotope shift. *Proceedings of the Physical Society. Section A*, vol. 66, no. 11, pp. 1041–1058, Nov 1953.
Available at: `https://doi.org/10.1088/0370-1298/66/11/308`

[49] Blundell, S., Baird, P., Palmer, C., Stacey, D., Woodgate, G. and Zimmermann, D.: A re-evaluation of isotope shift constants. *Zeitschrift für Physik A Atoms and Nuclei*, vol. 321, no. 1, pp. 31–33, Mar 1985. ISSN 0939-7922.
Available at: `https://doi.org/10.1007/BF01411940`

[50] Kreim, K., Bissell, M., Papuga, J., Blaum, K., De Rydt, M., Garcia Ruiz, R., Goriely, S., Heylen, H., Kowalska, M., Neugart, R., Neyens, G., Nörtershäuser, W., Rajabali, M., Sánchez Alarcón, R., Stroke, H. and Yordanov, D.: Nuclear charge radii of potassium isotopes beyond N = 28. *Physics Letters B*, vol. 731, pp. 97–102, Apr 2014.
Available at: `https://doi.org/10.1016/j.physletb.2014.02.012`

[51] Hurst, G. and Parks, J.: *Atomic, Molecular, and Optical Physics: Atoms and Molecules*, chap. Methods and Applications of Resonance Ionization Spectroscopy. Academic Press.

[52] Letokhov, V.S.: *Laser Photoionization Spectroscopy.* Academic Press, 1987. ISBN 0124443206.

[53] Letokhov, V.S.: On the possibilities of isotope separating by methods of the resonant photoionization of atoms and photo-dissociation of molecules by laser radiation. Tech. Rep., P.N. Lebedev Physical Insitute, 1969.

[54] Ambartsumyan, R.V., Kalinin, V. and Letokhov, V.: Two-step Selective Photoionization of Rubidium Atoms by Laser Radiation. *Soviet Journal of Experimental and Theoretical Physics Letters*, vol. 13, p. 217, Mar 1971.

[55] Kluge, H.-J.: Resonance ionization spectroscopy and its applications. In: *Proceedings of the International Conference "Quantum Optics III"*.

[56] Ferrer, R., Bastin, B., Boilley, D., Creemers, P., Delahaye, P., Liénard, E., Fléchard, X., Franchoo, S., Ghys, L., Huyse, M., Kudryavtsev, Y., Lecesne, N., Lu, H., Lutton, F., Mogilevskiy, E., Pauwels, D., Piot, J., Radulov, D., Rens, L., Savajols, H., Thomas, J., Traykov, E., Beveren, C.V., den Bergh, P.V. and Duppen, P.V.: In gas laser ionization and spectroscopy experiments at the superconducting separator spectrometer (S3): Conceptual studies and preliminary design. *Nuclear Instruments and Methods in Physics Research Section B: Beam Interactions with Materials and Atoms*, vol. 317, pp. 570–581, Dec 2013.
Available at: https://doi.org/10.1016/j.nimb.2013.07.028

[57] Saloman, E.: A resonance ionization spectroscopy/resonance ionization mass spectrometry data service. *Spectrochimica Acta Part B: Atomic Spectroscopy*, vol. 47, no. 4, pp. 517–543, Apr 1992.
Available at: https://doi.org/10.1016/0584-8547(92)80044-h

[58] Boyd, R.W.: *Nonlinear Optics.* Academic Press, 2008. ISBN 0123694701.

[59] Guenther, B.D.: *Modern optics.* Wiley, New York, N.Y., 1990. ISBN 0471512885.

[60] Wiley, W. and McLaren, I.: Time-of-Flight Mass Spectrometer with Improved Resolution. *Review of Scientific Instruments*, vol. 26, no. 12, pp. 1150–1157, Dec 1955.
Available at: https://doi.org/10.1063/1.1715212

[61] Mamyrin, B., Karataev, V., Shmikk, D. and Zagulin, V.: The mass-reflectron, a new nonmagnetic time-of-flight mass spectrometer with high resolution. *Soviet Physics Journal of Experimental and Theoretical Physics*, vol. 37, 1973.

[62] Boesl, U.: Time-of-flight mass spectrometry: Introduction to the basics. *Mass Spectrometry Reviews*, vol. 36, Nov 2016.
Available at: https://doi.org/10.1002/mas.21520

[63] Ramsey, N.: *Atomic, Molecular, and Optical Physics: Atoms and Molecules*, chap. Thermal Beam Sources. Academic Press.

[64] Pauly, H.: *Atomic and Molecular Beam Methods*, chap. Other Low-Enrgy Beam Source. Oxford University Press, 1988.

[65] Kennard, E.: The kinetic theory of gases. *Journal of the Society of Chemical Industry*, 1938.

[66] Ramsey, N.: *Molecular Beams (Oxford Classic Texts in the Physical Sciences)*. Oxford University Press, 1956, 1990. ISBN 0198520212.

[67] Stern, O.: Eine direkte messung der thermischen molekulargeschwindigkeit. *Zeitschrift für Physik*, vol. 2, no. 1, pp. 49–56, Feb 1920. ISSN 0044-3328.
Available at: https://doi.org/10.1007/BF01333787

[68] Pauly, H.: *Atom, Molecule, and Cluster Beams I: Basic Theory, Production and Detection of Thermal Energy Beams (Springer Series on Atomic, Optical, and Plasma Physics)*. Springer, 2010. ISBN 3642086233.

[69] Kantrowitz, A. and Grey, J.: A high intensity source for the molecular beam. part i. theoretical. *Review of Scientific Instruments*, vol. 22, no. 5, pp. 328–332, May 1951.
Available at: https://doi.org/10.1063/1.1745921

[70] Kistiakowsky, G.B. and Slichter, W.P.: A high intensity source for the molecular beam. part II. experimental. *Review of Scientific Instruments*, vol. 22, no. 5, pp. 333–337, May 1951.
Available at: https://doi.org/10.1063/1.1745922

[71] Becker, E. and Bier, K.: Die erzeugung eines intensiven, teilweise monochromatisierten wasserstoff-molekularstrahles mit einer laval-düse. *Zeitschrift für Naturforschung A*, vol. 9, no. 11, Jan 1954.
Available at: https://doi.org/10.1515/zna-1954-1113

[72] Becker, E.W. and Henkes, W.: Geschwindigkeitsanalyse vonlaval-strahlen. *Zeitschrift für Physik*, vol. 146, no. 3, pp. 320–332, Jun 1956. ISSN 0044-3328.
Available at: https://doi.org/10.1007/BF01330427

[73] Koperski, J. and Fry, E.S.: Molecules in the cold environment of a supersonic free-jet beam: from spectroscopy of neutralneutral interactions to a test of bell's inequality. *Journal of Physics B: Atomic, Molecular and Optical Physics*, vol. 39, no. 19, pp. S1125–S1150, 2006. ISSN 0953-4075.

[74] Morse, M.: *Atomic, Molecular, and Optical Physics: Atoms and Molecules*, chap. Supersonic Beam Sources. Academic Press.

[75] Miller, D.: *Atomic and Molecular Beam Methods*, chap. Free Jet Sources. Oxford University Press, 1988.

[76] Wegener, P.: *Molecular beams and low density gas dynamics*. M. Dekker, 1974. ISBN 0824761995.

[77] Lubman, D.M., Rettner, C.T. and Zare, R.N.: How isolated are molecules in a molecular beam? *The Journal of Physical Chemistry*, vol. 86, no. 7, pp. 1129–1135, 1982. ISSN 0022-3654.

[78] *Rarefied gas dynamics : proceedings of the Fourth International Symposium on Rarefied Gas Dynamics.* Advances in applied mechanics ; suppl. 3, v. 1. Academic Press, 1965.

[79] Kalvas, T., Tarvainen, O., Ropponen, T., Steczkiewicz, O., Ärje, J. and Clark, H.: IBSIMU: A three-dimensional simulation software for charged particle optics. *Review of Scientific Instruments*, vol. 81, no. 2, p. 02B703, Feb 2010.
Available at: `https://doi.org/10.1063/1.3258608`

[80] du Plessis, A., Strydom, C.A., Uys, H. and Botha, L.R.: Laser induced and controlled chemical reaction of carbon monoxide and hydrogen. *The Journal of Chemical Physics*, vol. 135, no. 20, p. 204303, Nov 2011.
Available at: `https://doi.org/10.1063/1.3662129`

[81] Eimerl, D., Davis, L., Velsko, S., Graham, E.K. and Zalkin, A.: Optical, mechanical, and thermal properties of barium borate. *Journal of Applied Physics*, vol. 62, no. 5, pp. 1968–1983, Sep 1987.
Available at: `https://doi.org/10.1063/1.339536`

[82] Biraben, F., Cagnac, B. and Grynberg, G.: Experimental evidence of two-photon transition without doppler broadening. *Physical Review Letters*, vol. 32, no. 12, pp. 643–645, Mar 1974.
Available at: `https://doi.org/10.1103/physrevlett.32.643`

[83] Hänsch, T.W., Lee, S.A., Wallenstein, R. and Wieman, C.: Doppler-free two-photon spectroscopy of hydrogen 1S-2S. *Physical Review Letters*, vol. 34, no. 6, pp. 307–309, Feb 1975.
Available at: `https://doi.org/10.1103/physrevlett.34.307`